



Room 14-0551
77 Massachusetts Avenue
Cambridge, MA 02139
Ph: 617.253.5668 Fax: 617.253.1690
Email: docs@mit.edu
<http://libraries.mit.edu/docs>

DISCLAIMER OF QUALITY

Due to the condition of the original material, there are unavoidable flaws in this reproduction. We have made every effort possible to provide you with the best copy available. If you are dissatisfied with this product and find it unusable, please contact Document Services as soon as possible.

Thank you.

Some pages in the original document contain pictures, graphics, or text that is illegible.

Impulsive Stimulated Scattering Spectroscopy of Thin Film and Bulk Ferroelectric Systems

by

Lisa Dhar

B.S. Chemistry, University of Chicago
1989

Submitted to the Department of Chemistry in partial fulfillment of the
requirements for the degree of

Doctor of Philosophy

at the

MASSACHUSETTS INSTITUTE OF TECHNOLOGY

September, 1994

© Massachusetts Institute of Technology, 1994
All rights reserved

Signature of Author _____
Department of Chemistry
August 5, 1994

Certified by _____
Keith A. Nelson
Thesis Supervisor

Accepted by _____
Dietmar Seyferth
Chairman, Departmental Committee on Graduate Students

MASSACHUSETTS INSTITUTE
OF TECHNOLOGY

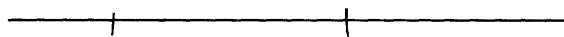
OCT 05 1994

LIBRARIES

Science

This doctoral thesis has been examined by a committee of the Department of Chemistry as follows:

Professor Sylvia T. Ceyer



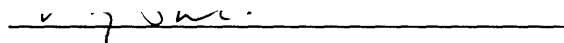
Chairperson

Professor Keith A. Nelson



Thesis Supervisor

Professor Mounji G. Bawendi



Impulsive Stimulated Scattering Spectroscopy of Thin Film and Bulk Ferroelectric Systems

By Lisa Dhar

Submitted to the Department of Chemistry on August 23, 1994 in partial fulfillment of the requirements for the degree of Doctor of Philosophy in Chemistry

Abstract

A laser-based ultrasonic technique, impulsive stimulated thermal scattering (ISTS), is used to characterize the acoustic waveguide behavior in a series of silicon-supported and free-standing polyimide bilayer structures. The experimental results demonstrate that multilayer structures are characterizable using ISTS measurements. In addition, simulations of acoustic waveguide behavior in coatings with very thin interfacial layers adjacent to the substrate and in films with continuously changing elastic properties are presented. The results indicate depth-profiling possibilities using ISTS.

The same technique is used to evaluate the acoustic wave properties of the piezoelectric film lead zirconium titanate. In this study, numerical results are also presented calculating the electric fields and potentials that accompany the acoustic excitations in this material.

Femtosecond impulsive stimulated Raman scattering (ISRS) experiments are performed on the lowest frequency A_1 polariton in the ferroelectric crystal lead titanate. The experimental results coupled with numerical simulations of the polariton behavior focus upon the anharmonic nature of the lattice potential demonstrating that the anharmonicity can be detected in ISRS experiments.

An optical technique for performing single-shot pump-probe spectroscopy with femtosecond time resolution is demonstrated. The time-dependent absorption of the laser dyes Nile blue, cresyl violet, and ethyl violet is monitored using this technique. The possibility of probing the dynamics of irreversible processes initiated through photoexcitation is discussed.

Thesis Supervisor: Dr. Keith A. Nelson

Title: Professor of Chemistry

Acknowledgments:

I would like to begin by thanking my parents whose love, support, and guidance have been my greatest inspiration. Whatever I have been able to achieve in school is due to their hard work and encouragement.

I greatly appreciate the enthusiasm and energy for science of my advisor, Keith Nelson. His physical insight into problems and endless supply of ideas were a immense help to me throughout my graduate work.

In the Nelson group, I have had the good luck to work with an extremely capable and motivated group of people. I must begin by thanking John Rogers whose tremendous depth and breadth of knowledge never ceased to amaze me. I cannot overstate how much I learned by working with him on the thin film projects and how much I appreciate his suggestions and advice on whatever I ran into trouble with. I was always in awe of Dr. Andrew Cook's experimental and computer expertise which benefited not only me but many others in the group. Dr. Matthew Banet's bent for applied science was a huge asset to the group, making us all think past just getting signal. Special thanks to Bernd Burfeindt for his hard work on the regenerative amplifier that was used for the single shot and lead titanate experiments. Dr. Thomas Dougherty was a storehouse of information on ferroelectrics and his code to run the normalization algorithm for the single-shot experiment was the secret to its success. Dr. Gary Wiederrecht introduced me to the wonders of the amplified dye laser system and his experiments on lithium tantalate were a great help for the work on lead titanate. I would like to thank Dr. John Fourkas for an enjoyable collaboration on the single-shot experiment. I would also like to thank past group members Dr. Anil Duggal, Dr. Ion Halalai, Chris Mindas, Dr. Scott Silence, and Dr. Dong Hong Wu and present group members Kerry Brennan, Dutch Chung, Dr. Hitoshi Kawashima, Laura Muller, Dora Paolucci, Weining Wang, Marc Wefers, and Yong-Wu Yang (the number one Bulls fan) for making the basement of building 2 an extremely enjoyable place to spend my graduate career.

Outside the Nelson group, Bhavani Rajaram's sympathy about recalcitrant lasers was greatly appreciated. I value her friendship highly and will miss her dearly. Dr. Theresa Kavanaugh was an extremely valuable resource, answering all of my theoretical questions, and is a wonderful friend.

I would also to thank Professor N.C. Yang and Professor Graham Fleming for research opportunities while I was an undergraduate. Working with

Dr. Alexander Harris during the summer between college and graduate school was a tremendous experience, exposing me to the world of Bell Laboratories and introducing me to surface vibrational dynamics. I also was fortunate to work in the laboratory of Dr. James Butler of the Naval Research Laboratory allowing me to learn about the glittering world of CVD diamonds.

Finally, I would like to thank my family in India whose love from halfway around the world means an infinite amount to me.

To my mother and father

Table of Contents

1. Introduction	9
2. Experimental Methods	12
3. Moduli Determination in Polyimide Film Bilayer Systems: Prospects for Depth Profiling Using Impulsive Stimulated Thermal Scattering	
3.1 Introduction	14
3.2 Experimental	16
3.3 The ISTS Technique	
3.3a Qualitative Description and Background	20
3.3b Typical Data	25
3.3c Theory	28
3.4 Results	34
3.5 Discussion	
3.5a Interpretation of ISTS results on polymer bilayer structures	34
3.5b Detection of Very Thin Interfacial Layers	43
3.5c Continuously-Varying Depth-Dependent Elastic Properties	48
3.5d Limitations of ISTS measurements	54
3.6 Conclusions	54
4. Impulsive Stimulated Thermal Scattering Spectroscopy of Piezoelectric and Metallic Multilayer Systems	
4.1 Introduction	61
4.2 Experimental	62
4.3 Experimental Results	64
4.4 Theory	67
4.5 Discussion of Experimental Results	78
4.6 Conclusion	82

5. Impulsive Stimulated Raman Scattering Spectroscopy and Finite Element Modeling of Polariton Dynamics in an Anharmonic Lattice	
5.1 Introduction	84
5.2 Experimental	85
5.3 Experimental Results	88
5.4 Polaritons in a Harmonic Lattice	91
5.5 Polaritons in an Anharmonic Lattice.....	99
5.6 Numerical Simulations of the Polaritons Dynamics in Lead Titanate	103
5.7 Conclusion	107
6. Single-Shot Ultrafast Absorption Spectroscopy	
6.1 Introduction	109
6.2 Experimental	110
6.3 Results	117
6.4 Discussion	117
6.5 Limitations of the Single Shot Technique	123
6.6 Conclusion	124
7. Future Directions	126
Appendix A	127
Appendix B	131

Chapter 1. Introduction

Impulsive stimulated scattering (ISS) spectroscopy has proved to be a powerful tool in exploring material dynamics in a wide range of condensed matter problems. In ISS experiments, material excitations are coherently excited and probed providing new insights into chemical and structural rearrangements in all phases of matter and into the dynamical behavior of crystal lattices, liquids and isolated molecules.

In this thesis are described ISS experiments that probe material dynamics in two different temporal regimes. The first, which probes material motions in the nanosecond to millisecond regime, is known as impulsive stimulated thermal scattering (ISTS) spectroscopy and is used to probe the acoustic waveguide behavior in thin film systems. The second type of experiment, which probes vibrational dynamics in the femtosecond to picosecond range, is known as impulsive stimulated Raman (ISRS) spectroscopy, and is used to investigate polariton behavior in ferroelectric crystals. Also described in this thesis is an experimental methodology for performing single-shot pump-probe spectroscopy, a technique that is expected to be extremely useful for probing irreversible chemical and structural processes.

Thin films have become extremely important in a wide range of areas from electronics packaging industries to the aerospace and automotives industries to bioengineering applications. Of utmost importance in all of their applications are their mechanical properties. Quantities that characterize the elastic properties of thin films guide film

fabrication and design choices and are therefore the subject of extensive experimental investigations. ISTS has been used to characterize the acoustic waveguide behavior in films of micron thicknesses yielding information on their mechanical and adhesive properties. The first discussion of ISTS in this thesis focuses upon the depth-profiling capabilities of ISTS. Often film fabrication procedures yield films which exhibit depth-dependent and anisotropic material properties. In Chapter 3 are presented experimental and theoretical results that establish the sensitivity of ISTS to depth-dependent elastic properties.

ISTS is also used to explore the acoustic wave properties in piezoelectric thin films. The potential for piezoelectric films to become integrated into surface acoustic wave devices is currently the subject of great interest and therefore requires a characterization of the acoustic properties of these films. Chapter 4 discusses numerical calculations and ISTS investigations into the piezoelectric film of lead zirconium titanate.

Chapter 5 focuses upon ISRS investigations into the dynamics of the lowest frequency A1 polariton in the ferroelectric crystal lead titanate. This vibrational mode is believed to experience a highly anharmonic lattice potential implying there should be a strong effect upon the behavior of this mode in the polariton regime. Finite element modeling and experimental investigations provide evidence for the existence of strong anharmonicity. The results also suggest that the dispersive behavior of polaritons may be exploited to sample selected areas of the lattice potential energy surface.

Finally, an experimental methodology for performing single-shot pump-probe femtosecond spectroscopy is presented in Chapter 6. The

dynamics of photo-initiated irreversible chemical or structural processes are not easily probed using traditional time-resolved experimental techniques. This chapter outlines a simple method for recording the femtosecond dynamics of a processes in a single excitation laser shot-probe laser shot sequence.

Chapter 7 outlines future research directions suggested by the work presented in this thesis.

Chapter 2. Experimental Methods

Both laser systems used for experiments in this thesis have been described in detail elsewhere^{1,2} therefore only a brief description will be given here.

For the ISTS experiments, a Q-switched, mode-locked, and cavity-dumped neodymium-doped yttrium aluminum garnet (YAG) laser served as the pump laser. The laser yielded 1.064 μm light with energy of 0.8 - 1.0 mJ per pulse at a repetition rate of 570 Hz. The probe laser was an electro-optically modulated argon ion laser. A temperature-tuned etalon insured single-mode operation. The output power is approximately 1 watt in the 514nm line. The diffracted probe light is detected by a small-area fast-amplified photodiode with a 2 GHz bandwidth. The photodiode signal is digitized with 1 GHz bandwidth transient digitizer and the resulting waveform is transferred to a computer for storage. The data collection times are in the range of 30 seconds to a few minutes. Typically 100 laser shots are averaged to yield signal with adequate signal-to-noise. Single-shot data collection is possible and often used with samples that damage easily.

For the ISRS experiments, an amplified femtosecond dye laser system was used. The dye laser was pumped by a Nd:YAG laser (Spectron Lasers) mode-locked using a Quantronix mode-locker. The output of this laser was approximately 9.5 to 10 watts of 70 ps pulses of 1.064 μm light. The infrared output was frequency doubled in a temperature-tuned LBO crystal yielding 532 nm light of energy 1 watt. The resulting green light was used to synchronously pump a antiresonant ring dye laser. Rhodamine

590 tetrafluoroborate dissolved in ethylene glycol was used as the gain medium while the saturable absorber is 3',3'-diethyloxadiacarbocyanine Iodide (DODCI) dissolved in ethylene glycol. This dye laser produces 80 fs pulses with pulse energies of approximately 0.1 nj.

The dye laser pulses are amplified in a three stage amplifier pumped by the frequency doubled output of a regenerative amplifier based on YAG oscillator. The regenerative amplifier is an optically seeded high gain cavity that outputs 1mj pulses at a repetition rate of up to 2.5 kHz. The modelocked output of the cw-laser provides the optical seed for the amplifier. A Pockels cell (Medox, Inc.) serves to switch in the seed pulse from the mode-locked laser. After approximately 100 round trips in the cavity, the pulse is switched out by the same Pockels cell. The infrared output is frequency doubled in a angle tuned LBO crystal yielding 400 μ j pulses at 532nm. This green light pumps three dye cells containing sulforrhodamine 640. After amplification, the pulses are recompressed with a pair of prisms, yielding an output of 80fs pulses with energy of approximately 10 μ j.

References

1. S. Silence, Ph.D. Thesis, Massachusetts Institute of Technology
2. A.G. Joly, Ph.D. Thesis, Massachusetts Institute of Technology

Chapter 3. Moduli Determination in Polyimide Film Bilayer Systems: Prospects for Depth Profiling Using Impulsive Stimulated Thermal Scattering

3.1. Introduction

Thin films are used in virtually every technologically advanced industry. Much attention has been focussed upon optical, mechanical, and thermal measurements of such films since these properties determine design choices in structures using the films^{1,2}. Accurate characterization is made difficult by the fact that many fabrication and processing steps yield films which in general have anisotropic and depth-dependent properties. For example it is well-established that many solvent-cast polyimide films, which are used throughout the microelectronics and aerospace industries due to their excellent temperature stability and mechanical properties³, exhibit preferential polymer chain orientation in the plane of the film. This leads to physical properties that are isotropic in the plane but whose in-plane and out-of-plane properties are different⁴⁻¹⁰. In addition to this, recent refractive index measurements in polyimide films of a range of thicknesses found that the birefringence of the films decreased as a function of increasing thickness suggesting that the substrate-induced ordering which leads to the in-plane orientation may also produce depth-dependent properties¹¹⁻¹⁸. This depth dependence has been accounted for in models by proposing either the existence of an interfacial layer located adjacent to

the substrate with higher anisotropy than the rest of the film or the existence of a continuous depth-dependent change in the physical properties with the degree of anisotropy decreasing as the distance from the substrate increases.

It is to be expected that depth-dependent ordering should affect not only the film birefringence but also the elastic properties of the film. In this paper, the ability to evaluate depth-dependent elastic properties using an ultrasonic method is evaluated. (Reference 19 gives a short list of previous theoretical and experimental investigations of depth-varying elastic properties in a variety of systems.) We focus upon the information accessible using a novel laser-based ultrasonic method known as Impulsive Stimulated Thermal Scattering (ISTS) spectroscopy²⁰. This method can be used to determine the acoustic waveguide properties of film structures with micron thicknesses which in turn can be used to extract information about their mechanical and adhesive properties. Thermal diffusivities can also be measured. In previous investigations, the viscoelastic properties of isotropic polyimide films and films with transverse isotropic symmetry (i.e. where the in-plane properties are isotropic but different from the through-plane properties) were determined²¹⁻²³. Film delamination detection capabilities with fine spatial resolution were also demonstrated²⁴. Additional investigations have evaluated the in-plane thermal diffusivities of a series of polyimide films²³ and superconducting films²⁵. In this paper we present experimental and theoretical results that establish the sensitivity of ISTS to depth-dependent elastic properties.

We begin with a brief review of the ISTS technique and the theory used to analyze ISTS data. We then focus on the experimental characterization of a series of polyimide bilayer structures. Our interest in

such structures was spurred by their intrinsic importance and by the suggestion mentioned above that there exists in general a thin interfacial layer adjacent to the substrate with different properties than the rest of the film. Therefore, bilayer samples were fabricated using anisotropic polyimides to mimic the highly ordered layer that is assumed to form near the substrate interface. Although these structures are rather artificial models of films with depth-dependent properties, they serve to establish the utility and test the sensitivity of ISTS as a depth-profiling tool and demonstrate how ISTS may be used to quantitatively measure the shear and longitudinal acoustic velocities of the individual layers.

We also present simulations of the acoustic waveguide behavior in systems which exhibit a continuous change in elastic properties, with an aim to highlight the signatures of depth-dependent elastic properties. We conclude by evaluating the capabilities and limitations of ISTS in this application.

3.2. Experimental

The ISTS experiment has been described in detail elsewhere²⁰. Figure 3.1 shows the experimental arrangement. Briefly, two short laser pulses are overlapped in time and space within an absorbing sample. The interference of the two pulses leads to an optical interference "grating" pattern with wavevector \mathbf{k} whose magnitude is given by $4\pi\sin(\theta/2)/\lambda$ where θ is the angle between the two excitation pulses and λ is the excitation pulse wavelength. Rapid nonradiative relaxation after absorption of the excitation pulses leads to formation of a temperature grating that images the optical interference grating. The impulsive creation of this grating

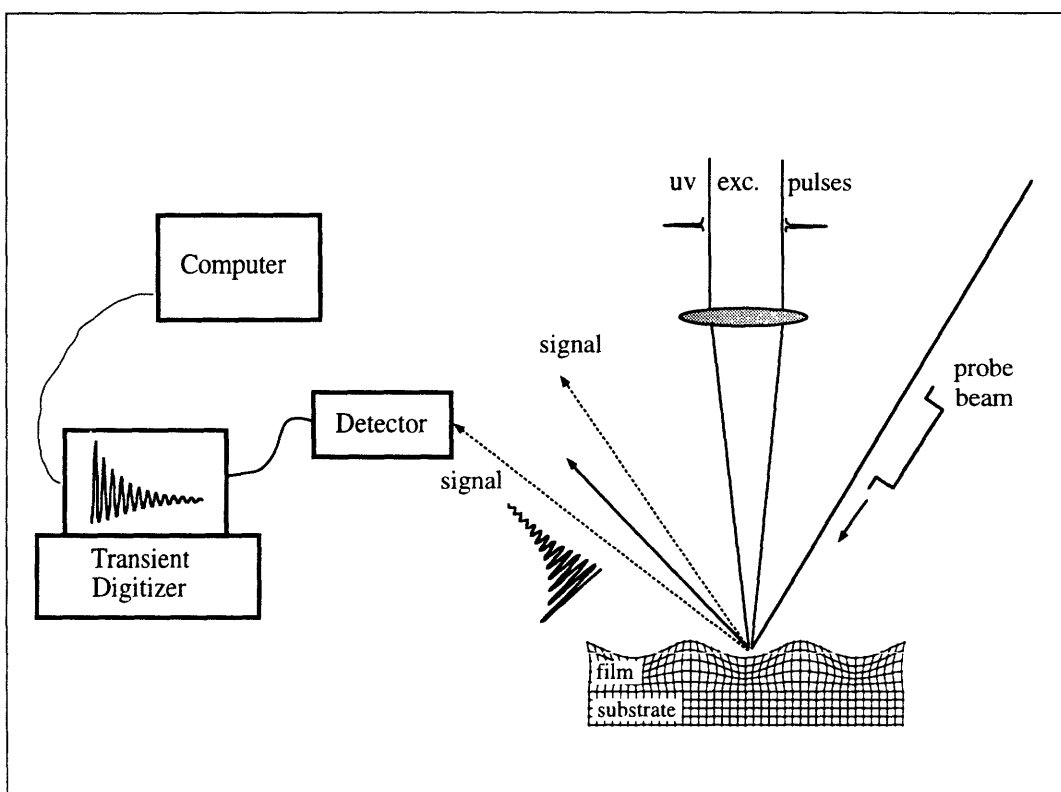


Figure 3.1. The experimental geometry for ISTS experiments. The two excitation pulses create a thermal grating within the sample with a well-defined wavevector. The probe pulse is diffracted off of the surface ripple induced by the thermal grating. The intensity of the diffracted light is electronically time-resolved by a fast amplified photodiode and transient digitizer.

drives thermal and acoustic responses at wavevectors $\pm\mathbf{k}$. Counterpropagating acoustic waves lead to damped oscillatory material motions while the thermal response persists as a quasi-steady state material response that slowly decays as heat travels from grating peaks to grating nulls. The resulting material motions are monitored in real time by diffracting a cw probe pulse off of the grating and electronically time-resolving the intensity of the diffracted light. Data collection times are on the order of milliseconds.

The excitation pulses originate from a Q-switched, mode-locked, and cavity-dumped Nd:YAG laser yielding 100 ps pulses with 1 mJ of energy at 1064 nm. This light is frequency-doubled to 532 nm in a lithium triborate (LBO) crystal. The 532 nm light is mixed with the undoubled 1064 nm light in a β -barium borate (BBO) crystal to yield excitation pulses at 355 nm, λ wavelength absorbed by the polyimide films. This light is passed through a beamsplitter to yield two excitation pulses whose path lengths are adjusted so that they are temporally coincident at the sample. The pulses are cylindrically focussed and crossed at an angle θ to overlap spatially at the sample. Approximately 1 μ J of the excitation light was required for the experiments described here.

The probe pulse originates from a continuous-wave single-mode argon ion laser which produces 1 watt at 514 nm. The output of the laser is electro-optically gated to yield a square pulse with a temporal width adjustable from 500 ns to seconds. The probe pulse is spatially coincident with the excitation pulses and the diffracted probe light is monitored by a fast amplified photodiode and transient digitizer. The effective bandwidth of the system is 1 GHz.

Experiments were conducted on polymer bilayers composed of the DuPont polyimides PI2555 (BTDA-ODA/MPDA), PI2545 (PMDA/ODA), and DuPont PI2611 (BPDA-PDA). The samples were fabricated in the following fashion. Polyamic acid precursor solutions were spin coated and fully cured on bare 10 cm diameter silicon substrates to produce the first polymer coating. Spin-coating and fully curing a different polyamic acid on top of this first layer yielded the bilayer structure. The thickness of each of the layers was measured after the two cures using a DEKTAK 8000 stylus profilometer by successively scratching off each polymer layer with a razor blade. A teflon jig apparatus along with a 6:1:1 mixture of HF:HNO₃:CH₃COOH were then used to etch the silicon away from the polymer layers in two selected regions of the samples. (It has been shown that this acid etch does not alter the mechanical properties of the polyimide films²⁶.) Following this etch, the samples were rinsed with deionized water and were allowed to dry for 48 hours in a dessicator. The bilayer systems fabricated for this study consisted of PI2555(5.49 μm top layer)/PI2611(1.19 μm bottom layer)/Si substrate, PI2555(4.34 μm)/PI2611(2.50 μm)/Si, PI2555(3.22 μm)/PI2545(2.99μm)/Si, and PI2555(2.94 μm)/PI 2611(3.56 μm)/Si.

The experiments were conducted on both the unsupported and supported regions of the samples. Although no significant differences were detected in ISTS data recorded from different supported regions or different unsupported regions of a film, care was exercised to record data from the same 1-cm² area of the unsupported and supported regions of the film for all of the wavevectors. The grating wavelengths used for these experiments were 4.13, 5.05, 5.50, 6.29, 7.26, 7.78, 8.14, 9.40, 11.62, 13.56 16.32, 20.00, 24.42, 28.37, 38.27 μm. The wavelengths were

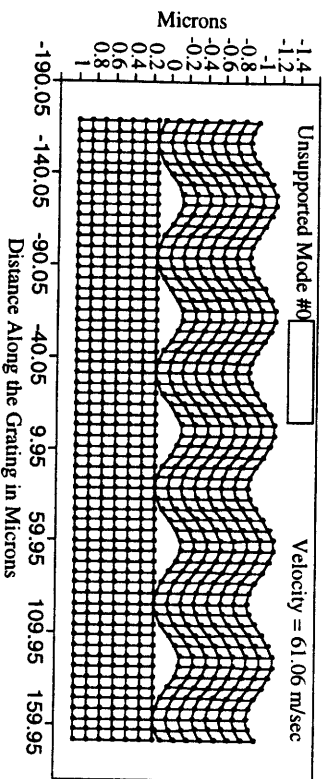
measured by burning a grating into a silicon wafer and measuring the grating wavelength with an optical microscope.

3.3. The ISTS Technique

3.3a. Qualitative Description and Background

In films whose thicknesses are on the order of the acoustic wavelength, ISTS excites material motions which exhibit strong waveguide effects. In particular, a number of acoustic waveguide modes, or normal modes, of the film are excited. As an illustration, the lowest four such modes at three different wavelengths in an unsupported and a silicon supported polymer film are shown in Figures 3.2 through 3.4. Each normal mode propagates in the plane of the film and is characterized by a distinct spatial character and phase velocity. This phase velocity is in general a function of the acoustic wavevector. That is, all of the modes are dispersive and the form of this dispersion is a function of the elastic properties of the system. The wavevector-dependent variations in the spatial characters of the modes are reflected in the velocity dispersion behavior which is illustrated in figure 3.5. Since each mode involves both in and out of plane shear and longitudinal motions, both the in and out of plane mechanical moduli determine the spatial nature and therefore the phase velocity dispersion of the mode. This fact has been used in previous work as a means to evaluate the moduli in several isotropic and anisotropic thin film systems²¹⁻²³. In this paper we exploit the fact that the displacements of each mode extend throughout the thickness of the structure. Because of this, any depth dependence in the mechanical

Part A



Part B

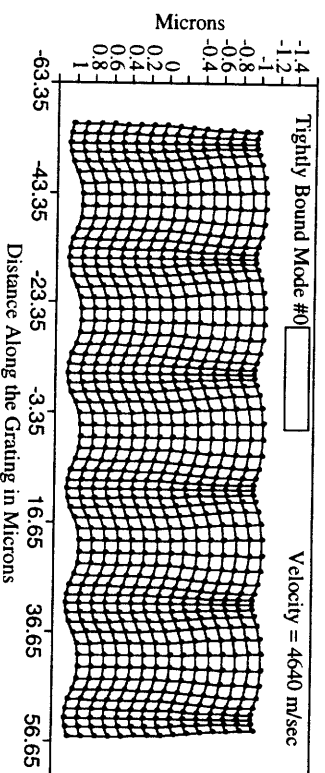
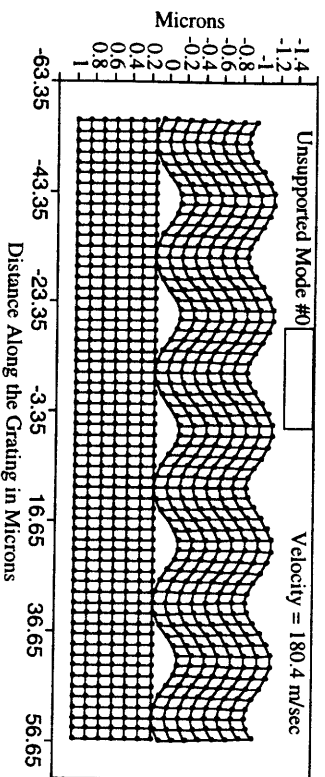
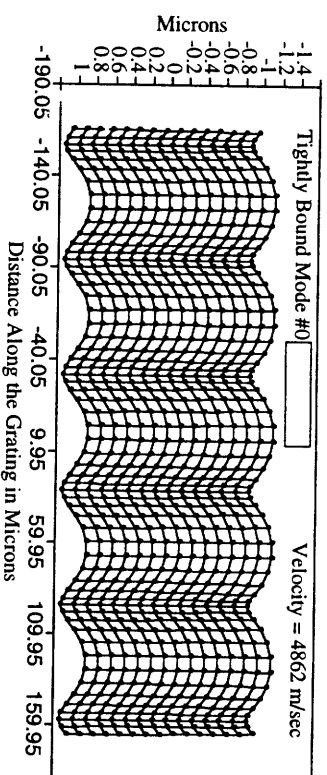
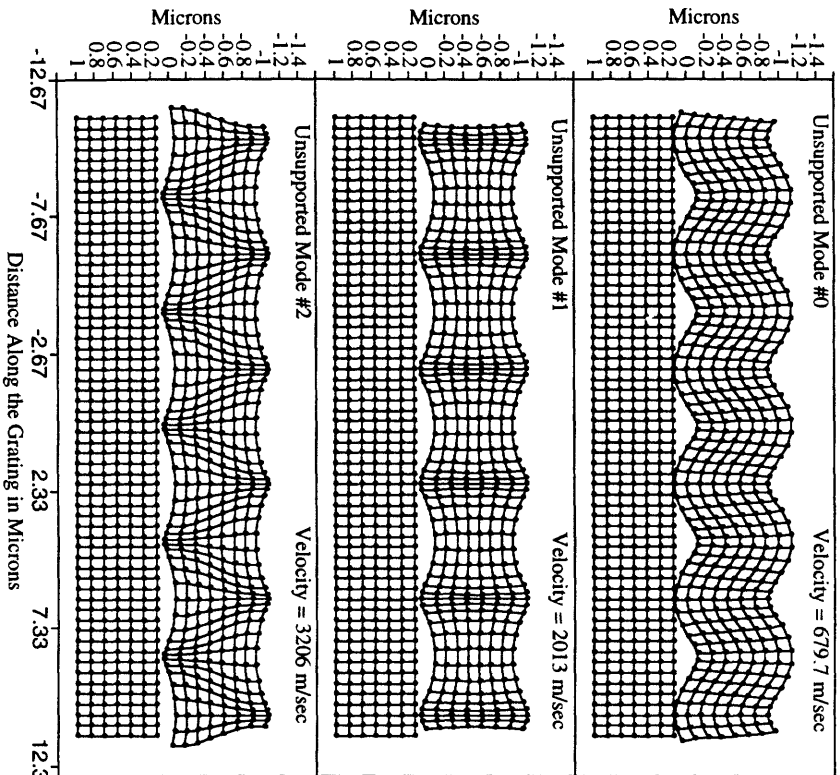


Figure 3.2. Lattice distortion diagrams illustrating the spatial nature of the lowest order acoustic waveguide modes which propagate in silicon supported (Part B) and unsupported (Part A) polymer films. The film thickness is $1.0 \mu\text{m}$ and the wavevector is $0.1 \mu\text{m}^{-1}$ for the upper frames and $0.3 \mu\text{m}^{-1}$ for the lower frames.

Part A



Part B

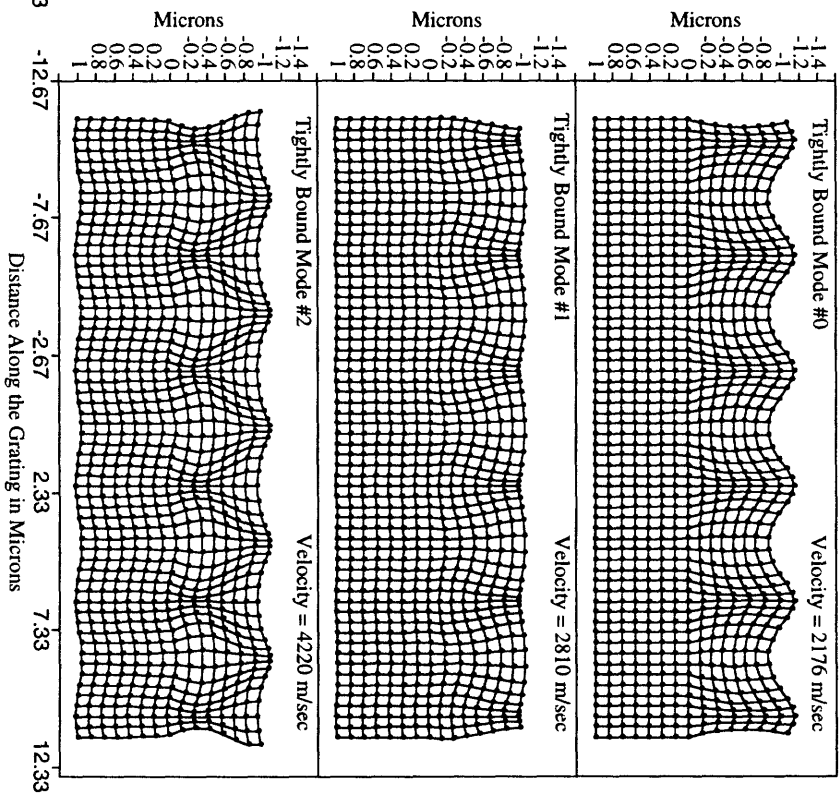
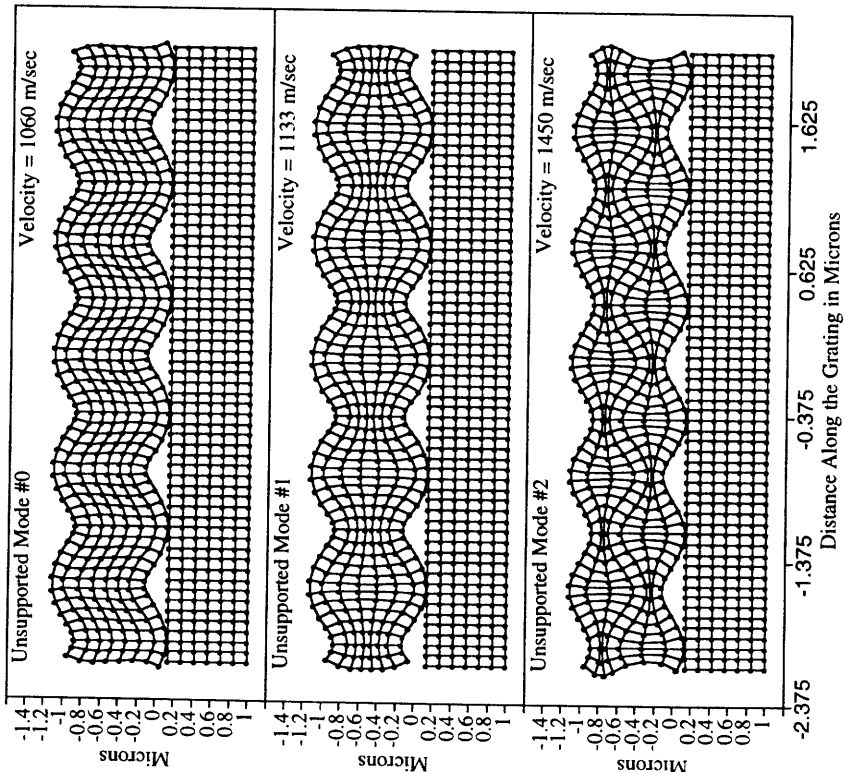


Figure 3.3. Lattice distortion diagrams illustrating the spatial nature of three lowest order acoustic waveguide modes which propagate in silicon supported (Part B) and unsupported (Part A) polymer films. The film thickness is 1.0 μm and the wavevector is 1.5 μm^{-1} .

Part A



Part B

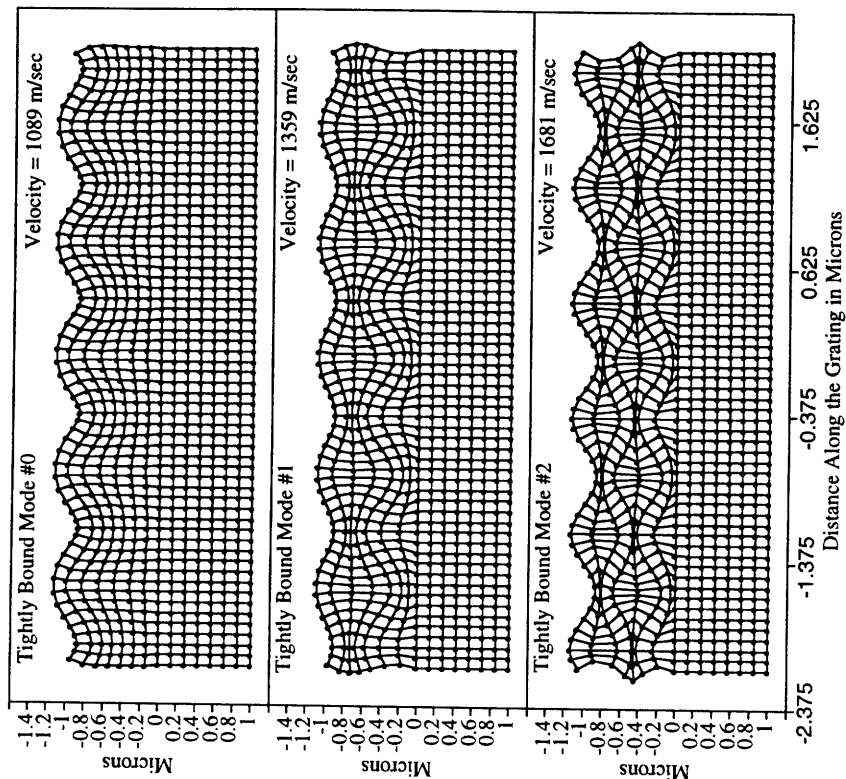


Figure 3.4. Lattice distortion diagrams illustrating the spatial nature of three lowest order acoustic waveguide modes which propagate in silicon supported (Part B) and unsupported (Part A) polymer films. The film thickness is $1.0 \mu\text{m}$ and the wavevector is $8.0 \mu\text{m}^{-1}$.

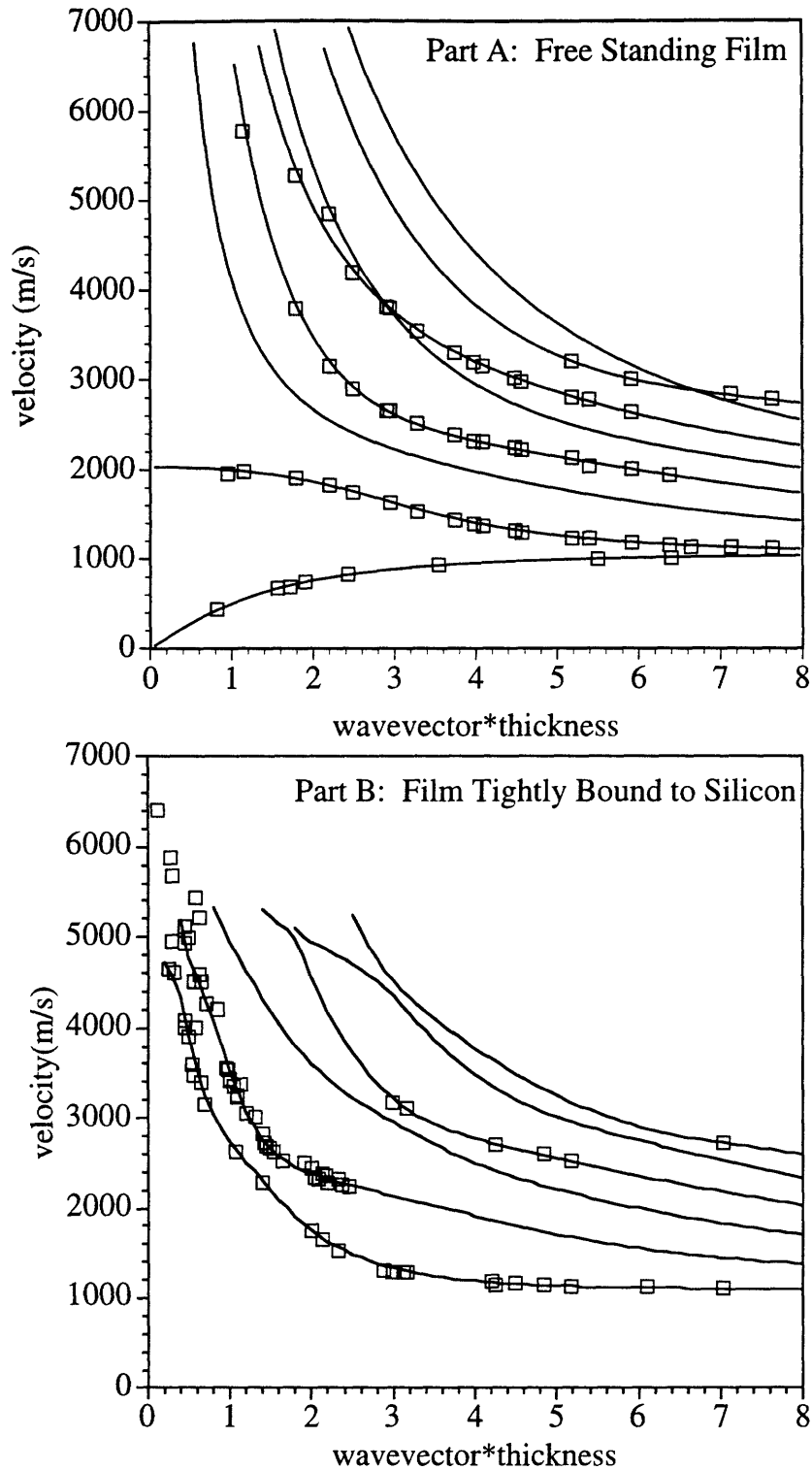


Figure 3.5. Data (symbols) and best fit acoustic velocity dispersion curves for unsupported (part A) and silicon-tightly bound (part B) DuPont PI2555 films with several thicknesses.

properties will be reflected in the spatial character and therefore in the phase velocity dispersion of the mode.

3.3b. Typical Data

Two typical ISTS data scans, one on the time scale of tens of nanoseconds and the other on the time scale of microseconds, are shown in Figure 3.6. From data like that shown in Figure 3.6(a) the acoustic phase velocities of the waveguide modes at a particular wavevector can be calculated. Data on a longer timescale like that shown in Figure 3.6(b) can be used to determine the in-plane and out-of-plane thermal diffusivities in the film. In this paper, we focus on the acoustic data.

As discussed in the preceding section, the acoustic phase velocity is determined by the mechanical moduli of the system, and any depth dependence in these moduli will affect the phase velocity. An illustration of this depth dependence in the raw data is given in Figure 3.7 where we display acoustic phase velocities determined in the PI2555(5.49 μm)/PI2611(1.19 μm)/Si and PI2555(4.34 μm)/PI2611(2.50 μm)/Si bilayer samples at a given acoustic wavevector. As is evident in every case, the phase velocities measured in the PI2555(4.34 μm)/PI2611(2.50 μm)/Si system are slightly larger than those in the PI2555(5.49 μm)/PI2611(1.19 μm)/Si system. This is a result of the slightly higher proportion of PI2611 (the stiffer polyimide) in the PI2555(4.34 μm)/PI2611(2.50 μm)/Si system than in the PI2555(5.49 μm)/PI2611(1.19 μm)/Si system. While this sort of behavior is expected, we highlight the fact that the phase velocity differences are not the same for each mode. It is the displacement field of the mode which

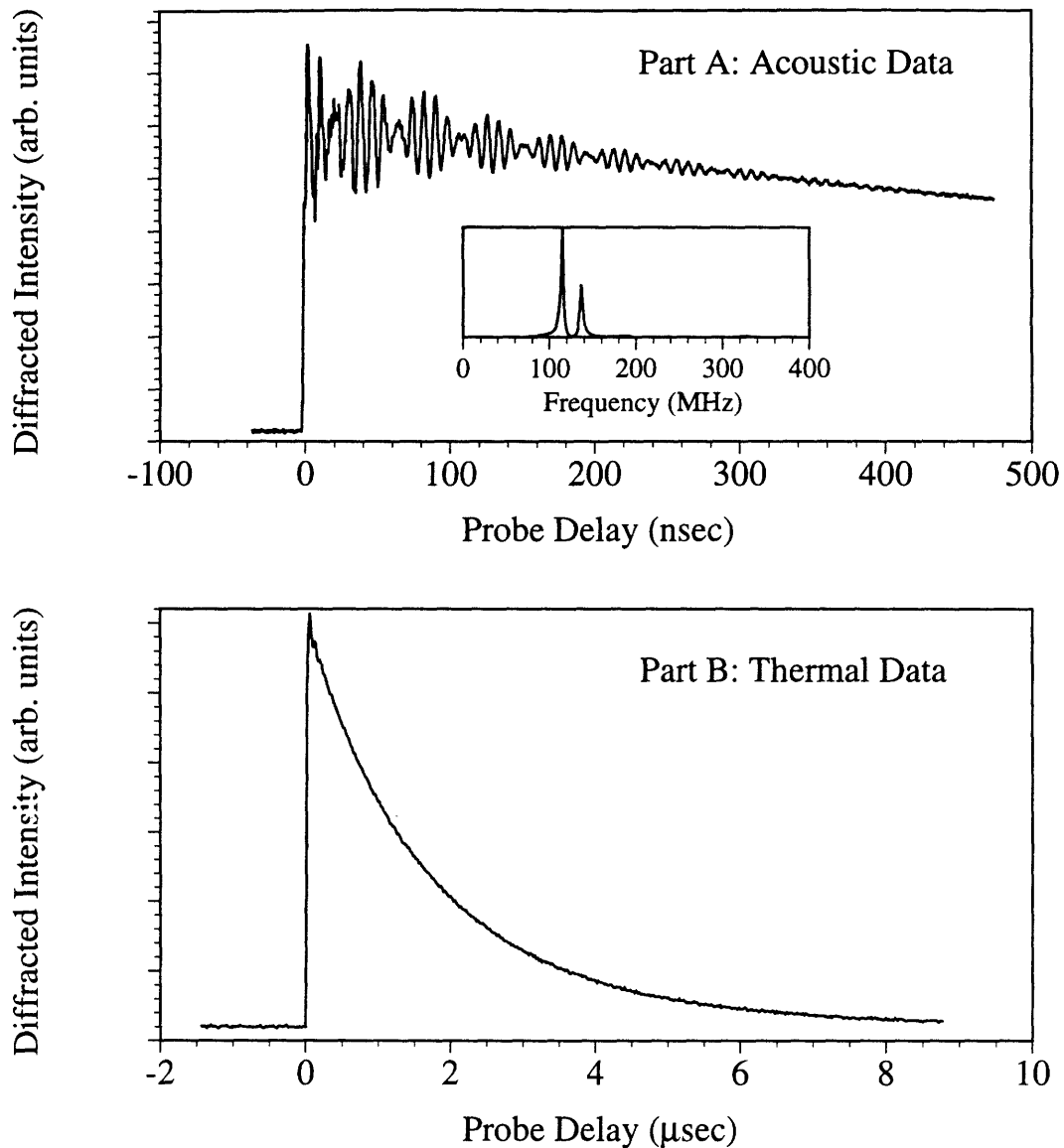


Figure 3.6. Typical ISTS data from a polyimide bilayer structure. The oscillations in (a) determine the frequency and damping of the counterpropagating acoustic waves generated by ISTS excitation. The phase velocities of the allowed waveguide modes at this wavevector can be calculated from the power spectrum of the data (shown in the inset). The decay in (b) is due to thermal diffusion within the sample. The thermal grating decays due to both in-plane and out-of-plane thermal diffusion.

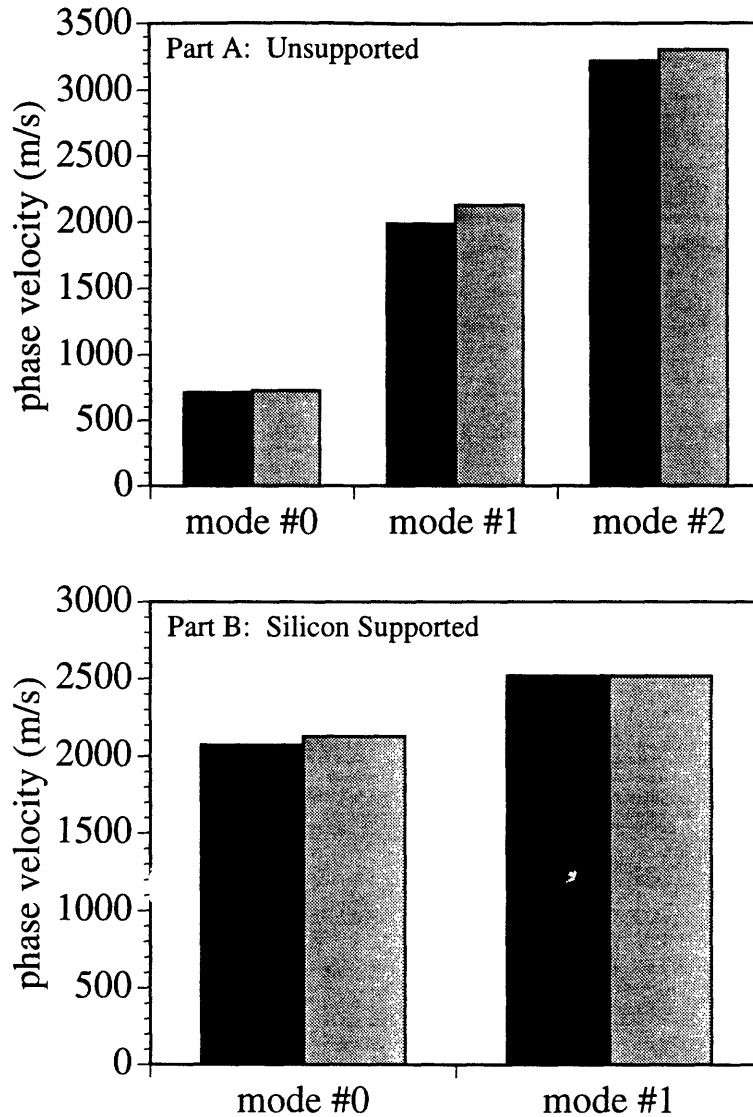


Figure 3.7. Experimentally determined acoustic phase velocities in (a) unsupported and (b) supported regions of the PI2555(5.49 μm)/PI2611(1.19 μm) (black bars) and the PI2555(4.34 μm)/PI2611(2.50 μm) (grey bars) bilayer structures. This data shows that for every mode, the bilayer composed of the larger fraction of PI2611 (the stiffer polyimide) has a higher phase velocity. While this sort of behavior is expected, it is important to note that the differences in the phase velocities from the two samples are not the same for each waveguide mode. This is a result of each waveguide mode "sampling" the structure at different depths, a fact which can be exploited for depth-profiling measurements.

determines this sensitivity. For example, modes with displacements localized to the upper surface of the structure will only be sensitive to the mechanical properties in that region. In what follows we show how to use this fact to quantify the depth-dependence of the moduli in these and other systems.

3.3c. Theory

The phase velocity dispersion can be calculated²⁷ by solving the elastic wave equations for particle displacements u_j within the film given in equation (1) and particle displacements $u_j^{(s)}$ in the substrate given in eqn (2) using the coordinate system illustrated in Figure 3.8

$$\rho \frac{\partial^2 u_j}{\partial t^2} - c_{ijkl} \frac{\partial^2 u_k}{\partial x_i \partial x_l} = 0 \quad (1)$$

$$\rho \frac{\partial^2 u_j^{(s)}}{\partial t^2} - c_{ijkl}^{(s)} \frac{\partial^2 u_j^{(s)}}{\partial x_i \partial x_l} = 0 \quad (2)$$

where the c_{ijkl} 's are the elastic constants of the film and substrate. In isotropic media, there are only two independent elastic constants representing longitudinal and transverse motions in the material. Using collapsed tensor notation²⁸, the coupled equations become

$$\rho \frac{\partial^2 u_y}{\partial t^2} - c_{11} \frac{\partial^2 u_z}{\partial y^2} - c_{44} \frac{\partial^2 u_z}{\partial z^2} + (c_{44} - c_{11}) \frac{\partial^2 u_z}{\partial y \partial z} = 0 \quad (3)$$

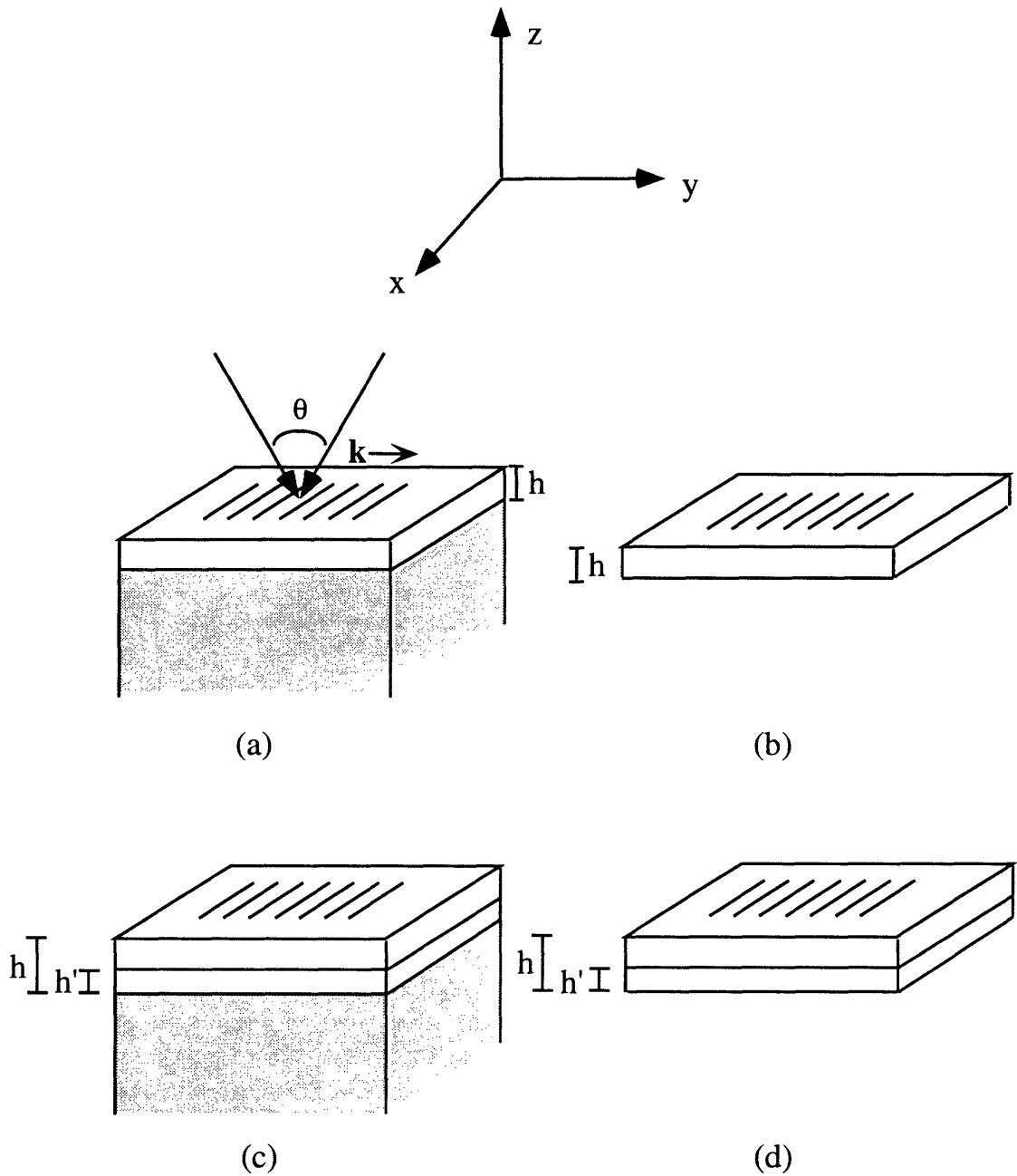


Figure 3.8. The coordinate system used for the calculations of the phase velocity dispersion in supported and unsupported thin film systems. Part (a) shows the geometry used for a single layer supported system where the grating wavevector is aligned along the y-axis and the film thickness is h . Similar geometries for an unsupported single layer film, supported bilayer film, and unsupported bilayer film are shown in parts (b), (c), and (d) respectively. In the bilayer systems, h' is the thickness of the layer adjacent to the substrate while h is the thickness of the entire film.

$$\rho \frac{\partial^2 u_z}{\partial t^2} - c_{11} \frac{\partial^2 u_y}{\partial y^2} - c_{44} \frac{\partial^2 u_y}{\partial z^2} + (c_{44} - c_{11}) \frac{\partial^2 u_y}{\partial y \partial z} = 0 \quad (4)$$

$$\rho^{(s)} \frac{\partial^2 u_y^{(s)}}{\partial t^2} - c_{11}^{(s)} \frac{\partial^2 u_z^{(s)}}{\partial y^2} - c_{44}^{(s)} \frac{\partial^2 u_z^{(s)}}{\partial z^2} + (c_{44}^{(s)} - c_{11}^{(s)}) \frac{\partial^2 u_z^{(s)}}{\partial y \partial z} = 0 \quad (5)$$

$$\rho^{(s)} \frac{\partial^2 u_z^{(s)}}{\partial t^2} - c_{11}^{(s)} \frac{\partial^2 u_y^{(s)}}{\partial y^2} - c_{44}^{(s)} \frac{\partial^2 u_y^{(s)}}{\partial z^2} + (c_{44}^{(s)} - c_{11}^{(s)}) \frac{\partial^2 u_y^{(s)}}{\partial y \partial z} = 0 \quad (6)$$

where the c_{11} 's are the longitudinal elastic constants and the c_{44} 's are the transverse elastic constants of the film and the substrate. For materials with transverse isotropic symmetry, there are five independent elastic constants, so that equations (3) and (4) read

$$\rho \frac{\partial^2 u_y}{\partial t^2} - c_{11} \frac{\partial^2 u_z}{\partial y^2} - c_{44} \frac{\partial^2 u_z}{\partial z^2} - (c_{13} + c_{44}) \frac{\partial^2 u_z}{\partial y \partial z} = 0 \quad (7)$$

$$\rho \frac{\partial^2 u_z}{\partial t^2} - c_{11} \frac{\partial^2 u_y}{\partial y^2} - c_{44} \frac{\partial^2 u_y}{\partial z^2} - (c_{13} + c_{44}) \frac{\partial^2 u_y}{\partial y \partial z} = 0 \quad (8)$$

Derivatives along the x (or 2) direction are ignored since the ISTS experimental geometry does not induce motion in this direction when spatial variations in the excitation grating along the x-direction are ignored.

By assuming that the particle displacements are linear combinations of partial waves of the form,

$$u_y = \alpha_y \exp(ikbz) \exp[ik(y - vt)] \quad (9)$$

$$u_z = \alpha_z \exp(ikbz) \exp[ik(y - vt)] \quad (10)$$

$$u_y^{(s)} = \alpha_y^{(s)} \exp(ikb^{(s)}z) \exp[ik(y - vt)] \quad (11)$$

$$u_z^{(s)} = \alpha_z^{(s)} \exp(ikb^{(s)}z) \exp[ik(y - vt)] \quad (12)$$

where k is the magnitude of the acoustic wavevector and v is the acoustic phase velocity, the coupled equations summarized in equations (1) and (2) can be solved subject to the appropriate boundary conditions at the film interfaces.

The boundary conditions enforce the continuity of the longitudinal and vertical particle displacements, the sagittal shear stress, and the vertical compressional stress at all material interfaces and the vanishing of the sagittal shear stress and vertical compressional stress at all free surfaces. The boundary conditions are summarized in equations (13) through (30).

Film-Substrate System:

$$u_y = u_y^{(s)} \text{ at } z = 0, \quad (13)$$

$$u_z = u_z^{(s)} \text{ at } z = 0, \quad (14)$$

$$T_{yz} = T_{yz}^{(s)} \text{ at } z = 0 \quad (\text{Continuity of Shear Stress}), \quad (15)$$

$$T_{zz} = T_{zz}^{(s)} \text{ at } z = 0 \quad (\text{Continuity of Longitudinal Stress}), \quad (16)$$

$$T_{yz} = 0 \text{ at } z = h, \quad (17)$$

$$T_{zz} = 0 \text{ at } z = h, \quad (18)$$

(for a bilayer system,

$$u_y = u_y' \text{ at } z = h', \quad (19)$$

$$u_z = u_z' \text{ at } z = h', \quad (20)$$

$$T_{yz} = T_{yz}' \text{ at } z = h', \quad (21)$$

$$T_{zz} = T_{zz}' \text{ at } z = h') \quad (22)$$

Unsupported Film System:

$$T_{yz} = 0 \text{ at } z = 0, \quad (23)$$

$$T_{zz} = 0 \text{ at } z = 0, \quad (24)$$

$$T_{yz} = 0 \text{ at } z = h, \quad (25)$$

$$T_{zz} = 0 \text{ at } z = h, \quad (26)$$

(for a bilayer system,

$$u_y = u_y' \text{ at } z = h', \quad (27)$$

$$u_z = u_z' \text{ at } z = h', \quad (28)$$

$$T_{yz} = T_{yz}' \text{ at } z = h', \quad (29)$$

$$T_{zz} = T_{zz}' \text{ at } z = h') \quad (30)$$

In practice, the velocities of the waveguide modes are calculated by searching for the zeroes of the determinant determined by the system of equations generated by the boundary conditions of equations (13) through (22) or equations (23) through (30). In the unsupported single layer film system, this determinant is a function of only the wavevector-film thickness product and the transverse and longitudinal velocities of the film. In the case of the supported single layer film, the determinant is a function of the wavevector-film thickness product and the velocities and densities of the film and substrate. In multiple layer film systems, the relative thicknesses of the individual layers are additional parameters in the determinant. Note

then that for multiple layer systems, there is no simple scaling of the acoustic velocities with the wavevector-thickness product, using either the total thickness of the multilayer assembly or any one of the individual layer thicknesses. This provides one of the distinctive signatures of depth-dependent elastic properties.

In order to analyze the ISTS data, the experimentally determined phase velocity dispersion curves are fit to calculated dispersion curves by varying the velocities of the film using a non-linear least squares Marquardt-Levenberg fitting algorithm²⁹. Unsupported film systems are straightforward to analyze as the only parameters that are allowed to vary are the film velocities. Although supported film systems are somewhat more complicated to analyze as the velocity dispersion depends on the velocities and densities of both the film and the substrate, the substrate properties are often well known and can be fixed when fitting the experimental data. Analysis of ISTS waveguide data have yielded the longitudinal and transverse acoustic velocities in the isotropic films PI2555 and UD4212 and the in-plane and out-of-plane longitudinal velocities and in-plane and out-of-plane transverse velocities in the transverse isotropic films PI2545 and PI2611²¹⁻²³. In the following section we use the above formalism to analyze new data from a series of silicon-supported and unsupported polymer bilayer systems made up of PI2555/PI2545 and PI2555/PI2611. The results indicate that the measured waveguide dispersion contains information that can be used to learn about the depth dependence of the mechanical moduli.

3.4. Results

In Figures 3.9 through 3.11 are shown the phase velocity dispersion curves resulting from ISTS measurements on the supported and unsupported regions of the polymer bilayer structures listed in the experimental section. The error bars are on the order of the symbol sizes.

3.5. Discussion

3.5a. Interpretation of ISTS results on polymer bilayer structures.

In previous ISTS investigations of single layer films made from the polyimides PI2555, PI2545, and PI2611, the acoustic longitudinal and transverse velocities of the isotropic film PI2555 and the in-plane and out-of-plane longitudinal and transverse velocities of the transverse isotropic films PI2611 and PI2545 were determined for films of different thicknesses^{22,23}. The results are summarized in Table 1 where the range given for each velocity reflects the slight differences between films of different thicknesses rather than uncertainty in the results themselves. The uncertainties of the isotropic velocities are on the order of one to two percent while the uncertainties of the anisotropic velocities are on the order of five percent. It should be noted that no correlation between the film thicknesses and the measured velocities was observed in these studies.

Instead of attempting to fit the data from the bilayer samples by using an algorithm that allowed all of the velocities and densities of the different layers to vary in an unrestricted manner, the experimentally determined dispersion curves were analyzed by starting with the velocities determined from the previous single layer ISTS studies. Fits to the

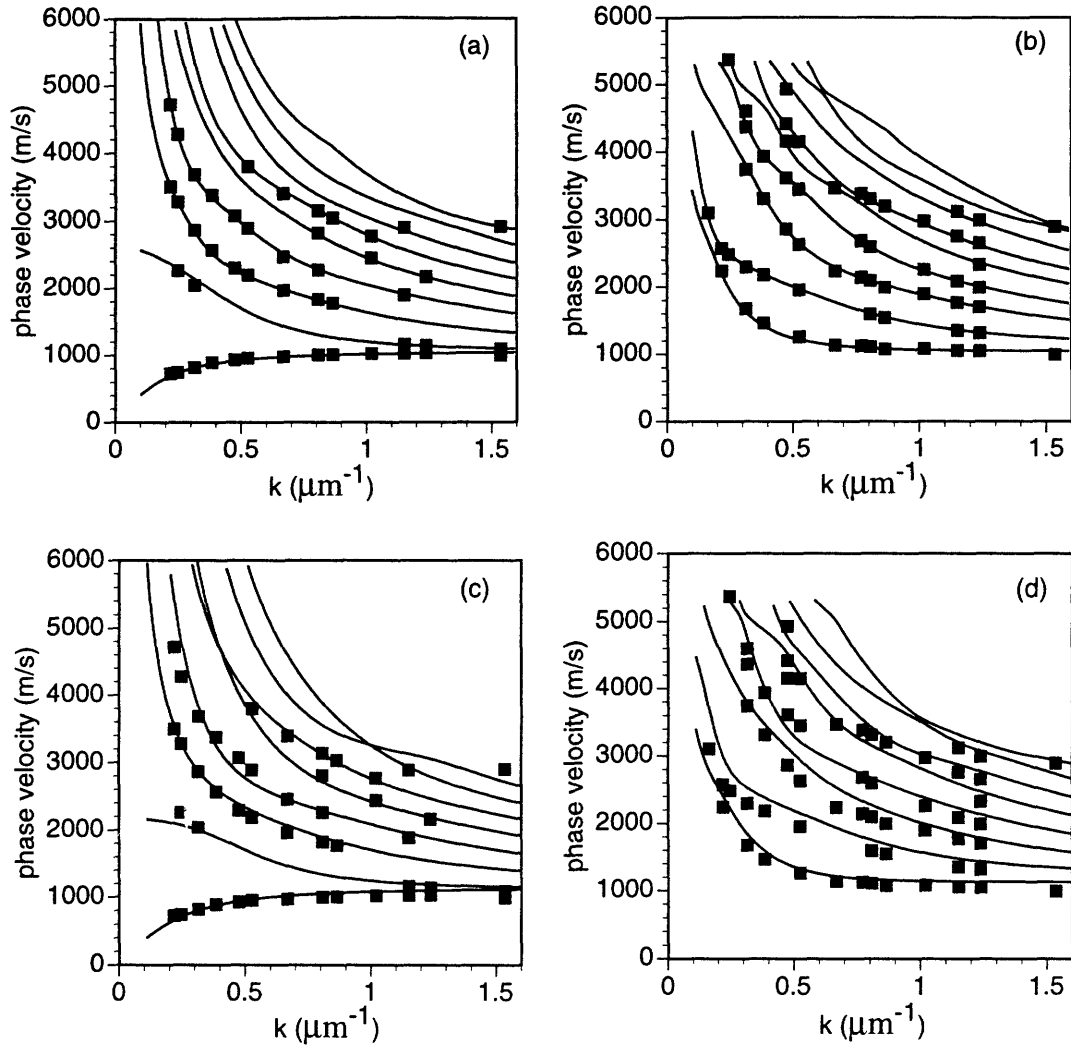


Figure 3.9. Phase velocity dispersion curves for the unsupported and supported polyimide bilayer structure PI2555($2.94\mu\text{m}$)/PI2611 ($3.56\mu\text{m}$). In all of the plots, the experimentally determined velocities are represented by the symbols. In part (a), the best fit to the data from the unsupported region is shown (solid curves) and in part (b), parameters from the unsupported fit were used to calculate the dispersion in the supported region (solid curves). The solid curves in part (c) are the best fit to the data assuming a single layer isotropic film while the solid curves in part (d) are calculated using the best fit parameters of part (c).

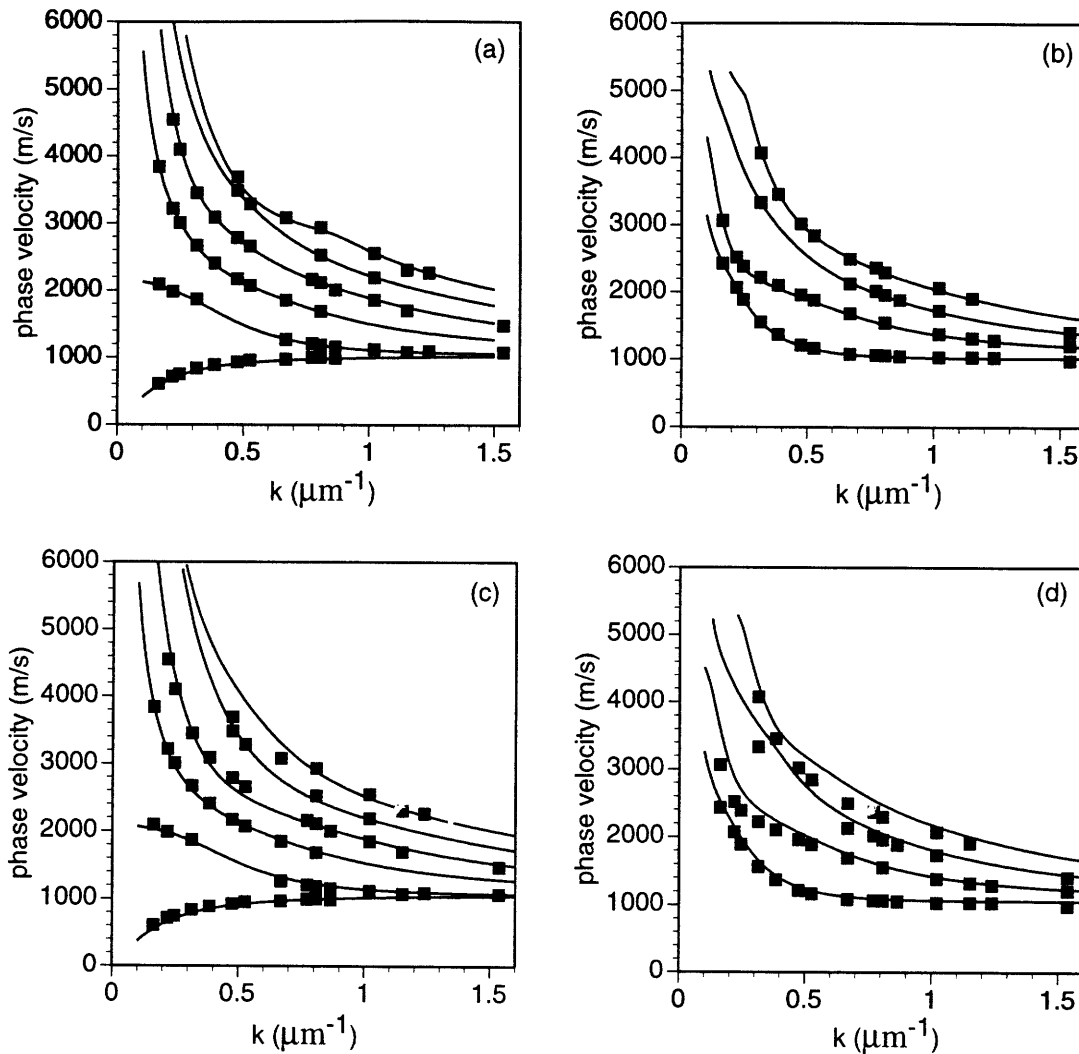


Figure 3.10. Phase velocity dispersion curves for an unsupported and supported polyimide bilayer structure with composition PI2555 ($5.49\mu\text{m}$)/PI2611 ($1.19\mu\text{m}$). In all of the plots, the experimentally determined velocities are represented by the symbols. In part (a), the best fit to the data from the unsupported region is shown (solid curves) and in part (b), parameters from the unsupported fit were used to calculate the dispersion in the supported region (solid curves). The solid curves in part (c) are the best fit to the data assuming a single layer isotropic film while the solid curves in part (d) are calculated using the best fit parameters of part (c). The curves in (c) and (d) show systematic deviations from the data.

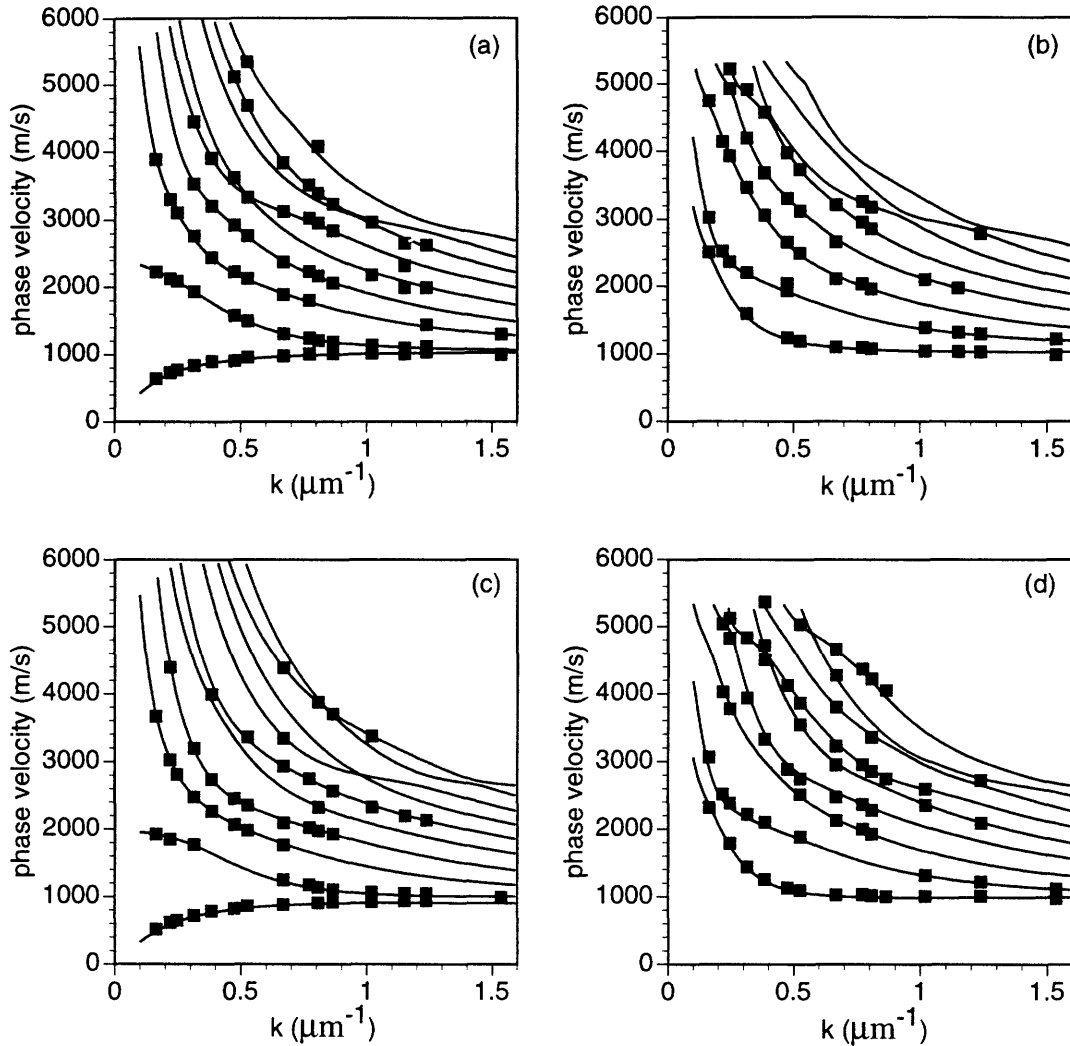


Figure 3.11. Phase velocity dispersion curves for the unsupported and supported polyimide bilayer structure PI2555 ($4.34\mu\text{m}$)/PI2611 ($2.50\mu\text{m}$) (parts (a) and (b)) and PI2555($3.22\mu\text{m}$)/PI2545($2.99\mu\text{m}$) (parts (c) and (d)). In all of the plots, the experimentally determined velocities are represented by the symbols. The solid lines in parts (a) and (c) represent best fits to the data, while solid lines in parts (b) and (d) show simulations using these best fit parameters.

experimentally determined dispersion curves from the unsupported regions of the different bilayer structures were obtained by using the bilayer model of section III C., allowing the velocities of the two layers to vary in a restricted range (+/- 15%) about the velocities listed in Table 1. The thicknesses of the layers were fixed at the values measured using a profilometer while the densities of the polymers were fixed to values determined by density column measurements³⁰. The best fit was determined by the set of velocities that yielded the lowest chi-square. The best-fit velocities are given in Table 2 and the dispersion curves calculated using these best-fit values are shown with the data in Figures 3.9(a), 3.10(a), 3.11(a), and 3.11(c). These best-fit values from the unsupported bilayer systems were used to generate dispersion curves for the supported bilayer systems. These simulated curves generated from the results of the unsupported films with no new adjustable parameters are shown with the data from the supported regions of the bilayer structures in Figures 3.9(b), 3.10(b), 3.11(b), 3.11(d). The measured dispersion curves from the unsupported region and supported region of each film are well described by the bilayer film models given in section III C using velocities that are within ten percent of the velocities determined through independent ISTS measurements on single layer films of PI2555, PI2545, and PI2611. The quality of the fits indicate that no modification of the models for possible imperfect adhesion between the layers or possible diffusion of one layer into the other is required to describe the ISTS data.

In order to demonstrate that ISTS measurements are sensitive to the presence of a second layer, the data from the unsupported regions of the films were fit with a single-layer isotropic layer model each with the same thickness as the total thickness of the corresponding bilayer structure.

Results of the best fits using the single-layer model and the data are shown in Figures 3.9(c) and 3.10(c). From Figures 3.9(c) where data and single-layer best fit curves for the PI2555(2.94 μm)/PI2611(3.56 μm) system are shown, it is obvious that the bilayer structure is readily distinguishable from the single layer isotropic system. Figure 3.10(c) illustrates the same comparison but for a structure with an anisotropic layer of a much smaller relative thickness (PI2611(1.19 μm)/PI2555(5.49 μm)). Although the differences are not as dramatic as in Figure 3.9, Figure 3.10 demonstrates that the single isotropic layer model still provides an inadequate description of the data. In parts (d) of Figures 3.9 and 3.10 are shown the dispersion curves for the corresponding single layer supported system calculated using the best fit isotropic parameters obtained from the unsupported data presented in 3.9(c) and 3.10(c).

The deviations between the data and the single layer dispersion curves calculated for the supported system are even larger than those seen in the single layer fits to the data from the unsupported systems. Since in general motion extends throughout the thickness of the film in the unsupported case, the parameters obtained from the single layer fits to the unsupported data can be considered to represent depth averaged values. It is therefore not surprising that these depth-averaged parameters cannot describe the acoustic waveguide behavior in the corresponding supported system since the presence of the substrate restricts the motion of the film, essentially fixing the motion of the bottom layer and thereby reducing the sensitivity of the dispersion curves to the properties of the bottom layer. This suggests that the failure of the same material parameters to adequately describe the waveguide behavior in the unsupported and supported regions

of the same film system is a strong signature for the existence of depth-dependent properties.

An intuitive understanding of the sensitivity of ISTS experiments to the elastic properties of the film through the depth of the material can be achieved by studying the spatial nature of the waveguide modes probed in the measurements. This is illustrated in Figure 3.12 where grid distortion diagrams for the four lowest order modes at $k=4.0\mu\text{m}^{-1}$ for two unsupported films with different elastic properties are shown. One film is assumed to be a 1μ PI2555 layer while the second film is assumed to be a bilayer structure composed of 0.5μ of PI2555 and 0.5μ of a film chosen to be much stiffer than PI2555 (with $v_{lg} = 5000\text{ m/s}$ and $v_{tr} = 3000\text{ m/s}$). The second layer is chosen to be artificially stiff in order to highlight the differences between film motions of a single layer and bilayer. As seen by the constrained motion of the bilayer structure relative to the single layer, the second layer has the effect of stiffening the entire film. The higher velocities reflect the stiffening of the film and thereby provide a sensitive probe of elastic properties through the depth of the film.

Not only do different modes at a given wavevector probe different regions of the film, the phase velocity of a given mode at different wavevectors can also serve as a depth dependent probe of material properties. For example, the grid distortion diagrams shown above were calculated at a relatively low wavevector where the wavelength is on the order of the film thickness. At large wavevectors where the acoustic wavelength is small compared to the film thickness, the waveguide modes resemble Rayleigh waves which travel on the surfaces of bulk materials. The penetration depth of the Rayleigh mode is a function of the acoustic wavevector. In Figure 3.13 we show how changing the wavevector allows

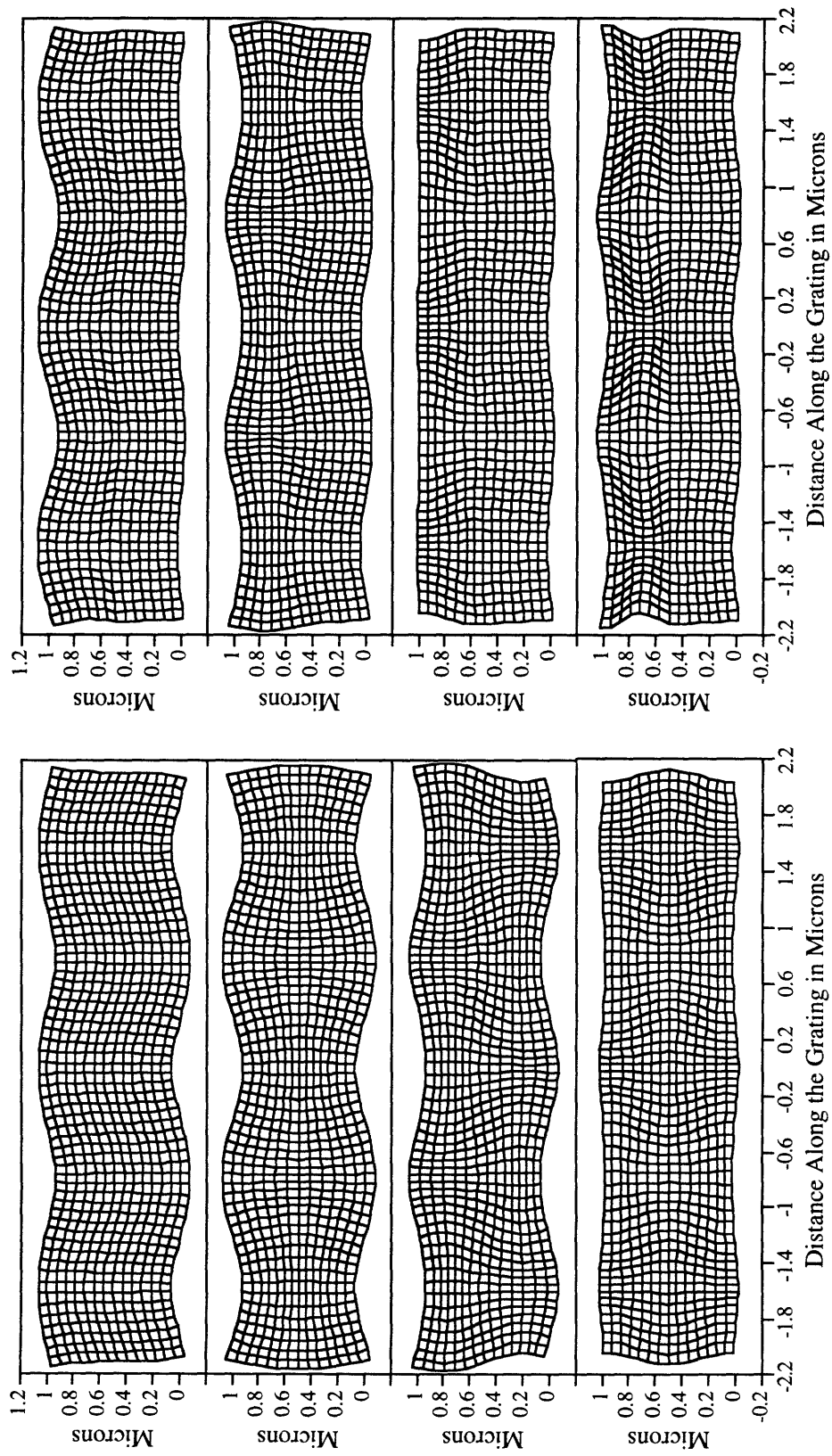


Figure 3.12. Grid distortion diagrams for the four lowest order modes in unsupported single layer and bilayer film systems.

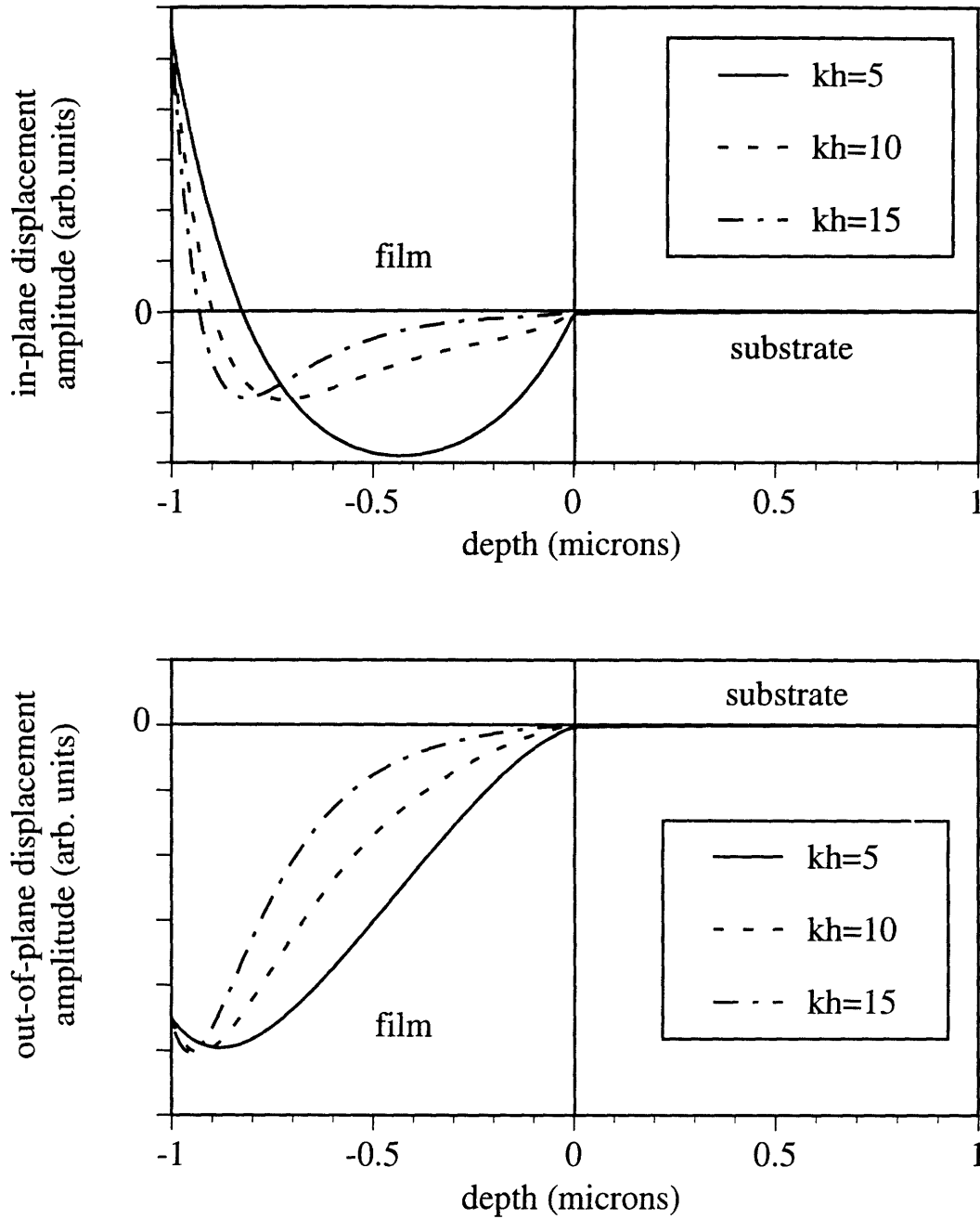


Figure 3.13. Calculated in and out of plane displacement profiles for the Rayleigh wave. As the wavevector increases, the displacements associated with the Rayleigh mode become more localized to the free film surface. This fact can be used to tune the depth sensitivity of the measured Rayleigh wave phase velocity.

us to use the Rayleigh wave as a probe of material properties at different depths. As the wavevector increases, the mode displacements become less and less affected by properties of the film near the substrate as they become localized to the surface of the film.

3.5b. Detection of Very Thin Interfacial Layers

Although the results of part 3.5a demonstrated the effect of an interfacial layer upon ISTS measurements, the analysis was structured around having information on the compositions and properties of the bilayer films. In cases where the composition of the film is not known *a priori*, it is necessary to establish a strategy to optimize ISTS detection of possible interfacial layers.

As briefly mentioned in section III, in single layer films with constant elastic properties, the phase velocities of the allowed waveguide modes scale with the product of the wavevector and thickness. This scaling can be seen in Figure 3.5 where data from a series of films with different thicknesses are shown in single master plots. In contrast to this, in films with an interfacial layer near the substrate, the acoustic wave travels through both layers and no simple relation between the velocity and wavevector-film thickness product can be derived. Therefore, at the most basic level, a breakdown of the phase velocity scaling with wavevector-thickness product is a signature for the possible presence of an interfacial layer.

In order to investigate the sensitivity of ISTS experiments to deviations from the scaling of the wavevector-thickness product, simulations of the phase velocity dispersion behavior as a function of the

relative interfacial layer thickness were carried out. Refractive index measurements have suggested that the thickness of the interfacial layer is typically on the order of 500\AA ^{16,18}. Because the contribution of an interfacial layer to the behavior of the velocity dispersion will decrease as its relative thickness with respect to total film thickness decreases, the effects are best observed in films with thicknesses less than $1\ \mu\text{m}$. The interfacial layer was assumed to be 500\AA thick and to have the elastic properties of PI2611 while the rest of the film was assumed to have the properties of PI2555. In Figure 3.14, we show five sets of dispersion curves for unsupported films of total thicknesses $0.1\ \mu\text{m}$, $0.2\ \mu\text{m}$, $0.3\ \mu\text{m}$, $0.5\ \mu\text{m}$, and $10\ \mu\text{m}$. In both cases, the velocities are plotted versus the product of the wavevector and the total film thickness. We wish to highlight two features illustrated by this figure. First, as expected from previous discussion, in both cases deviations from ideal scaling are unmistakable. In the unsupported case, the second lowest order mode shows the largest deviations at small wavevectors because in this region waveguide motion extends uniformly through the depth of the film (see figure 3.3a) and because this mode is most sensitive to the longitudinal velocity which in PI2611 is significantly larger than that in PI2555. Second, in the supported case, except for the thinnest film, the dispersion curves show a reduced sensitivity to the relative thickness of the interfacial layer. This is because the substrate (which in this example is much stiffer than the polymer) constrains material motion near the interface. As a result, material located near this interface has a small influence on the spatial nature and phase velocity of the modes. This is in contrast to the case of unsupported samples where in general motion extends throughout the thickness of the film. Because of this, depth independent mechanical

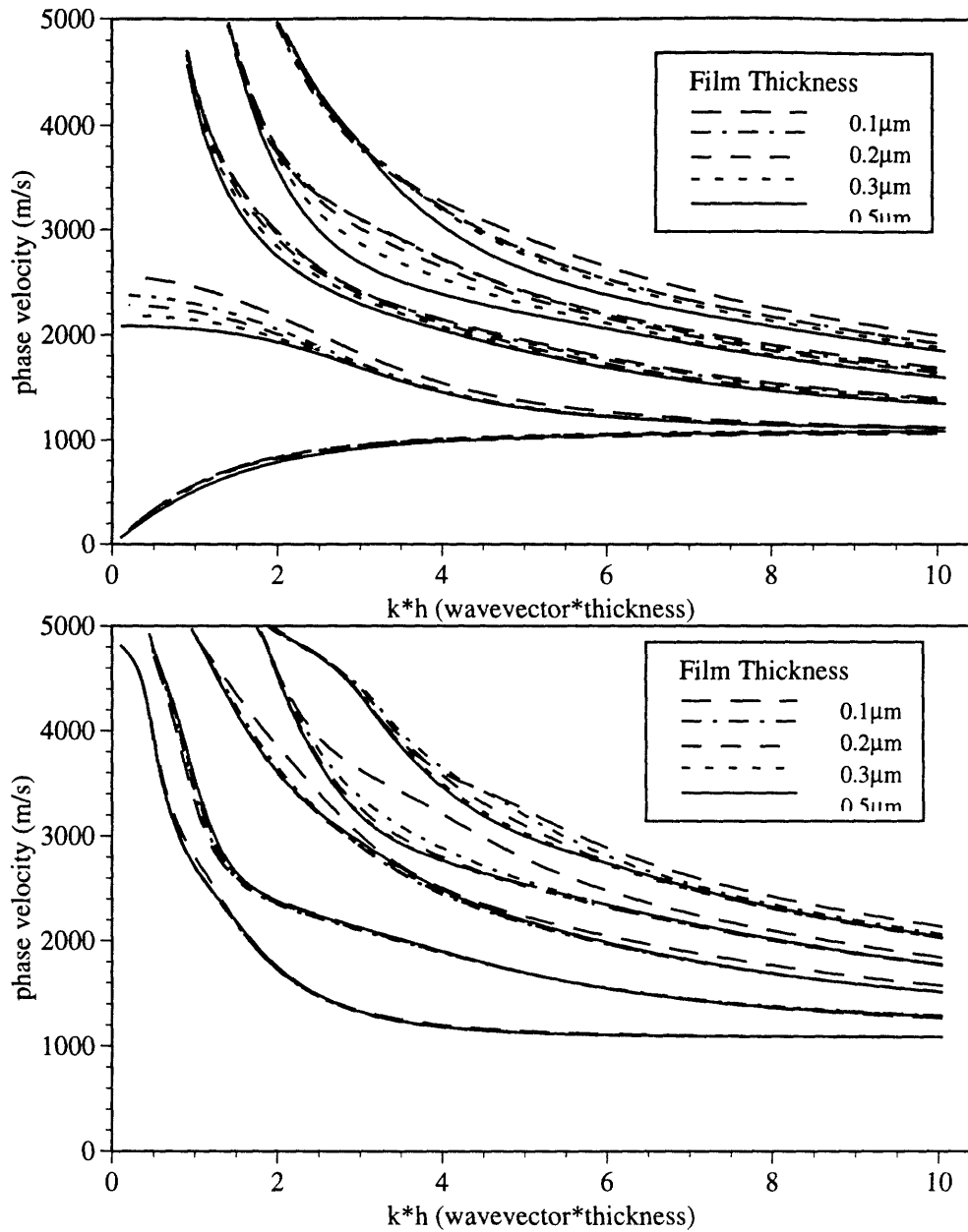


Figure 3.14. Calculated phase velocity dispersion curves for a series of films of different total thicknesses containing a 500\AA thick anisotropic layer adjacent to the substrate. The properties of the interfacial layer are assumed to be that of PI2611 with the in-plane $v_{tr} = 2340$ m/s and $v_{lg} = 3460$ m/s and the out-of-plane $v_{tr} = 1085$ m/s and $v_{lg} = 1960$ m/s and density = 1464 kg/m³. The properties of the rest of the film are assumed to be that of PI2555 with $v_{tr} = 1160$ m/s and $v_{lg} = 2660$ m/s and density = 1400 kg/m³.

parameters determined by fitting data from unsupported films with depth dependent properties will not adequately describe the dispersion of similar films when tightly bound to stiff substrates. This fact provides a signature for depth-dependent moduli, and offers a means for independent determination of material properties near and far from the film-substrate interface.

Both of these features are illustrated in the experimental data from two bilayer samples in figure 3.15. As expected, deviations illustrated here are much larger than experimental uncertainties and are most clearly seen in the second lowest order unsupported mode in the small wavevector times thickness regime. In addition, because of the constraining effect of the substrate, little difference is observed in the data from the supported film.

The results of these simulations suggest that presence of an interfacial layer should be most clearly observable when comparing the experimentally determined phase velocity dispersion of the second lowest order unsupported mode from a relatively thick film to that determined in a film whose thickness is comparable the thickness of the supposed interfacial layer. Of course the differences in the dispersion behavior will depend not only on the relative thickness of the interfacial layer but also on its elastic properties compared to that of the bulk film. Because the elastic properties of this layer are not known, it is difficult to establish an absolute detection limit on the relative thickness of this layer using ISTS experiments. In previous investigations of single-layer polyimide films, no systematic departure from velocity scaling was observed in films that ranged in thickness from $1\mu\text{m}$ to $12\mu\text{m}$. Given the simulations outlined here which used the properties of PI2555 and PI2611 and which predict observable deviations from ideal velocity scaling, we are forced to

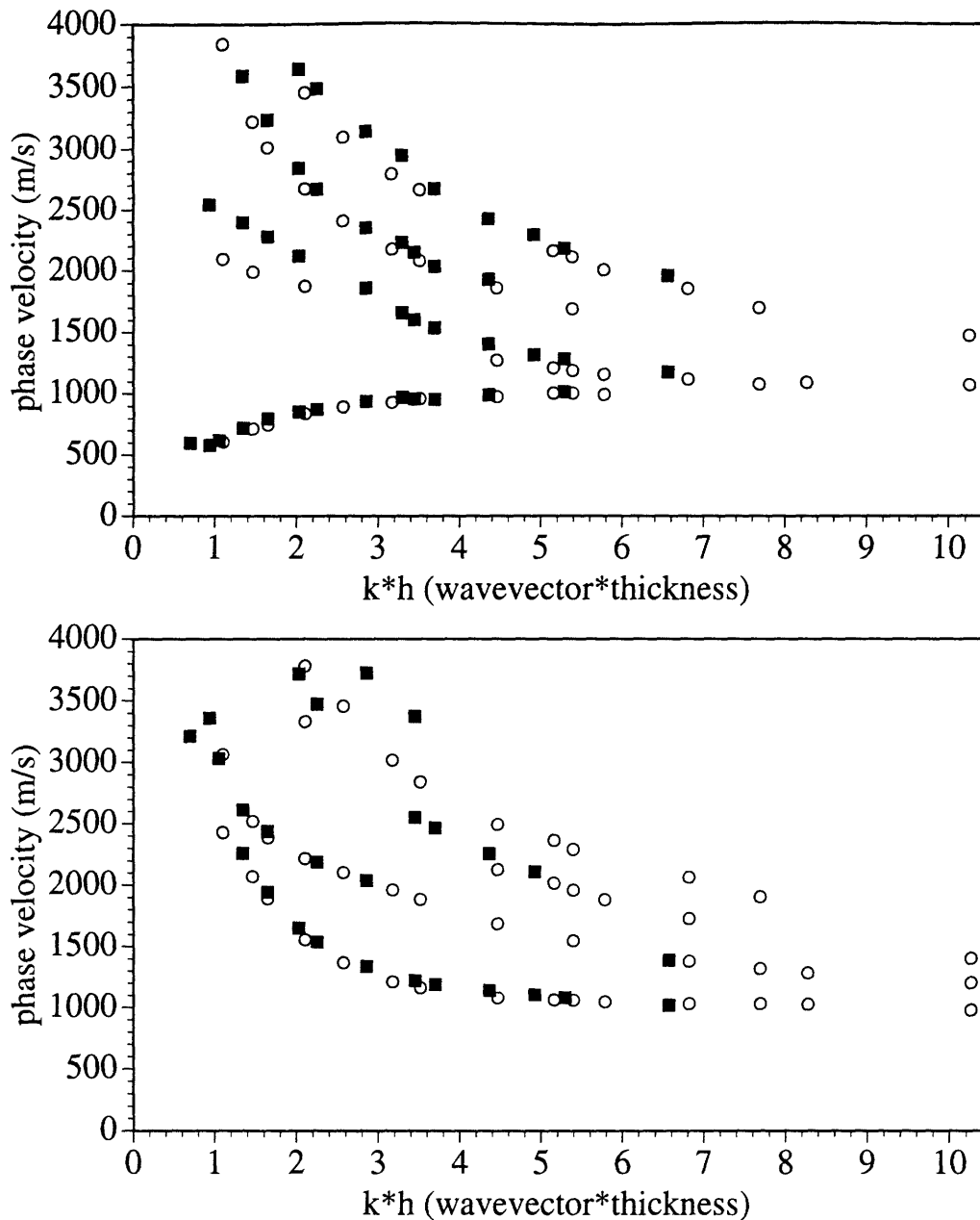


Figure 3.15. Experimentally determined phase velocity dispersion in unsupported (part A) and supported (part B) PI2555(2.05 microns)/PI2611(2.23 microns) (solid squares) and PI2555(5.49 microns)/PI2611(1.19 microns) (open circles) bilayer samples. This figure illustrates the expected breakdown of wavevector times thickness scaling in structures whose mechanical properties vary through the thickness. We also note that waveguide modes in the unsupported case involve motion throughout the thickness of the structure while in the supported case motion near the substrate is restricted. As a result, the unsupported modes are more sensitive to depth dependence in the material properties and therefore show the largest deviations from scaling.

conclude that either the difference between the elastic properties of any interfacial layer and the bulk film are not as great as that between PI2611 and PI2555 or that the interfacial layer is much thinner than 500Å.

As a more concrete illustration of the sensitivity of the dispersion curves in supported and free-standing films to the elastic properties of the interfacial layer, we calculate the sum-of-square errors between the phase velocities of waveguide modes of a film with depth independent mechanical properties and those of a film containing a 500 Å thick interfacial layer as a function of the transverse and longitudinal velocities of the interfacial layer. Although it is believed that for our samples the interfacial layer is quite anisotropic, we assume that it is isotropic in order to facilitate calculating and plotting of the error surface. The results are shown in Figure 3.16. Both films are 0.5 μm thick and the mechanical properties of the reference film are set to be those of PI2555. The mechanical properties of the interfacial layer vary about those of PI2555 while the velocities of the rest of the film are held at those of PI2555. Errors were calculated up to a level determined significant by the ninety percent confidence level F statistic³¹. This surface shows that ISTS can in principle be used to detect the presence of the interfacial layer in this system provided that this layer is characterized by longitudinal and transverse velocities which differ from those of the rest of the film by at least 15 percent.

3.5c. Continuously-Varying Depth-Dependent Elastic Properties

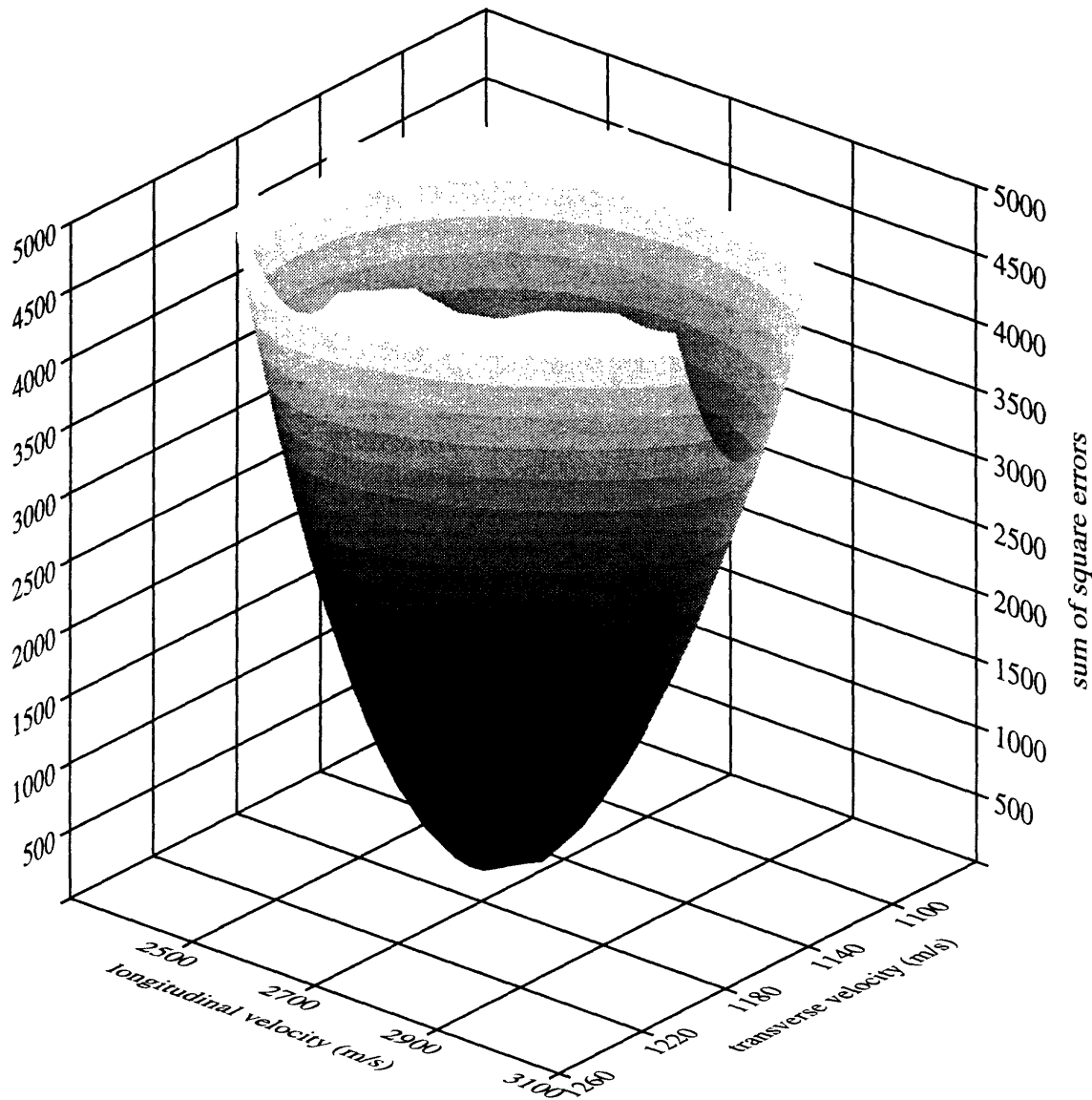


Figure 3.16. Surface plot of the sum of square errors computed for an isotropic model of a silicon supported 0.5 micron film with a 500 Å interfacially modified layer near the substrate. The mechanical properties of this layer vary about those of the rest of the film. The errors are calculated up to a point determined significant through application of a ninety percent confidence level F statistic. The results indicate that the thin buried interfacial layer can be inferred from ISTS data provided that its properties differ from those of the rest of the film by at least 15 percent.

While the interfacial layer model described above was proposed to account for birefringence measurements in spin-cast polyimides, a more realistic model includes properties which vary continuously throughout the thickness of the film. Also, it might be expected that many different processing steps (laser ablation and e-beam polymer curing, for example) would yield films with properties which vary with depth. For these two reasons, in this section we present simulations of waveguide behavior in such films. Although modelling of this system could be achieved by assuming a functional dependence for the elastic constants of the film and numerically solving the equations outlined in section 3.3c where the elastic constants vary with the z-coordinate, the approach taken here is to divide the film into many layers each with different elastic properties. Two cases were considered. The first, with results shown in Figure 3.17, assumes that the film elastic properties change in a linear fashion from those of PI2555 at the top layer to those of PI2611 at the layer near the substrate. The film thickness used is 1 μm and the film is divided into fifteen layers. In the second case, the film properties vary linearly from those of PI2555 to those of an anisotropic film with in-plane $v_{lg} = 3020\text{m/s}$ and $v_{tr} = 1320\text{m/s}$ and the out-of-plane $v_{lg} = 2300\text{m/s}$ and $v_{tr} = 1000\text{m/s}$. These parameters were chosen so that the average longitudinal velocity and average transverse velocity were equal to those of PI2555. Again, the film thickness is 1 μm and the film is divided into fifteen layers.

As might be expected from the discussion in section 3.3b, scaling of the phase velocity with wavevector-film thickness product fails in the case of continuously changing elastic properties. Differences between the depth-independent and the depth-dependent systems are also seen if the

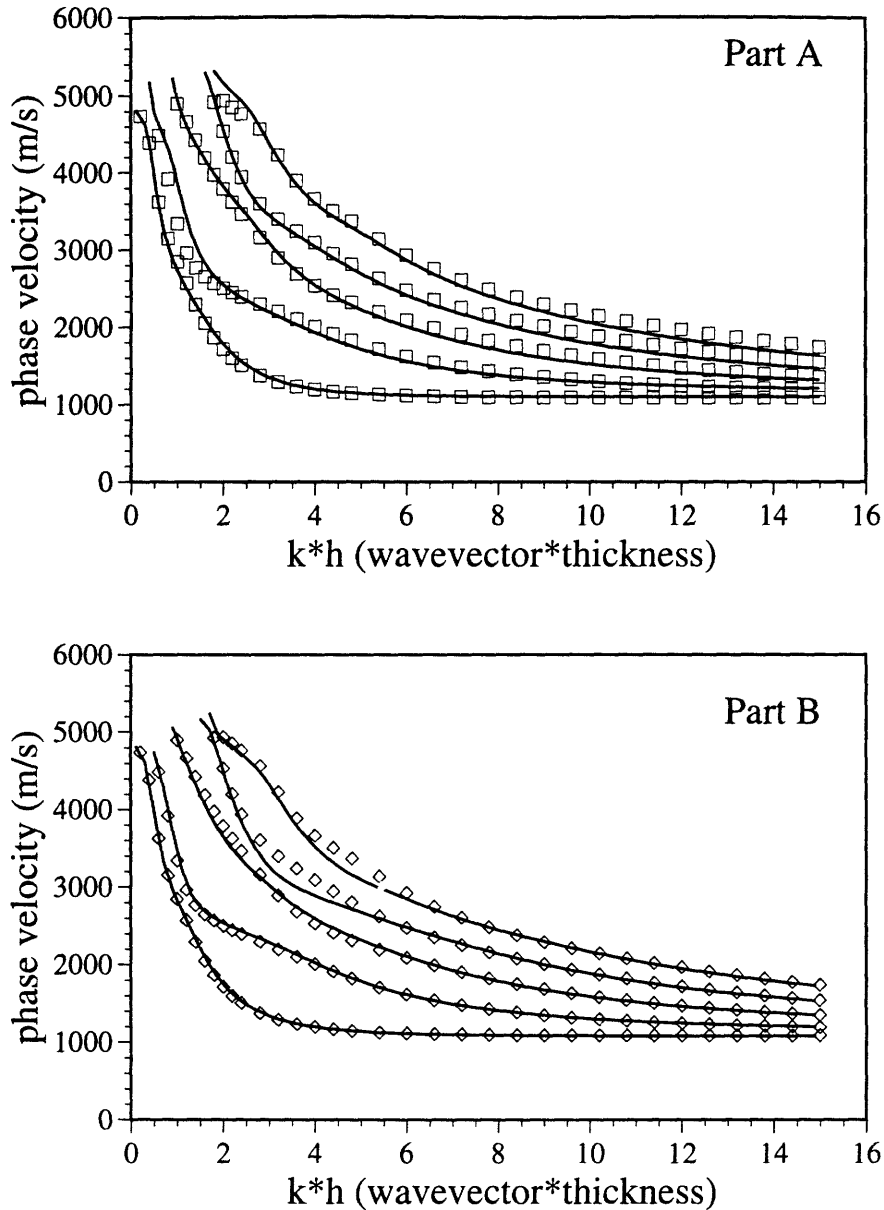


Figure 3.17. Calculated phase velocity dispersion (shown in symbols) in the case of continuously varying elastic constants. The dispersion is calculated by dividing a 1 μm film into 15 layers each with fixed elastic constants. The top layer is set to have the elastic constants of PI2555 while the layer adjacent to the substrate has the elastic constants of PI2611. The elastic constants of the intermediate layers are varied linearly between these limits. Part (a) shows the best fit to the calculated dispersion using an isotropic single layer model. Part (b) shows the best fit to the calculated dispersion utilizing an anisotropic single layer model. Neither of these models yields an accurate description of the data.

dispersion obtained with a stratified model is fit with a model assuming an isotropic or an anisotropic single layer film. In Figure 3.17(a) the result of the best fit of the simulated data to an isotropic model is shown. It is apparent that the fit misses the data severely, especially in the high wavevector range. While this deviation is partly due to the depth varying properties, it also results from the anisotropic nature of the film. In Figure 3.17(b) the best fit of the simulated data to an anisotropic single layer model is shown. The fit describes the data adequately in most regions but misses the data systematically in the region $k = 2.8\mu\text{m}^{-1} - 4.5\mu\text{m}^{-1}$ of the fourth lowest order mode and in the region $k = 4.0\mu\text{m}^{-1} - 6.0\mu\text{m}^{-1}$ of the fifth lowest order mode. Again, we note that the differences illustrated in these figures can be amplified considerably by removing the substrate which tends to confine modal motion to the surface of the film.

In Figure 3.18 are shown results of simulations from the second stratified model. Only a fit to an isotropic model is shown in this figure and the deviations from the actual dispersion are not as great as seen in Figure 3.17. Nevertheless, one distinctive feature of the dispersion of the lowest order mode is noted. For a supported film with constant elastic properties, the dispersion of this lowest order mode will always be monotonically decreasing with increasing wavevector. However in Figure 3.18, we see that the dispersion curve of the lowest order mode increases for wavevectors larger than $k = 4 \mu\text{m}^{-1}$. This is due to the fact that regions of the film near the substrate possess a lower Rayleigh velocity than those near the surface. As the wavevector changes, the Rayleigh wave "samples" different regions of the film which results in a non-constant Rayleigh wave velocity in the large wavevector times thickness limit. This was mentioned in the discussion surrounding Figure 3.13.

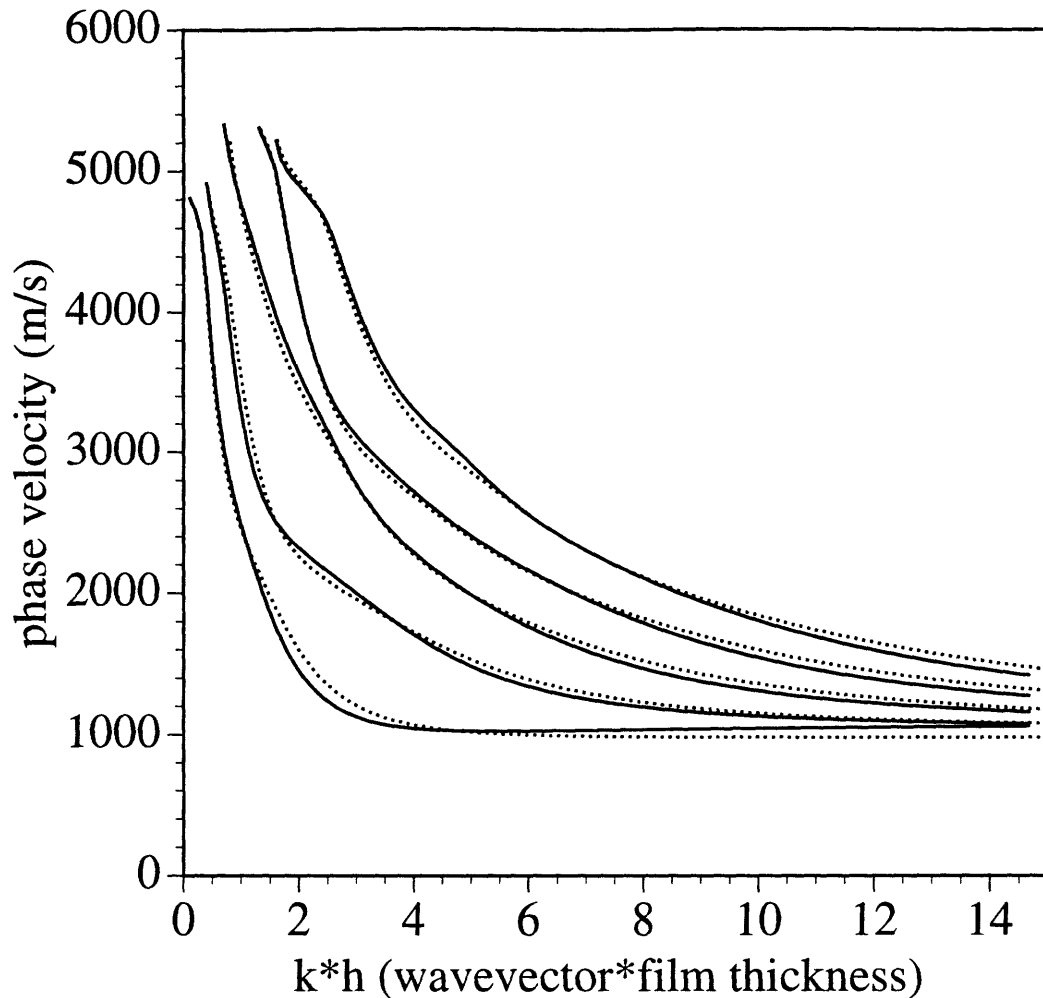


Figure 3.18. Calculated phase velocity dispersion in the case of continuously varying elastic constants (shown by the solid curves). The dispersion is calculated by dividing a 1 μm film into 15 layers each with fixed elastic constants. The top layer is set to have the elastic constants of PI2555 while the layer adjacent to the substrate has in-plane $v_{tr} = 1320$ m/s and $v_{lg} = 3020$ m/s and out-of-plane $v_{tr} = 1000$ m/s and $v_{lg} = 2300$ m/s and density = 1400 kg/m³. The elastic constants of the intermediate layers are varied linearly between the limits. The best fit to a isotropic single layer model is shown by the dashed curves.

3.5d. Limitations of ISTS measurements

To this point, we have argued that the ISTS technique can identify the presence of depth-dependent elastic properties and can be used to set bounds for the elastic properties of a non-ideal film. However, it cannot uniquely define the nature of the depth-dependence. In particular, behavior such as the failure of the phase-velocity dispersion to scale with the wavevector-film thickness product can be caused by either the presence of an interfacial layer or by the existence of continuously changing elastic properties.

In addition to this, the question of the resolution of the technique also arises. Due to experimental uncertainties very subtle variations in the elastic properties may be difficult to detect through ISTS. We note that an additional problem may arise from the possible frequency dependence of the elastic constants. While in general this must be considered, no evidence for frequency dependence of the elastic constants in the 10 - 1000 MHz frequency range probed by ISTS has been observed in any ISTS experiments on polyimides at room temperature. We expect similar results for nearly all solid polymer films since their relaxation spectra are at lower frequency ranges.

3.6. Conclusions

ISTS characterization of multilayer structures has been demonstrated through examination of a series of polyimide bilayer assemblies. These

experiments, along with extensive modelling, have made a strong case for the depth-profiling capabilities of ISTS. The experimental results established the direct effect of a second layer on the measured waveguide mode phase velocities, with the most pronounced effects occurring in modes that involve displacements through the depth of the film. In particular it was found that the dispersion of the second-lowest-order mode in the low wavevector regime in unsupported films was very sensitive to the presence of depth-varying elastic properties. Data from the bilayer structures and simulations of acoustic waveguide behavior in films with a thin interfacial layer established the utility of two simple tests for the existence of depth-dependent moduli. First, it was found that unlike in films with depth-independent properties, the phase velocities in these films fail to scale with the wavevector-thickness product. We also showed that depth independent models cannot consistently account for dispersion observed in both unsupported and supported samples. A quantitative measure of the sensitivity of ISTS to the elastic properties of the interfacial layer showed that for the case examined, a fifteen percent difference between the velocities of the interfacial layer and the velocities of the rest of the film is sufficient for ISTS detection of the interfacial layer. Finally, simulations of the phase velocity dispersion in systems characterized by a continuous change in material properties highlighted the signatures of depth dependent properties. In sum, the experimental results and simulations illustrate the sensitivity of acoustic waveguide behavior characterized in ISTS measurements to material properties through the depth of thin film systems and demonstrate the potential for using ISTS as a depth-profiling tool.

References:

1. S. Groothuis, W. Shroen, and M. Murtuza, Proc. of IEEE 23rd Int. Reliability Physics Symposium, 184 (1985).
2. A.O. Cifuentes and I.A. Shareef, IEEE Transactions on Semiconductor Manufacturing, **5** 128 (1992).
3. Polyimides: Synthesis, Characterization, and Applications (Proceedings of the First Technical Conference on Polyimides), K. Mittal, ed., Plenum Press: New York, 1984.
4. G. Danev, E. Spassova, and K. Popova, Thin Solid Films, **228**, 301 (1993).
5. M. Ree, K.-J. Chen, and D.P. Kirby, J. Katzenellenbogen, and D. Grischkowsky, J. Appl. Phys., **72**(5), 2014 (1992).
6. N. Takahashi, D.Y. Yoon, and W. Parrish, Macromolecules, **17**, 2583 (1984).
7. K. Nakagawa, J. Appl. Polym. Sci., **41**, 2049 (1990).
8. T.P. Russell, H. Gugger, and J.D. Swalen, J. Poly. Sci., Poly. Phys., **21**, 1745 (1983).
9. E. Gattiglia and T. P. Russell, J. Polym Sci., Polym Phys., **27**, 2131 (1989).
10. J.S. Machell, J. Greener, and B.A. Contestable, Macromolecules, **23**(1), 186 (1990).
11. J.C. Coburn, M.T. Pottinger, S.C. Noe, and S.D. Senturia, J. of Polymer Science: Part B: Polymer Physics. **32**, 1271-1283 (1994).
12. J.-H. Jou, P.-T. Huang, H.-C. Chen, and C.-N. Liao, Polymer, **33**(5), 967 (1992).
13. J.-H. Jou and P.-T. Huang, Macromolecules, **24**, 3796 (1991).
14. S.C. Noe, J.Y. Pan, and S.D. Senturia, Polym. Eng. Sci. **32**(15), 1015 (1992).

15. S.C. Noe, Ph.D. Thesis, Massachusetts Institute of Technology, 1991.
16. S. Herminghaus, D. Boese, D.Y. Yoon, and B.A. Smith, *Appl. Phys. Lett.* **59**(9), 1043 (1991).
17. M. Ree, C.-W. Chu, and M.J. Goldberg, *J. Appl. Phys.*, **75**(3), 1410 1994.
18. H. Kasten and G. Strobl, *Fresenius J. Anal Chem.* **346**, 300 (1993).
19. (a) A.E. Yagle and B.C. Levy, *J. Acoust. Soc. Am.* **78**(2), 729 (1985). (b) A.A. Bulgakov, *Solid State Communications.* **55**(10), 869 (1985). (c) T. Kundu, A.K. Mal, and R.D. Weglein, *J. Acoust. Soc. Am.* **77**(2), 353 (1985). (d) T.J. Plona, K.W. Winkler, and M. Schoenberg, *J. Acoust. Soc. Am.* **81**(5), 1227 (1987). (e) S.I. Rokhlin, *Journal de Physique*, **46**(C10), 809 (1985). (f) T.-C. Ma, M. Munidasa, and A. Mandelis, *J. Appl. Phys.* **71**(12), 6029 (1992).
20. (a) H.J. Eichler, P. Gunter, and D.W. Pohl, Laser-Induced Dynamic Gratings (Springer, Berlin, 1986). (b) K.A. Nelson and M.D. Fayer, *J. Chem. Phys.*, **72**, 5202 (1980). (c) K.A. Nelson, D.R. Lutz, M.D. Fayer, and L. Madison, *Phys. Rev. B.*, **24**, 3261 (1981). (d) J.S. Meth, C.D. Marshall, and M.D. Fayer, *J. Appl. Phys.*, **67**, 3362 (1990). (e) J.S. Meth, C.D. Marshall, and M.D. Fayer, *Chem. Phys. Lett.*, **162**, 306 (1989).
21. (a) A.R. Duggal, J.A. Rogers, and K.A. Nelson, *J. Appl. Phys.* **72**, 2823 (1992). (b) A.R. Duggal, J.A. Rogers, and K.A. Nelson, *Appl. Phys. Lett.*, **60**, 692 (1992). (c) J.A. Rogers, S.M. Thesis, Massachusetts Institute of Technology, (1992).

22. J.A. Rogers, L.Dhar, and K.A. Nelson , Appl. Phys. Lett. **65**(3), 312 (1994).
23. J.A. Rogers and K.A. Nelson, J. Appl. Phys., **75** 1 (1994). J.A. Rogers, Y.W. Yang, and K.A. Nelson, Appl. Phys. A. **58**, 523 (1994).
24. J.A. Rogers and K.A. Nelson, J. of Adhesion (in press).
25. C.D. Marshall, I.M. Fishman, and M.D. Fayer, Phys. Rev. B., **43**, 2696 (1991). C.D. Marshall, I.M. Fishman, R.D. Dorfman, C.B. Eom, and M.D. Fayer, Phys. Rev. B., **45**, 10009 (1992).
26. F. Maseeh and S.D. Senturia, Elastic Properties of Thin Polyimide Films, in Polyimides: Materials, Chemistry, and Characterization, C. Ferger, M.M. Khofasteh, and J.E. McGrath, Ed., 1989, Elsevier Science Publishers B.V.: Amsterdam, p. 575.
27. G.W. Farnell and E.L. Adler, Physical Acoustics: Principles and Methods, vol. 9, 35 (1972).
28. J.F. Nye, Physical Properties of Crystals, (Oxford University Press, London 1957).
29. W.H. Press, B.P. Flannery, S.A. Teukolsky, and W.T. Vetterling, Numerical Recipes (Cambridge U.P., Cambridge, 1988).
30. Technial Data Sheet, Dupont Co., Semiconductor Materials, Wilmington, DE. K. Nenov and J. A. Rogers, unpublished results
31. E.M.L. Beale and J. Roy, Sta. B, **22**, 41 (1960). E.S, Pearson and H.O. Harley, Biometrika Tables for Statisticians, (Cambridge University Press, Cambridge, 1970). J.W. Barnes, Statistical Analysis for Engineers, (Prentice Hall, Englewood Cliffs, 1988).

Table 1

	in-plane v_{lg} (m/s)	in-plane v_{tr} (m/s)	out-of-plane v_{lg} (m/s)	out-of-plane v_{tr} (m/s)
PI2555	2540-2715	1126-1191	2540-2715	1126-1191
PI2545	2620-2760	2150-2270	1190-1300	915-960
PI2611	3540-3620	2300-2380	2010-2080	1120-1150

Table 2

	PI2555		PI2545				PI2611			
	(m/s)		in-plane (m/s)		out-of-plane (m/s)		in-plane (m/s)		out-of-plane (m/s)	
	Vlg	Vtr	Vlg	Vtr	Vlg	Vtr	Vlg	Vtr	Vlg	Vtr
5.49 μ PI2555/ 1.19 μ PI2611	2515	1078					3559	2175	2034	1078
4.34 μ PI2555/ 2.50 μ PI2611	2583	1089					3512	2176	2017	1080
3.22 μ PI2555/ 2.99 μ PI2545	2624	1072	2537	1954	1293	941				
2.94 μ PI2555/ 3.56 μ PI2611	2464	1112					3660	2258	2096	1090

Chapter 4. Impulsive Stimulated Thermal Scattering Spectroscopy of Piezoelectric and Metallic Multilayer Systems

4.1 Introduction

In recent years the technology for synthesizing piezoelectric thin films has improved dramatically and as a result there has been a great deal of interest in their potential use as surface acoustic wave (SAW) devices such as resonators, filters, and delay lines^{1,2}. Considerable attention has been focussed upon the possibility of integrating acoustic wave devices with electronic components or semiconductor technology. For example¹ the weakly piezoelectric semiconductor gallium arsenide has been used as an acoustic charge transport device for high-speed analog signal processing applications. In this device, charge packets are transported by the propagating potential associated with the surface acoustic wave of the bulk material. However since GaAs is only weakly piezoelectric, large amounts of acoustic power are required for charge transport. A strongly piezoelectric film deposited upon the GaAs surface would potentially reduce the acoustic power required. Knowledge of the acoustic wave properties of piezoelectric films and the associated electric fields and potentials are therefore crucial to the design and fabrication of useful thin film SAW devices. In the following, we use a non-contact, real-time, optical technique known as impulsive stimulated thermal scattering (ISTS) spectroscopy, to characterize acoustic waveguide modes in a 1200Å film of

the piezoelectric material lead zirconium titanate (PZT) deposited upon a metallic multilayer system.

4.2 Experimental

In ISTS experiments^{3,4}, two ultrashort excitation pulses are overlapped temporally and spatially in an absorbing sample to form an optical interference grating characterized by a scattering wavevector \mathbf{k} . The grating wavevector magnitude k , determined by the difference between the wavevectors of the two excitation pulses, is calculated according to $k = 4\pi\sin(\theta/2)/\lambda$, where λ is the wavelength of the excitation light and θ is the angle between the two excitation beams. The formation of a sudden temperature grating due to optical absorption of the excitation light followed by nonradiative relaxation leads to thermal expansion within the sample. Counterpropagating acoustic waves in addition to a steady-state density modulation result from the thermal expansion. The time-dependent material response is monitored through the diffraction of probe laser light off of the density grating. The experimental setup is shown in Figure 4.1.

The two excitation pulses originate from a Q-switched, mode-locked, and cavity-dumped Nd:YAG laser yielding a 1 mJ, 100 ps pulse at 1064 nm. The light is first frequency doubled and then the doubled light is mixed with the remaining 1064 nm light to yield pulses at 355 nm. A cw argon-ion laser is used to provide the probe light. The advantage of using a cw probe rather than a pulsed probe is that by electronically analyzing the diffracted cw probe light, the complete material response over the entire time window may be collected in a single excitation-probe pulse sequence. The use of a pulsed probe requires multiple excitation-probe

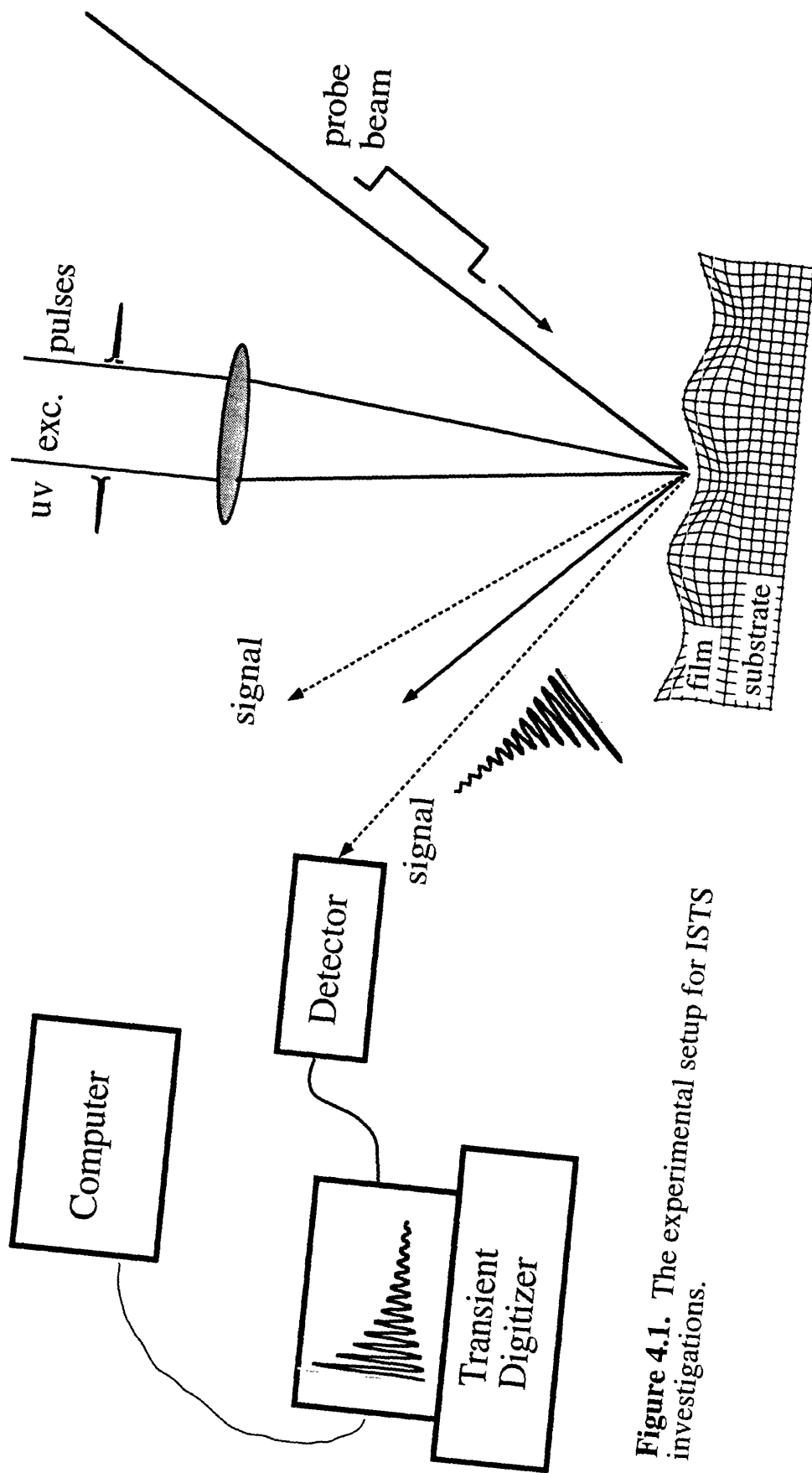


Figure 4.1. The experimental setup for ISTS investigations.

pulse sequences with variable time delays between the excitation and probe pulses. The diffracted light is detected by a fast photodiode with a bandwidth of 2 GHz and the photodiode signal is recorded by a transient digitizer with a bandwidth of 1 GHz.

The PZT sample was a 1200 Å film of 53/47 PZT deposited upon 1000 Å layers of platinum and titanium. The metallic layers were evaporated upon a 1000 Å layer of SiO₂ on the <100> surface of a silicon wafer. Experiments were also conducted on the bare metallic multilayer system.

4.3 Experimental Results

Experiments were conducted on the PZT film at the scattering angles 0.33°, 0.67°, 0.83°, 1.00°, 1.28°, 1.50°, 1.67°, 2.05°, 2.25°, 2.33°, 2.45°, 2.57°, 2.80°, 2.97°, 3.38°, 3.57°, 3.87°, 3.92°, 4.12°, 4.55°, 4.60°, and 5.13° corresponding to wavevectors 0.10, 0.21, 0.26, 0.31, 0.35, 0.46, 0.52, 0.63, 0.70, 0.72, 0.76, 0.79, 0.87, 0.92, 1.05, 1.10, 1.19, 1.21, 1.27, 1.40, 1.42, and 1.58 μm⁻¹. The angles were measured mechanically with a calibrated rotation stage with uncertainties estimated at ±0.05°. It should be noted that the frequencies of the acoustic oscillations at wavevectors higher than 1.6 μm⁻¹ exceed the bandwidth of the present experimental system.

Typical data are shown in Figures 4.2 and 4.3. The data are the result of the average of 100 laser shots, with a total data collection time of thirty seconds. The oscillations reflect the acoustic waves initiated by the thermal expansion in the sample. The phase velocities can be calculated from the observed acoustic frequencies. The very low frequency mode

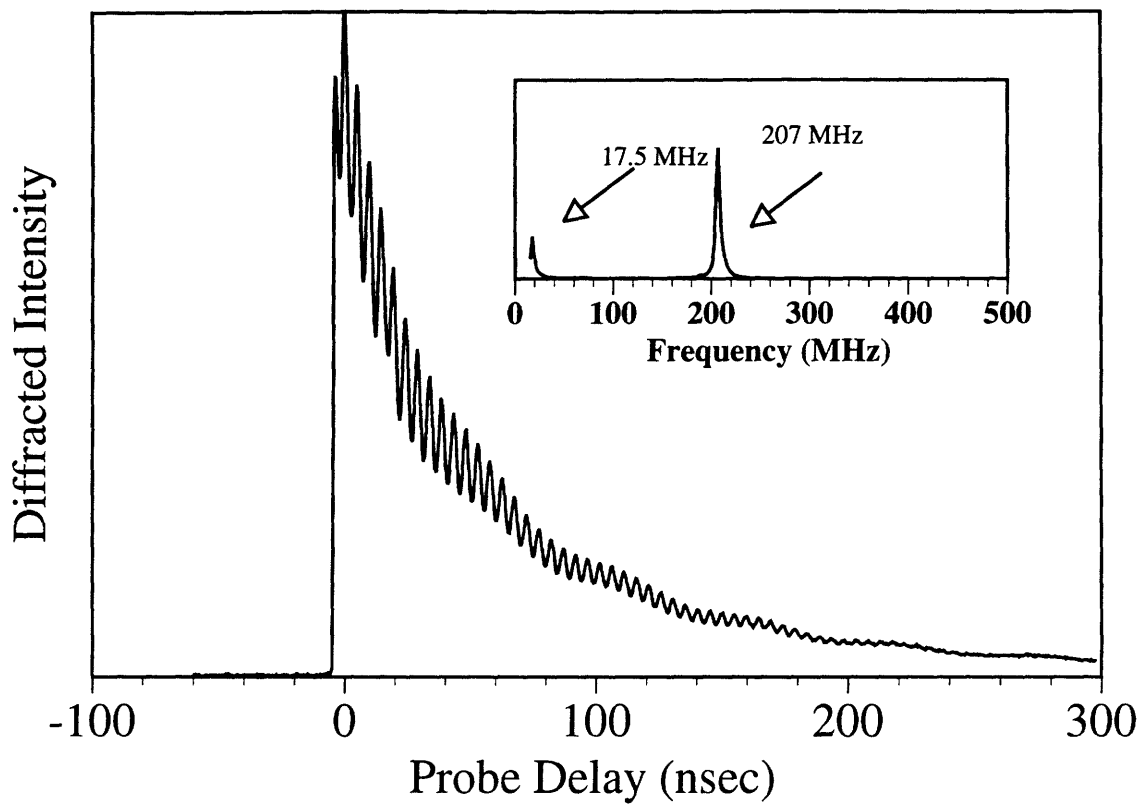


Figure 4.2. ISTS data from a 1200Å film of PZT. The inset shows the Fourier transform of the data.

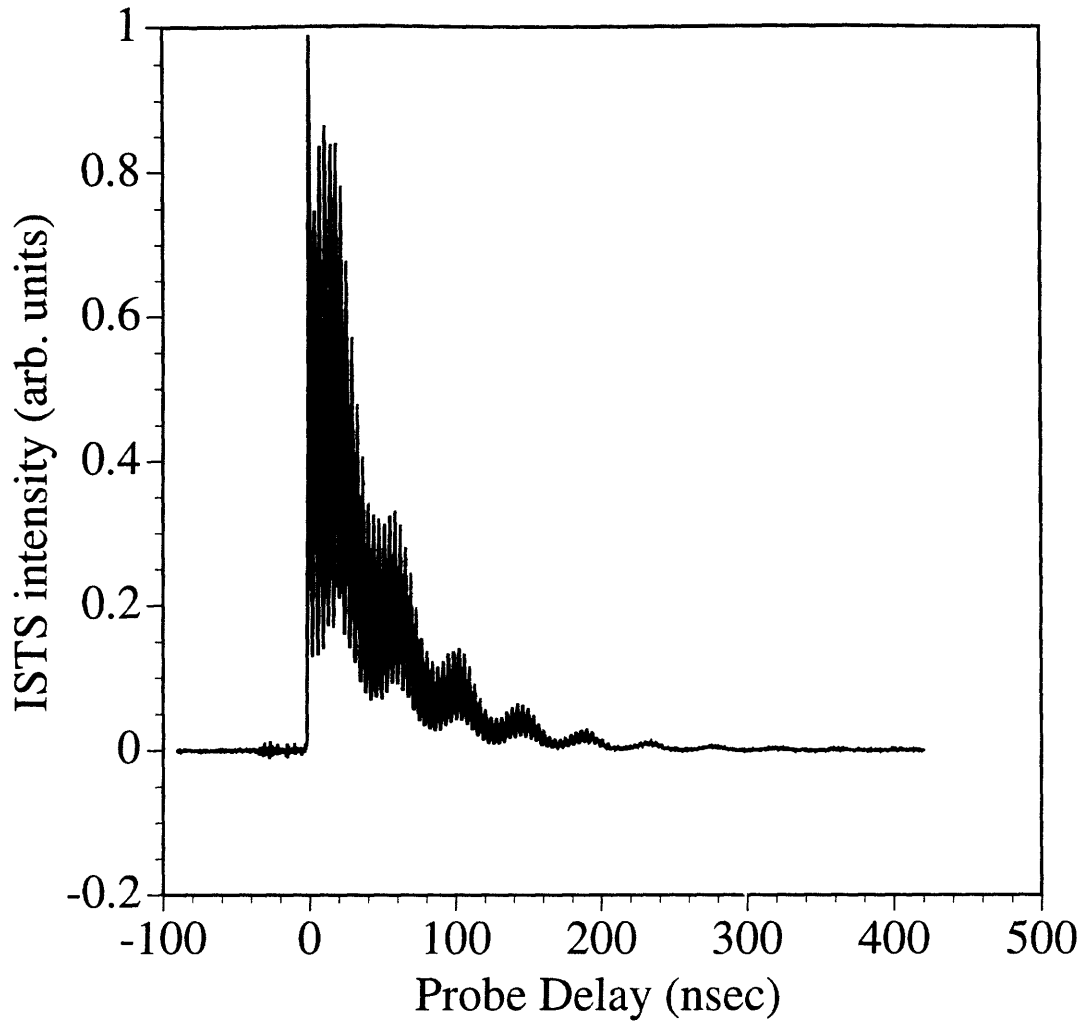


Figure 4.3. ISTS data in the Pt/Ti/SiO₂/Silicon multialyer

seen at 17.5 MHz in the PZT film is due to a mode that propagates at the interface between the ferroelectric material and the air and are ignored for the purposes of this paper. The velocities for the PZT thin film are plotted versus the product of the scattering wavevector and film thickness in Figures 4.11 and 4.12 of the discussion section. The uncertainty in the calculated phase velocities is 5%.

4.4 Theory

We begin this section with a discussion of the acoustic waveguide behavior in a single layer piezoelectric film tightly bound to a semi-infinite dielectric substrate^{5,6}. In the case of piezoelectric materials, there exists a coupling between elastic and electromagnetic waves. In other words, a term proportional to the electric field is introduced into the mechanical equation of motion that governs the material displacements and a term proportional to the mechanical strain is introduced into Maxwell's equations. The result is that accompanying the elastic waves is an electric field and associated with the electromagnetic waves is a mechanical strain. Typically, the velocities of the elastic waves are several orders of magnitude smaller than the velocities of the electromagnetic waves so that the effect of the electric field associated with the electromagnetic waves on the elastic waves is negligible compared to the effect of the electric field generated by the strain, greatly simplifying the analysis of acoustic wave propagation in piezoelectric materials. The neglect of the interaction between the electromagnetic solutions and the elastic solutions is known as the "quasistatic" approximation as the electric field generated by the strain is static when compared to the electromagnetic propagation.

In the quasistatic approximation, the general coupled field equations,

$$\nabla \cdot \mathbf{c}^E : \nabla_s \mathbf{u} = \frac{\partial^2 \mathbf{u}}{\partial t^2} + \nabla \cdot (\mathbf{e} \cdot \mathbf{E}) \quad (1)$$

$$-\nabla \times \nabla \times \mathbf{E} = \mu_0 \boldsymbol{\varepsilon}^s \cdot \frac{\partial^2 \mathbf{E}}{\partial t^2} + \mu_0 \mathbf{e} : \nabla_s \frac{\partial^2 \mathbf{u}}{\partial t^2} \quad (2)$$

become

$$\rho \frac{\partial^2 u_j}{\partial t^2} - c_{ijkl} \frac{\partial^2 u_k}{\partial x_i \partial x_l} - e_{kij} \frac{\partial^2 \phi}{\partial x_i \partial x_k} = 0 \quad (3)$$

$$e_{ikl} \frac{\partial^2 u_k}{\partial x_i \partial x_l} - \varepsilon_{ik} \frac{\partial^2 \phi}{\partial x_i \partial x_k} = 0 \quad i, j, k, l = 1, 2, 3, \quad (4)$$

where the clamped elastic stiffness tensor \mathbf{c}^E , the piezoelectric tensor \mathbf{e} , and the permittivity tensor $\boldsymbol{\varepsilon}$ are written in matrix form. In the film and the substrate, the particle displacements u_i along the coordinate axes x_i are then derived from the elastic wave equation (equation (1)) and the anisotropic Laplace's equation (equation (2)) where ρ is the density of the medium and ϕ is the electric potential. The system geometry is shown in Figure 4.4. The particle displacements and the potential are assumed to be linear combinations of waves of the form

$$u_j = \alpha_j \exp(ikb x_3) \exp[ik(x_1 - vt)] \quad (5)$$

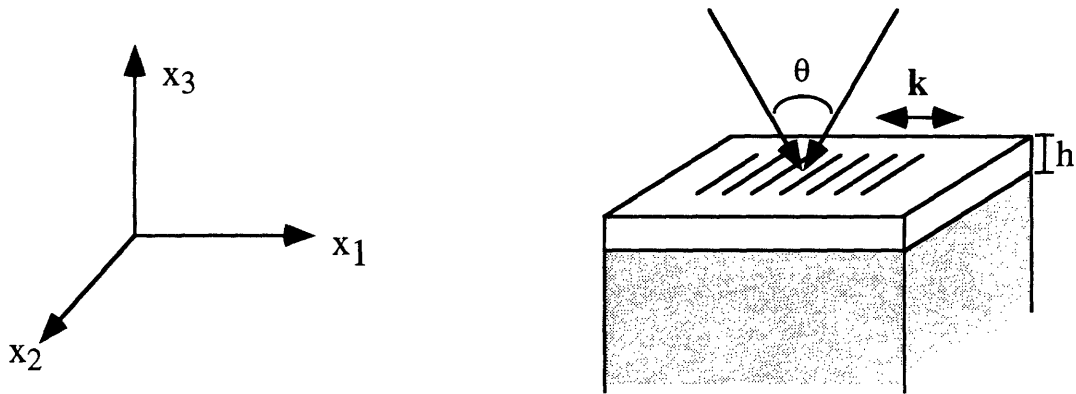


Figure 4.4. The coordinate system used for the calculations of the phase velocity dispersion in a supported piezoelectric film. k is the grating wavevector aligned along the x_1 axis and h is the film thickness.

$$\phi = \alpha_4 \exp(ikbx_3) \exp[ik(x_1 - vt)]. \quad (6)$$

The solutions to equations (1) and (2) are obtained by enforcing the following mechanical and electrical boundary conditions. At the free surface $x_3 = 0$, the vanishing of the sagittal shear stress, $T_{31} = 0$, the vanishing of the compressional shear stress, $T_{33} = 0$, and the continuity of the electric displacement $D_3 = k\epsilon_0\phi$ are required. At the film-substrate interface $x_3 = h$, the continuity of the vertical particle displacement, $u_3 = u_{3\text{surface}}$, the continuity of the longitudinal particle displacement $u_1 = u_{1\text{surface}}$, the continuity of the sagittal shear stress $T_{31} = T_{31\text{surface}}$, the continuity of the compressional shear stress, $T_{33} = T_{33\text{surface}}$, and the continuity of the electric displacement, $D_3 = D_{3\text{surface}}$ are required.

In order to illustrate aspects of acoustic waveguide behavior in piezoelectric materials, we consider the system of a silicon-supported PZT film. The PZT film is c-axis oriented and therefore assumed to have hexagonal symmetry. The elastic, piezoelectric, and permittivity constants used in the calculations are from Reference 7. In figure 4.5 are shown the longitudinal and vertical particle displacements through the depth of the film-substrate systems at several values of the wavevector-film thickness product, $kh=5.0$, $kh=10.0$, and $kh=15.0$, for the lowest order mode. As expected, as the wavevector-thickness product increases, the particle displacements become more and more localized to the free surface of the film. Also shown are the electric displacements ($D = \epsilon E + P$) induced by these acoustic motions. The depth dependence of the electric displacements resemble that of the particle displacements indicating that the majority of the polarization originates from the material strain. Shown in Figure 4.6 are the electric fields associated with the material motions. The electric

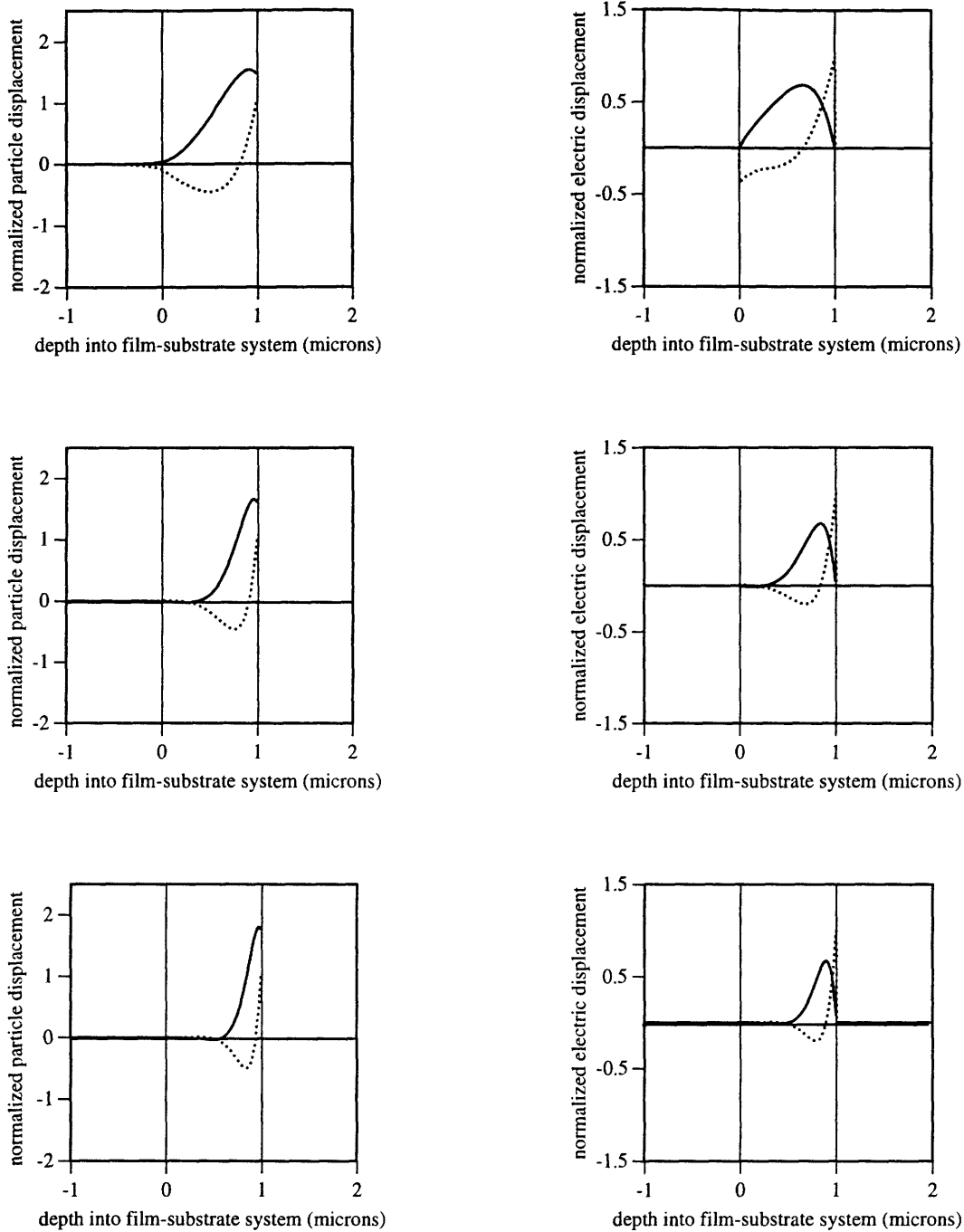


Figure 4.5. The in-plane (dashed lines) and out-of-plane (solid lines) components of the particle displacements and the electric displacements in a silicon-supported PZT film at $kh=5.0$ (top frames), $kh=10.0$ (middle frames), and $kh=15.0$ (bottom frames).

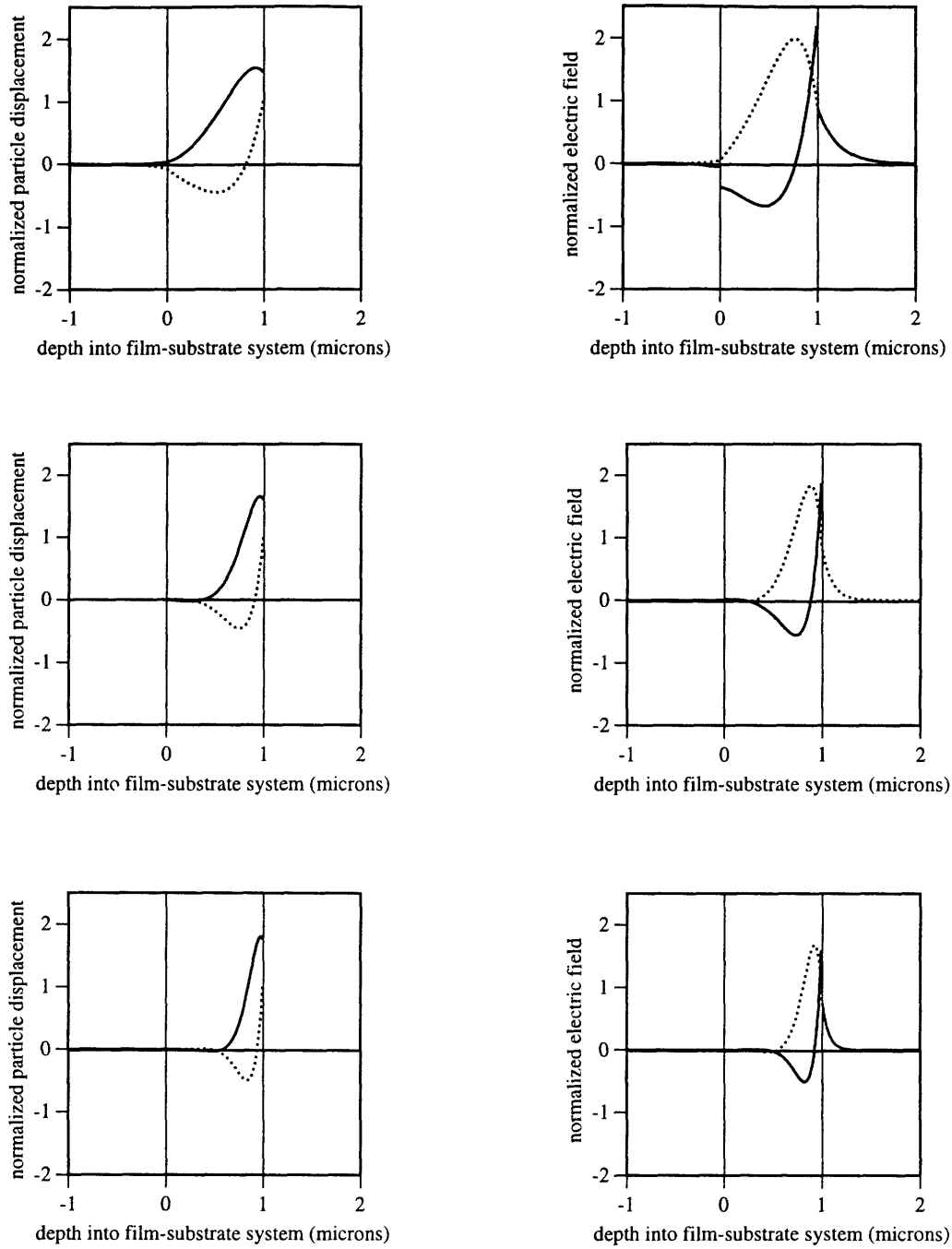


Figure 4.6. The in-plane (dashed lines) and out-of-plane (solid lines) components of the particle displacements and the electric field in a silicon-supported PZT film at $kh=5.0$ (top frames), $kh=10.0$ (middle frames), and $kh=15.0$ (bottom frames).

fields extend outside of the film-substrate system decaying within one wavelength. The longitudinal components of the electric fields are continuous at the interfaces while the vertical components are discontinuous indicating a buildup of charge at the interfaces. The particle displacements and electric fields for the lowest three order modes at a wavevector thickness product of 3.0 are shown in Figure 4.7. The particle displacements become more complicated for the higher order modes and involve significant displacements into the substrate. Figures 4.8 and 4.9 display the electric field vectors along the wavevector region and through the depth of the film for the lowest two order modes at $kh=1.5$ and the lowest three order modes at $kh=3$.

In Figure 4.10(a) through (d) are shown the effect of the different piezoelectric constants on the acoustic phase velocities. In Figures 4.10(a) we compare the dispersion curves calculated for a silicon-supported PZT film with the curves calculated for a non-piezoelectric film with the same elastic properties of PZT. The obvious effect is the stiffening of the piezoelectric film. As seen from the velocity of the lowest order mode at large wavevectors, the Rayleigh velocity of the piezoelectric film is almost 300 m/s higher than that of the nonpiezoelectric film. Figures 4.10(b) through (d) demonstrate the sensitivity of the dispersion curves to each of the three independent piezoelectric constants. In Figure 4.10(b), where e_{31} has been set to zero, the dispersion curves are only slightly affected. From Figures 4.10(c) and (d) where e_{33} and e_{15} individually have been set to zero, it is apparent that e_{15} has the largest effect on the acoustic phase velocities. The small effect of e_{31} may be considered to be a result of its small magnitude when compared to e_{33} and e_{15} . The fact that e_{15} has a stronger influence upon the velocities than e_{33} is due to the motions to

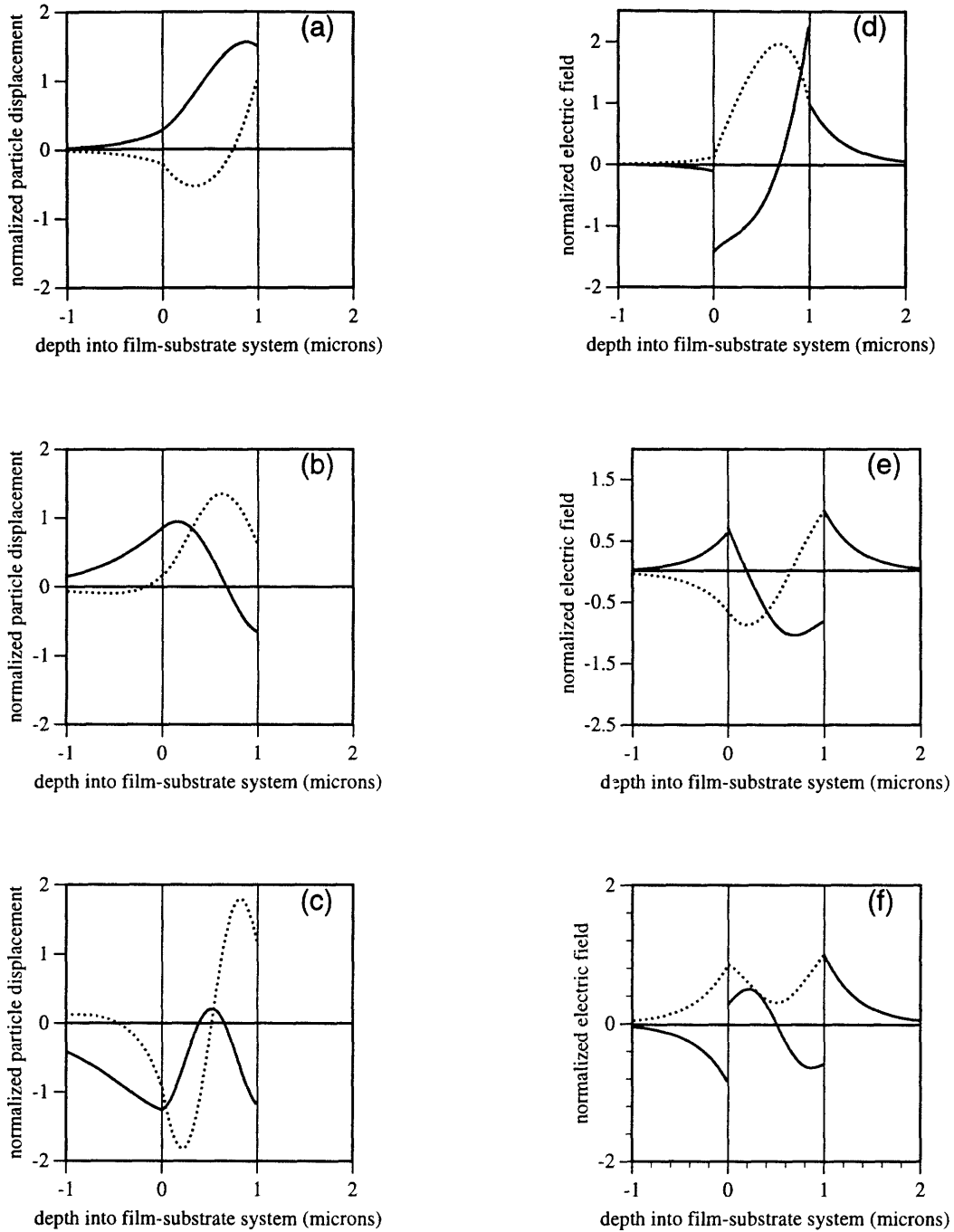


Figure 4.7. The in-plane (dashed lines) and out-of-plane (solid lines) components of the particle displacements and the electric field in a silicon-supported PZT film at $kh=3.0$ for the lowest order mode (top frames), second lowest order mode (middle frames), and third lowest order mode (bottom frames).

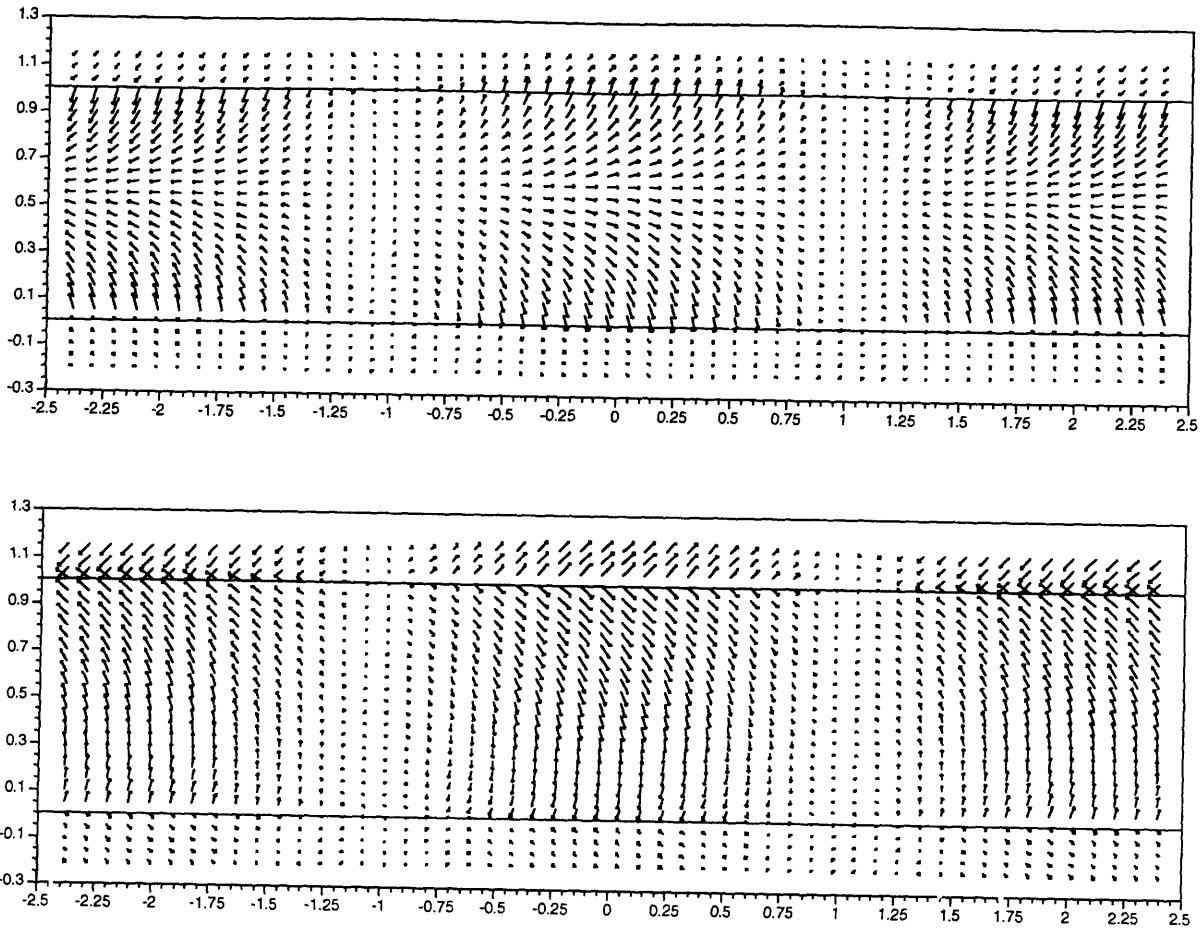


Figure 4.8. The electric field vectors associated with the lowest two order modes in a silicon-supported PZT film at $kh=1.5$.

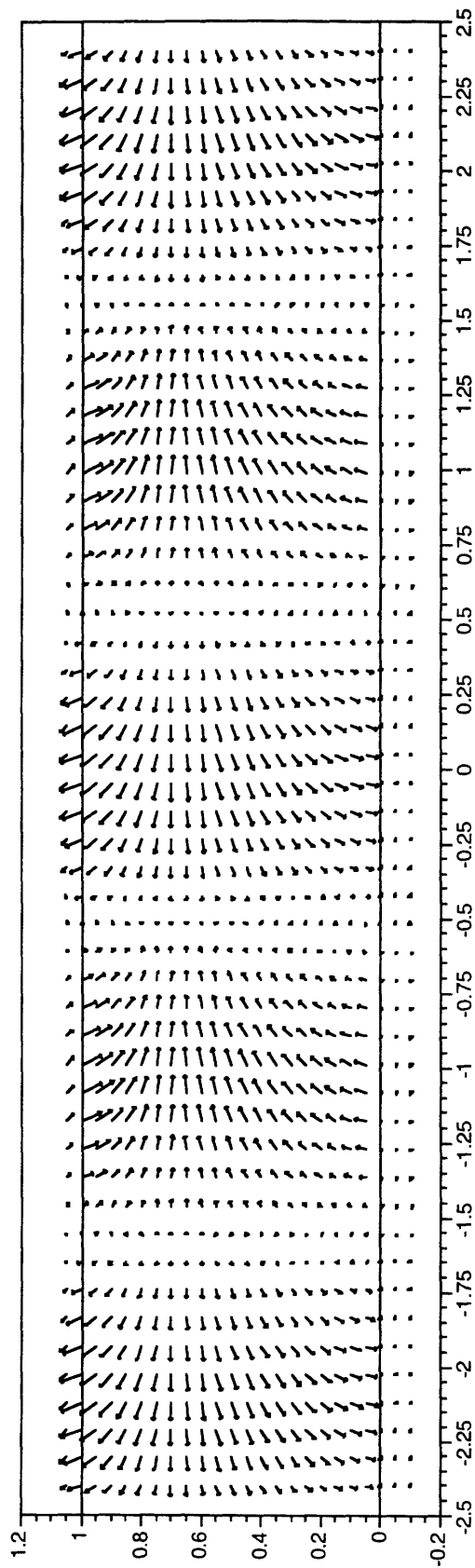


Figure 4.9 The electric field vectors associated with the lowest order mode at $kh=3.0$

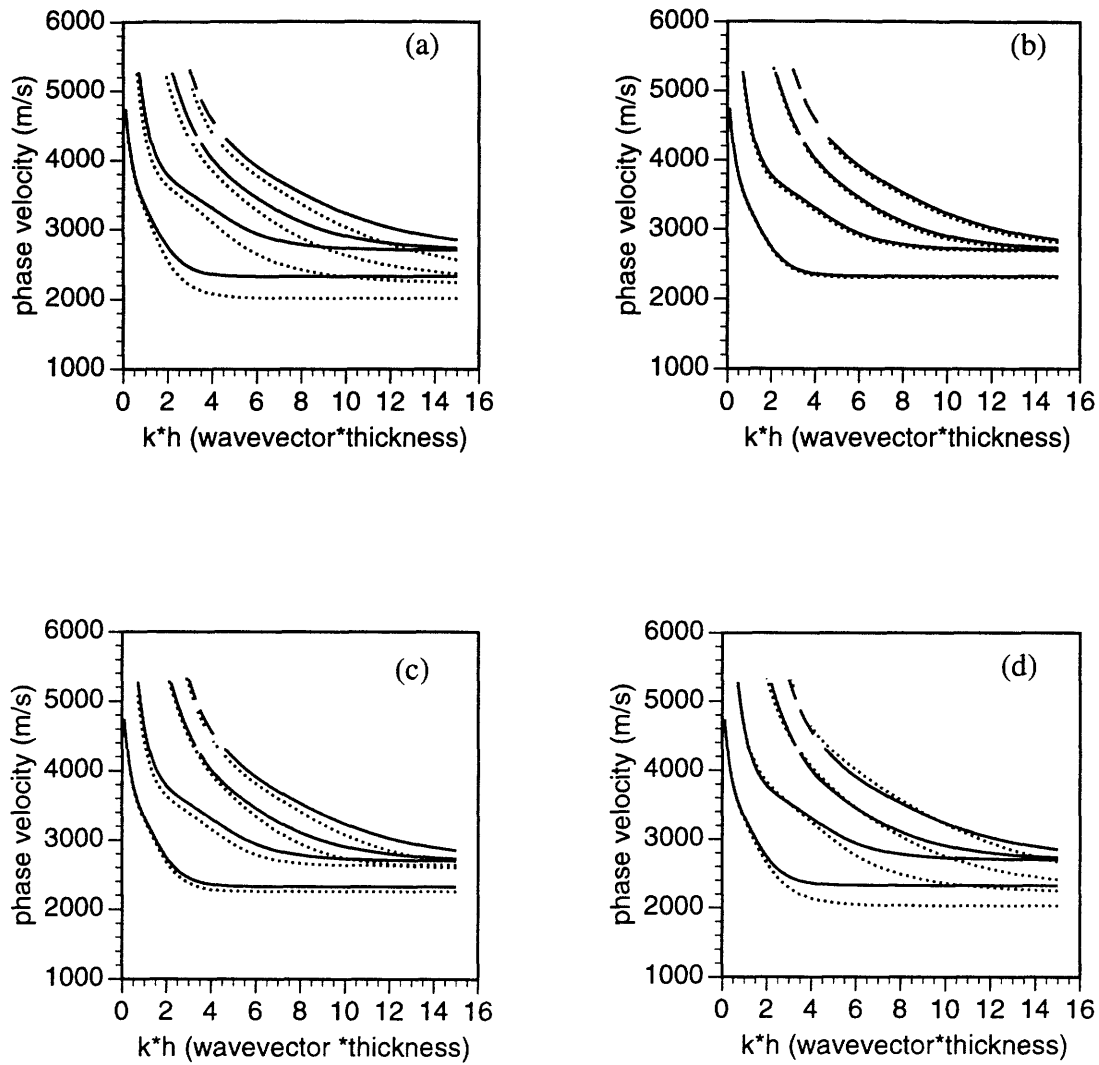


Figure 4.10 (a) Dispersion curves for a silicon supported PZT film (solid lines) compared to a nonpiezoelectric film (dashed lines) with the same elastic properties as PZT. (b) the same curves are calculated except $e_{31}=0$. (c) $e_{33}=0$ (d) $e_{15}=0$.

which it couples. e_{33} couples to motion only along the 3-axis or motion strictly out of the plane. e_{15} on the other hand couples to motion along both the 1- and 3-axes and therefore more directly affects the waveguide motions which involve both in- and out-of-plane motions.

While the above examples have been presented for the case of a PZT film upon the dielectric substrate, in many practical applications where electrical characteristics of the piezoelectric film are of interest, the film is deposited upon a metal substrate or has a very thin layer of metal in contact with the upper surface. In fact, in the PZT sample experimentally studied in this chapter, the PZT film is deposited upon layers of Pt and Ti. The effect of the metal contact is to short-circuit the surface. This can affect the phase velocities of the waveguide modes as the electrical boundary conditions at the free surface are now modified. The vertical component of the electrical displacement and the longitudinal component of the electric field at the metal-film interface are required to vanish. The dispersion curves for a short-circuited film do not differ dramatically from the dispersion curves for the open-circuited film in the case of a PZT film on silicon when an infinitesimally thin metal layer is considered. This is understood from Figure 4.5 where the electric displacements for the open-circuited film are plotted. The x_3 -component at the free surface is already quite small so that the short-circuited boundary condition forcing D_3 to zero does not strongly perturb the system.

4.5 Discussion of Experimental Results

ISTS experiments were conducted on a PZT/Pt/Ti/SiO₂/Si(substrate) multilayer system. The theoretical analysis of

this multilayer system is similar to the method presented in the preceding section and involves solving for the particle displacements and potentials in the PZT film and the particle displacements in the underlying layers and the silicon substrate. Since we are assuming that the metal layers are perfect conductors and therefore areas of constant potential, only the potential in the piezoelectric film is unknown allowing significant simplification of the problem compared to analysis of a multilayer system composed of a piezoelectric film on top of several dielectric layers.

The results of calculations of the phase velocity dispersion for lowest order mode in the PZT multilayer system and the experimental results are plotted in Figure 4.11. The elastic, piezoelectric, and permittivity constants used in the calculations are from Reference 7. (It should be noted that only the lowest order mode could be measured in this system since the higher order modes propagate with frequencies that are larger than the bandwidth of the experimental system.) The measured velocities are smaller with those predicted by using the constants for bulk PZT and the metal underlayers. Also measured was the phase velocity dispersion of the lowest order mode for only the metal underlayer system, the multilayer system composed of Pt/Ti/SiO₂/Si(substrate). The dispersion for this system is well described using the bulk values for the elastic constants of the film (where the calculated curves and experimentally measured velocities are shown in Figure 4.12). The fact that the metal only multilayer system is well described using bulk elastic parameters and the PZT-metal multilayer film exhibits velocities smaller than those predicted using the bulk parameters of PZT indicate that the elastic and piezoelectric constants of the film are different from the bulk

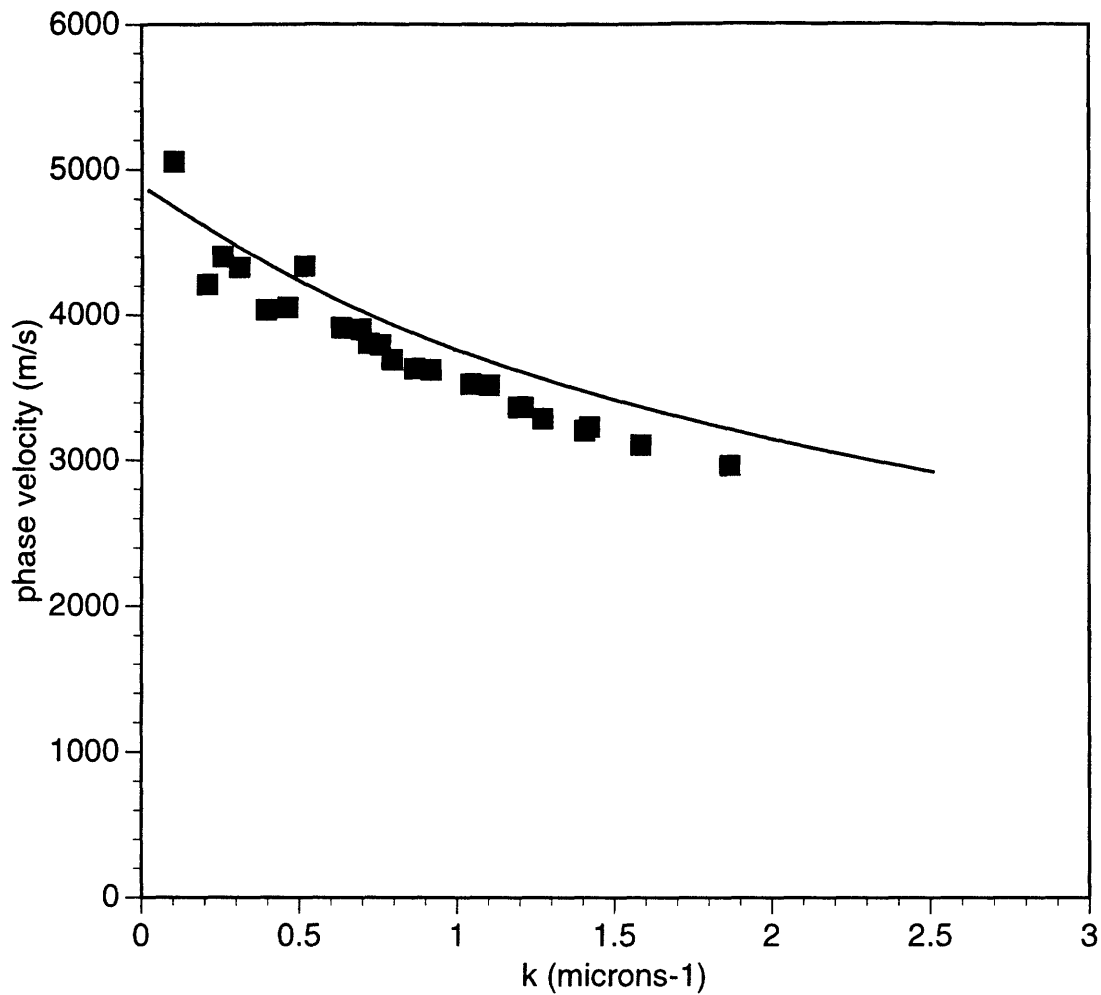


Figure 4.11. The experimentally measured (symbols) and calculated (solid lines) phase velocity dispersion in the multilayer system PZT (1200 Å)/Pt (1000 Å)/Ti(1000 Å)/SiO₂(1000 Å)/Si(substrate). The material constants used to calculate the solid lines are given in Reference 7.

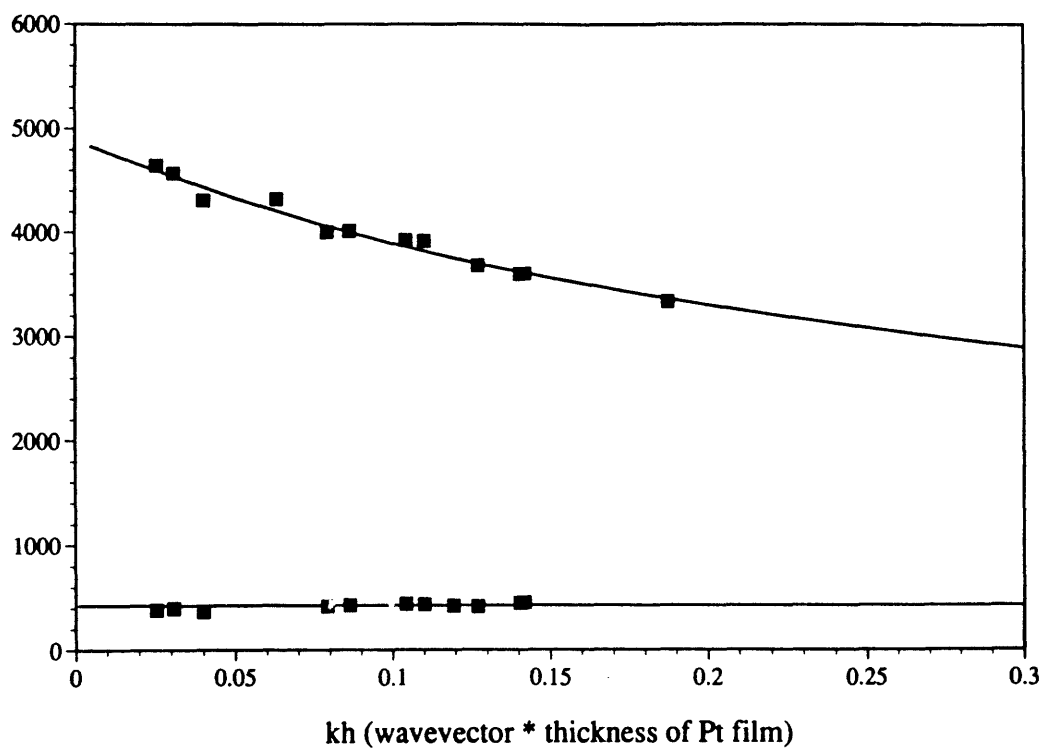


Figure 4.11. The experimentally measured (symbols) and calculated (solid lines) phase velocity dispersion in the multilayer system Pt(1000 Å)/Ti (1000 Å)/SiO₂(1000 Å)/Si(substrate). The material constants used to calculate the solid lines are given in Reference 7.

values. No attempt to fit the data was made as the large number of material parameters prohibits a unique description of the data.

It should be noted that the experimental measurement of the acoustic phase velocity behavior of piezoelectric film systems is extremely important for design considerations if these films are to be used as resonators or frequency filters. The predominant method for measuring the characteristic velocities of the piezoelectric film systems is use interdigital transducers deposited upon the film to launch and detect acoustic waves. ISTS instead allows non-contact and real-time determination of the phase velocities of the film and represents an alternative technique for launching acoustic waves in SAW devices.

4.6 Conclusion

Impulsive stimulated scattering spectroscopy is used to generate and detect pseudo-Rayleigh acoustic waves in a PZT film. This method which allows routine determination of the acoustic phase velocity dispersion in piezoelectric films is expected to be a useful tool in the characterization and evaluation of piezoelectric films for SAW devices.

References

1. (a) V.M. Bright, Y. Kim, and W.D. Hunt, *J. Appl. Phys.* **71**, 597 (1992). (b) Y. Kim and W.D. Hunt, *J. Appl. Phys.* **71**, 2136 (1992). (c) Y.K. Kim, W.D. Hunt, F.S. Hickernell, and R.J. Higgins, *Ultrasonics Symposium Proceedings*, 413 (1992).

2. Y. Shibata, K. Kaya, K. Akashi, M. Kanai, T. Kawai, and S. Kawai, *Appl. Phys. Lett.* **61**, 1000 (1992).
3. (a) Y.-X. Yan and K.A. Nelson, *J. Chem Phys.* **87**, 6240, (1989).
(b) Y.-X. Yan and K.A. Nelson, *J. Chem Phys.* **87**, 6257 (1989).
4. A.R. Duggal, J.A. Rogers, and K.A. Nelson, *J. Appl. Phys.* **72**, 2823, (1992).
5. (a) B.A. Auld, *Acoustic Fields and Waves in Solids*, (John Wiley & Sons, New York, 1973). (b) R. Dieulesaint, *Elastic Waves in Solids*, (John Wiley & Sons, Chichester, 1980).
6. G.W. Farnell and E.L. Adler, in *Physical Acoustics: Principles and Methods*, edited by W.P. Mason (Academic Press, New York and London, 1965), Chap 2, pp.35-127.
7. Londolt-Bornstein, *Low-Frequency Properties of Dielectric Crystals: Elastic Constants*, Vol. III/29a, (Springer-Verlag, Berlin, 1992).

Chapter 5. Impulsive Stimulated Raman Scattering Spectroscopy and Finite Element Modeling of Polariton Dynamics in an Anharmonic Lattice

5.1. Introduction

Phonon modes associated with structural phase transitions in ferroelectric materials have been the subject of extensive theoretical and experimental investigations¹. It is expected that the lattice potential associated with the soft-mode motion that precipitates the structural change is strongly anharmonic. Recently, Raman scattering studies on the ferroelectric crystal lead titanate have shown that in this material, the effect of the lattice anharmonicity is significant even at room temperature². In particular, the Raman scattering spectrum of the lowest frequency A_1 phonon shows a highly anomalous lineshape which is believed to originate from transitions from thermally populated excited phonon states in the anharmonic well. While the Raman scattering spectra collected at ninety degree scattering angles yield information on phonon dynamics, additional information on the shape of the potential energy surface is obtainable through study of the lattice vibrations at small wavevectors. The time-resolved method of ISRS is conveniently carried out with small scattering angles at which it is possible to excite and monitor the evolution of lattice displacements in this low wavevector regime in ferroelectric crystals.

At low wavevectors in ferroelectric materials, the interaction of polar lattice vibrations with the electromagnetic field leads to the formation of mixed phonon-electromagnetic modes known as polaritons³. This occurs when the wavevector magnitude k is on the order of ω/c where ω is

the phonon natural frequency and c is the speed of light. In this regime, the frequency and damping of the polariton are dispersive (i.e. they depend strongly on wavevector). The absolute values of the frequency and damping rate as well as the dispersion in both of these quantities yield valuable information on the potential well in which the ions move. In fact, is it possible to show that by exploiting the mixed electromagnetic-mechanical character of polaritons, it is possible to selectively probe different regions of the lattice potential energy surface.

In this chapter, we use the ISRS experimental method in conjunction with finite element simulations to investigate the dynamics of the A_1 phonon in PbTiO_3 in the polariton regime. These results are placed in context of those on the A_1 polariton in the ferroelectric crystal lithium tantalate, a material where the lattice is believed to be harmonic for vibrational levels accessible at room temperature. This work provides a baseline from which anharmonic polaritons may be studied and it motivates further ISRS investigation of PbTiO_3 .

5.2. Experimental

5.2a. Ferroelectric Crystals

The LiTaO_3 crystal, obtained from Inrad, is a 1mm thick x-cut sample, and is 5mm square. The PbTiO_3 was in the tetragonal phase and was a 2mm x 5mm x 5mm(c-axis) sample. To observe the transverse optic A_1 polariton in LiTaO_3 , the wavevector is aligned along the y axis with the polarizations of all beams along the polar axis, designated as z. In PbTiO_3 polarization of all the beams were aligned along the polar axis and the

wavevector was aligned perpendicular to the polar axis. Figure 5.1 shows the ion displacements in PbTiO_3 associated with the A_1 mode.

5.2b. Laser System and ISRS Experimental Arrangement

The laser system has been described in detail elsewhere⁴. Briefly, the system consists of a cw mode-locked Nd:YAG laser that synchronously pumps an anti-resonant ring dye laser. The output of the dye laser consists of 80 fs pulses centered at 615 nm. The pulses are subsequently amplified by a three-stage dye amplifier which is pumped by the frequency-doubled output of an optically seeded regenerative Nd:YAG laser. The final output consists of $10\mu\text{J}$ pulses at a 2 kHz repetition rate. The pulse duration remains at 80 fs, but dispersion in the sample results in actual time resolution of approximately 120 fs.

Pulses from this laser were used for exciting and probing the polaritons. To excite the polaritons⁴, two excitation beams are crossed temporally and spatially in the sample. The excitation wavevector magnitude (polariton wavelength) is determined by the crossing angle θ between the excitation beams (of wavelength λ_{laser}) through the relation $k = (4\pi\sin(\theta/2))/\lambda_{\text{laser}}$. The angles were measured by reflecting one excitation beam upon the other through the use of a mirror mounted upon a rotational stage with one minute accuracy.

We note that an important adaptation of the experimental setup for propagating modes, which is also used for examination of acoustic phonons, is cylindrical focusing of the excitation beams to form an excitation pattern which is wide (about 1.2 mm, compared to 120 μm high) in the grating wavevector direction. This is done to prevent propagation of

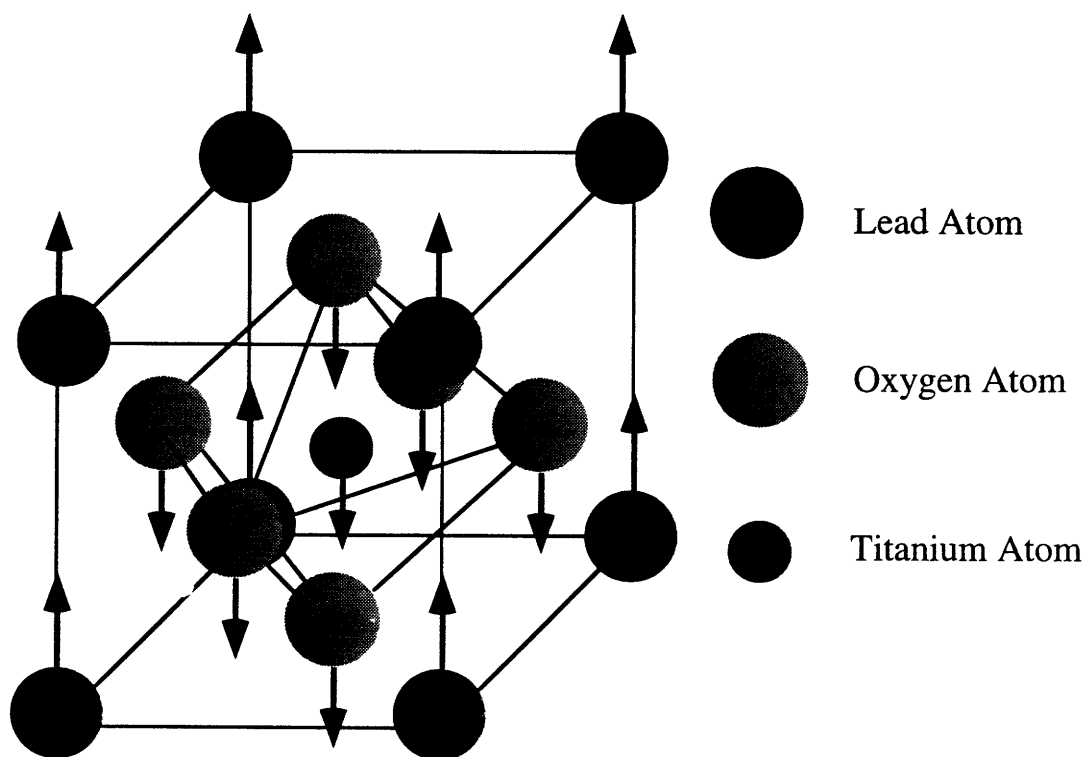


Figure 5.1. The atomic displacements associated with the lowest frequency A_1 phonon in lead titanate.

the polariton out of the excitation region before it is fully damped. For example, in the limit of small k , the group velocity, $v_g = d\omega/dk$, is $c/(\epsilon_0)^{1/2}$ which is approximately $40\mu\text{m/psec}$ for a typical low-frequency dielectric constant ϵ_0 of 50. A spot size exceeding 1 mm in the grating wavevector direction permits accurate measurement of polariton decay times up to 25 ps, which is sufficient for the A_1 polariton in LiTaO_3 and in PbTiO_3 . If the spot size is too small, propagation effects result in a non-exponential decay of the signal, making accurate determination of the damping rate difficult.

5.3. Experimental Results

ISRS data from the lowest frequency A_1 polariton at several wavevectors in LiTaO_3 and PbTiO_3 are shown in Figures 5.2 and 5.3. The ISRS response reflects the time dependent displacement of the coherently excited vibrational mode. In the case of a phonon mode in a harmonic potential, the response should be well described by an exponentially decaying sinusoid where the calculated frequency and damping are simply twice those of the excited vibrational mode⁵. Assuming a response consistent with this picture, it is possible to fit data to determine the frequency and the damping rate of the material mode. Such fits, which were obtained by a Marquadt-Levenberg least squares fitting routine, are shown along with the data in figures 5.2 and 5.3. While it is clear that this model is very consistent with the data from LiTaO_3 ^{4d,4e}, the limitations of such a model are highlighted in PbTiO_3 . While adequately describing ISRS data at very small angles, the assumption of a harmonic potential well

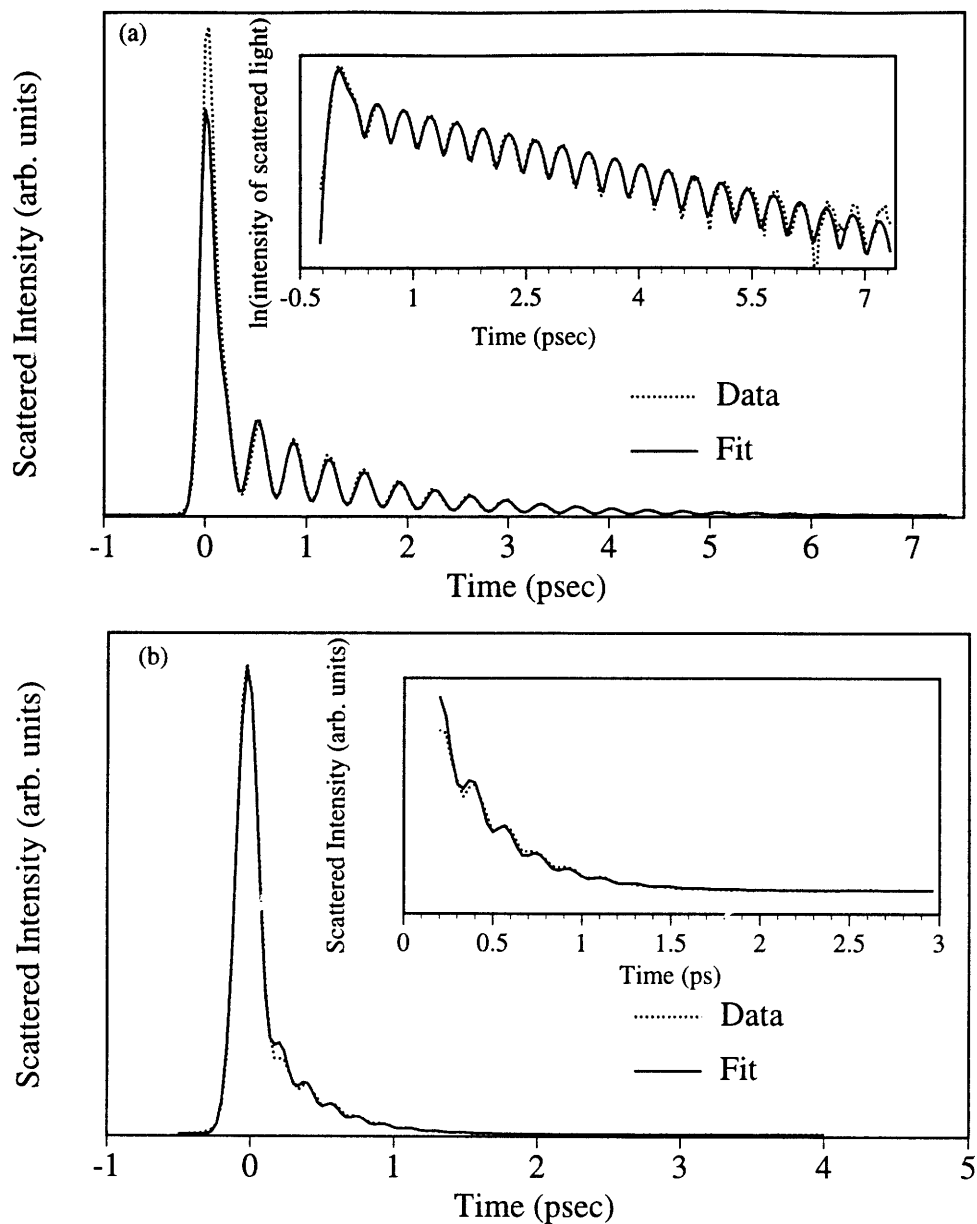
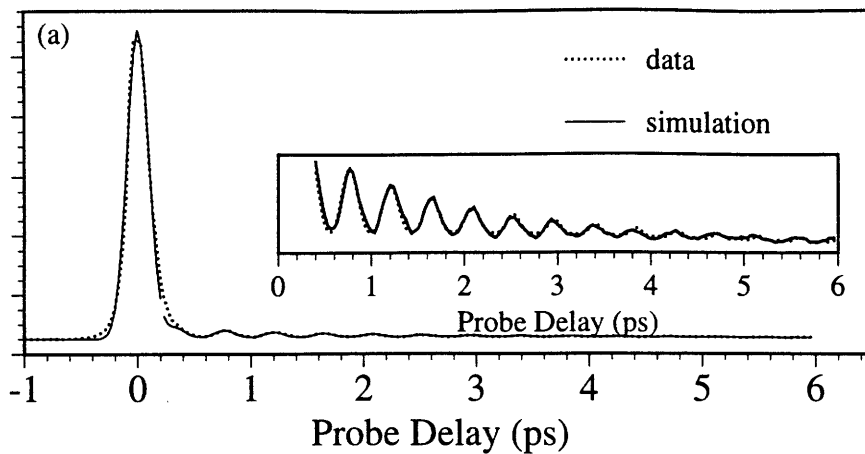
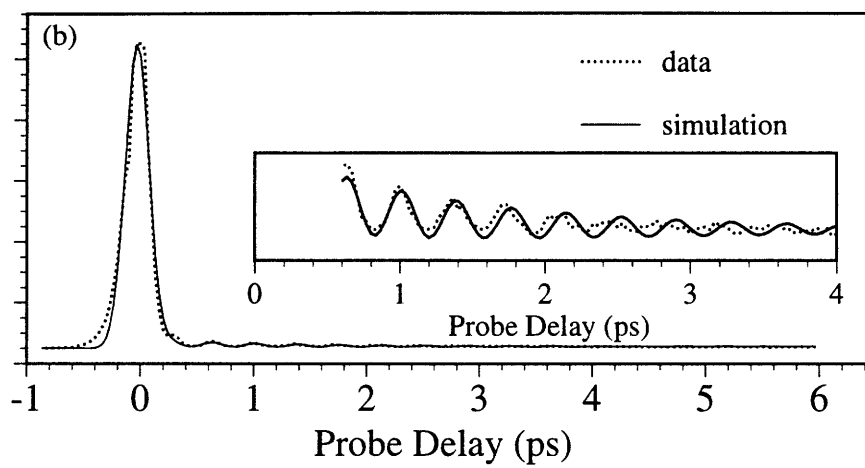


Figure 5.2. ISRS data from the lowest frequency A1 polariton in lithium titanate at (a) 1810 cm^{-1} and (b) 3980 cm^{-1} . The dashed lines represent the data while the solid lines are the best fit to a single sinusoidal oscillator model.

Scattered Intensity (arb. units)



Scattered Intensity (arb. units)



Scattered Intensity (arb. units)

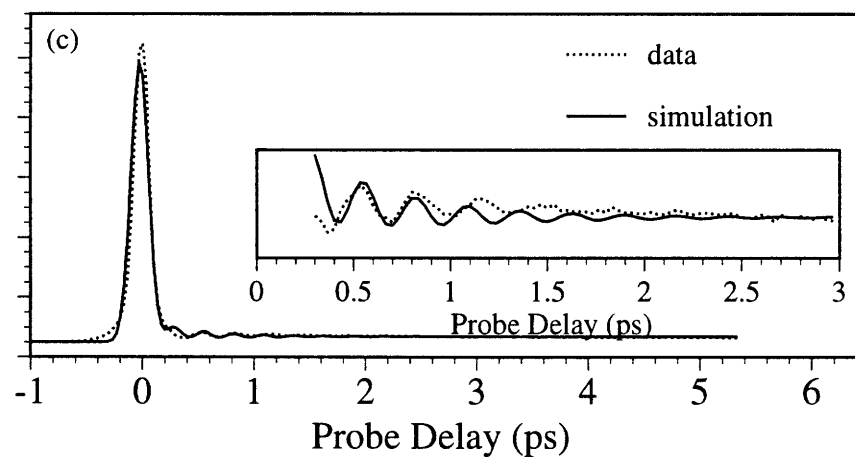


Figure 5.3. ISRS data at (a) $k=2590$ cm^{-1} , (b) 3640 cm^{-1} , and (c) 5280 cm^{-1} . The data are shown in dashed lines while the best fits to a single damped sinusoid are also shown in solid lines.

in PbTiO_3 becomes progressively worse as the wavevector magnitude grows.

As was noted in the introduction, the anharmonicity of the potential well in PbTiO_3 was recently inferred from a Raman scattering study of this material². In Figure 5.4 we show the Raman spectra of the lowest frequency A_1 phonon in PbTiO_3 in the large wavevector regime. The lineshape is well fit by a sum of four Lorentzians centered at 148.5 cm^{-1} , 137.5 cm^{-1} , 126.5 cm^{-1} , and 110.5 cm^{-1} . The positions of these Lorentzians determine the energy level spacings which in turn can be used to approximate the shape of the potential surface in PbTiO_3 . We show how this is done in appendix A.

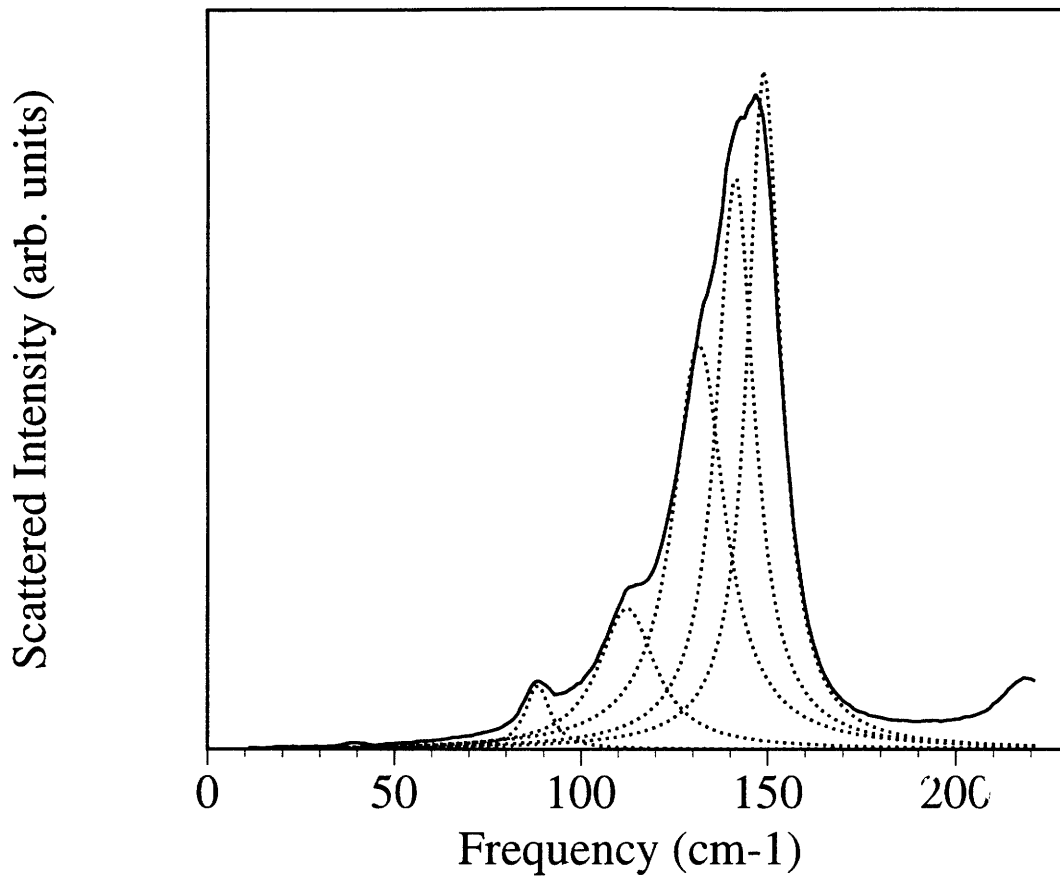
5.4. Polaritons in a Harmonic Lattice

We begin by reviewing the behavior of polaritons in a harmonic lattice³. In order to solve for all possible vibrational modes in a system composed of the lattice of an ionic crystal and the radiation field, it is necessary to consider the coupled system consisting of the equations describing polar motion in a lattice (equations 1 and 2) and Maxwell's equations (equations 3 through 6).

$$\frac{\partial^2 \mathbf{Q}}{\partial t^2} = -\omega_0^2 \mathbf{Q} + b_{12} \mathbf{E} \quad (1)$$

$$\mathbf{P} = b_{21} \mathbf{Q} + b_{22} \mathbf{E} \quad (2)$$

$$\nabla \cdot (\mathbf{E} + 4\pi \mathbf{P}) = 0 \quad (3)$$



Transitions	0 to 1	1 to 2	2 to 3	3 to 4
Experimental integrated intensities	1.00	0.98	0.63	0.48

Figure 5.4. The Raman spectra of the lowest frequency A1 phonon in lead titanate outside of the polariton regime. The dashed lines represent the deconvolution of the lineshape into the sum of four Lorentzians. (reproduced from reference 2(b))

$$\nabla \cdot \mathbf{H} = 0 \quad (4)$$

$$\nabla \times \mathbf{E} = -\frac{1}{c} \frac{\partial \mathbf{H}}{\partial t} \quad (5)$$

$$\nabla \times \mathbf{E} = -\frac{1}{c} \left(\frac{\partial \mathbf{E}}{\partial t} + 4\pi \frac{\partial \mathbf{P}}{\partial t} \right) \quad (6)$$

The above equations consider only diatomic ionic crystals that are optically isotropic. \mathbf{Q} is the mass-normalized displacement defined by $\mathbf{Q} = M^{1/2}\mathbf{R}$ where \mathbf{R} is the relative displacement between the positive and negative ions and M is the reduced mass of the system. \mathbf{P} , \mathbf{E} , and \mathbf{H} are the polarization, electric field, and magnetic field. By assuming solutions of the form

$$\mathbf{Q} = \mathbf{Q}_0 e^{i(\mathbf{k} \cdot \mathbf{x} - \omega t)} \quad (7)$$

$$\mathbf{P} = \mathbf{P}_0 e^{i(\mathbf{k} \cdot \mathbf{x} - \omega t)} \quad (8)$$

$$\mathbf{E} = \mathbf{E}_0 e^{i(\mathbf{k} \cdot \mathbf{x} - \omega t)} \quad (9)$$

$$\mathbf{H} = \mathbf{H}_0 e^{i(\mathbf{k} \cdot \mathbf{x} - \omega t)} \quad (10)$$

equations 1 through 6 can be solved. When there is no interaction between the lattice and the radiation field ($b_{22}=0$), the solutions reduce to two (transverse) electromagnetic modes and three lattice modes two of which are transverse and one of which is longitudinal. When there is interaction between the lattice and the radiation field, there are still a total of five solutions to the coupled system of equations which fall into two categories. The first category requires that the magnetic field associated with the vibrational mode disappear. As a result, modes which fall into this

category does not couple to the radiation field, just and represents longitudinal vibrations of the lattice. Because it turns out that in most ferroelectric materials, the longitudinal vibrations of the lattice occur on timescales significantly shorter than the excitation pulse duration, we do not discuss these modes further. The second category of solutions represent transverse modes in which the displacement \mathbf{Q} , the polarization \mathbf{P} , and electric field \mathbf{E} are parallel to one another and are perpendicular to the wavevector \mathbf{k} which in turn is perpendicular to \mathbf{H} .

To gain further understanding on these transverse modes, we make use of the known directions of the vectors to rewrite equations 1 through 6 in scalar form,

$$\frac{\partial^2 Q(x, t)}{\partial t^2} = -\omega_0^2 Q(x, t) + b_{12} E(x, t) \quad (11)$$

$$\nabla^2 E(x, t) = \frac{1}{c^2} \left(\frac{\partial^2}{\partial t^2} (E(x, t) + 4\pi P(x, t)) \right) \quad (12)$$

$$P(x, t) = b_{21} Q(x, t) + b_{22} E(x, t) \quad (13)$$

If the assumed forms for E , Q , and P given in equations (7) through (10) are substituted into the above equations, the dispersion relation for the frequency can be derived. The result is,

$$\left(\frac{ck}{\omega} \right)^2 = 1 + 4\pi b_{22} + \frac{4\pi b_{12} b_{21}}{-\omega_0^2 - \omega^2} \quad (14)$$

For each wavevector there exist two independent frequencies. For each wavevector there also exist two independent choices for the electric field yielding two doubly degenerate solutions for each choice of wavevector. By comparing the dispersion relation given in equation (14) with the phenomenological relation for the dielectric constant given in equation (15), the following values (equations (16) and (17)) of the coupling constants in terms of material constants can be calculated.

$$\varepsilon = \varepsilon_{\infty} + \frac{(\varepsilon_0 - \varepsilon_{\infty})\omega_0^2}{\omega_0^2 - \omega^2} \quad (15)$$

The coupling constants are

$$b_{12} = b_{21} = \left(\frac{\varepsilon_0 - \varepsilon_{\infty}}{4\pi} \right)^{1/2} \omega_0 \quad (16)$$

$$b_{22} = \frac{\varepsilon_{\infty} - 1}{4\pi} \quad (17)$$

In figure 5.5(a) we display the calculated frequency dispersion curves for the lowest frequency A1 polaritons in lithium tantalate and lead titanate. In the low wavevector regime, the frequency of the lower branch mode approaches $ck/\varepsilon(0)$ the frequency of light traveling at very low frequencies. In this wavevector regime, the polariton is dominated by the electromagnetic field.. In this same wavevector region, the frequency of the higher branch mode approaches that of the longitudinal optic phonon mode and is dominated by lattice motion. In contrast to this, in the large wavevector regime, the frequency of the higher branch approaches $ck/\varepsilon(\infty)$, the frequency of light traveling at infinite frequency, while the

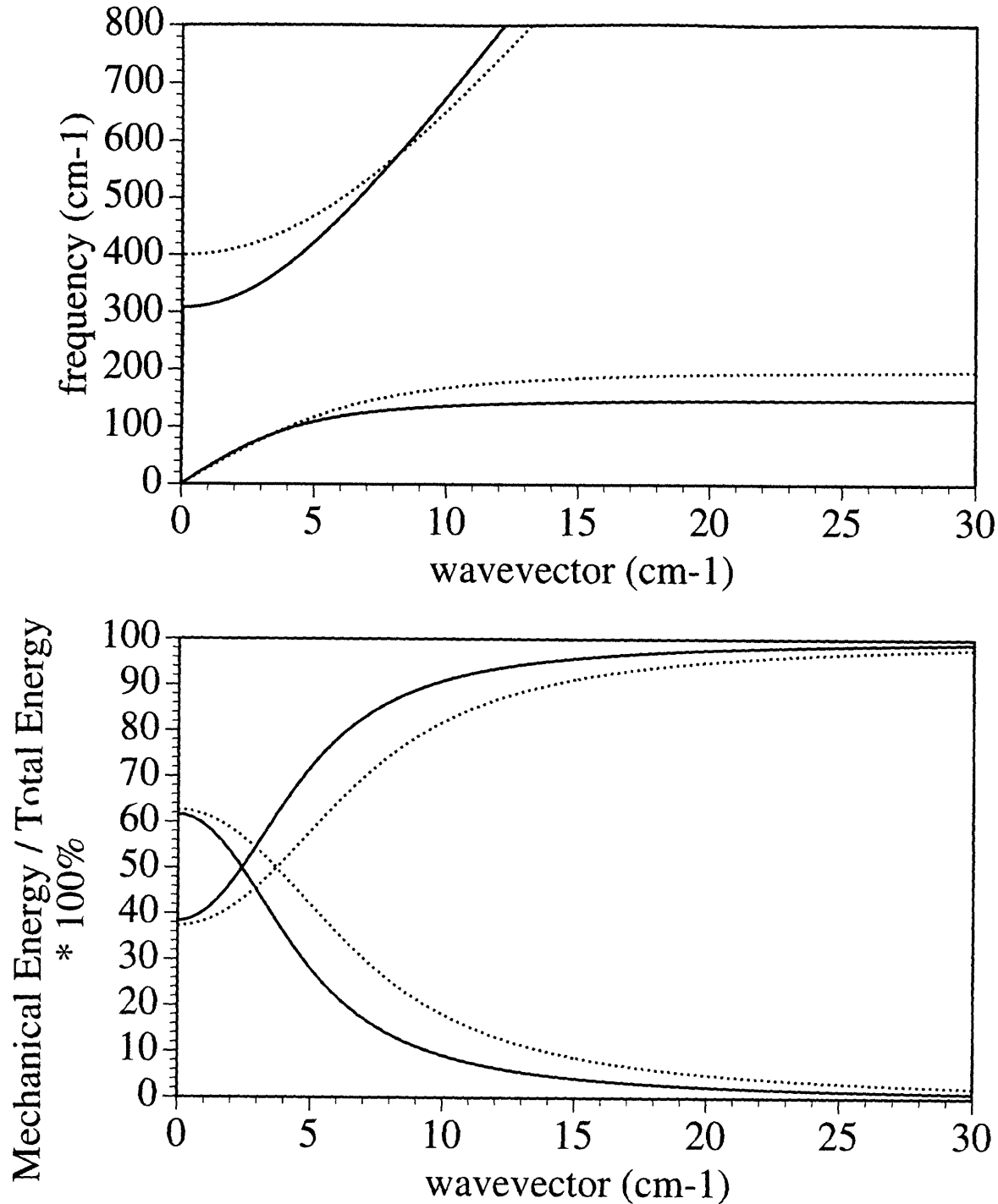


Figure 5.5. The wavevector dependence of the (a) frequency and the (b) mechanical energy of the two allowed transverse modes in the polariton regime. The dashed lines represent calculations using the material constants of lithium tantalate and the solid lines represent calculations using the material constants of lead titanate (assuming a harmonic lattice). The material parameters used were for lithium tantalate, $\omega_0=201\text{cm}^{-1}$, $\epsilon_0=34.0$, $\epsilon_{\text{inf}}=8.6$ and for lead titanate $\omega_0=148.5\text{cm}^{-1}$, $\epsilon_0=28.6$, $\epsilon_{\text{inf}}=6.64$.

frequency of the lower branch mode approaches that of the transverse uncoupled lattice mode. This description of polariton dispersion accounts very accurately for what is experimentally observed in many materials. As an illustration, the calculated and measured frequency dispersion for LiTaO₃ is shown in Figure 5.6.

While the mixed electromagnetic-mechanical character of a polariton is inferred from frequency dispersion like that shown in figure 5.5(a), a more quantitative understanding can be obtained by computing the energy of the mode^{3a}. The energy density of the polariton (given in equation (19)) is determined from equation (18) which is the general expression of the energy density determined from Maxwell's equations.

$$U = \frac{c}{4\pi} \int_{\text{surface}} (\mathbf{E} \times \mathbf{H}) \cdot d\boldsymbol{\sigma} = - \int_{\text{volume}} \left\{ \frac{1}{4\pi} \left(\mathbf{E} \cdot \frac{\partial \mathbf{E}}{\partial t} + \mathbf{H} \cdot \frac{\partial \mathbf{H}}{\partial t} \right) + \mathbf{E} \cdot \frac{\partial \mathbf{P}}{\partial t} \right\} d\tau \quad (18)$$

$$U = \frac{1}{2} \left(\frac{\partial \mathbf{Q}}{\partial t^2} + \omega_0^2 \mathbf{Q}^2 \right) + \frac{1}{8\pi} (\epsilon_\infty \mathbf{E}^2 + \mathbf{H}^2) \quad (19)$$

The lattice energy appears in the first parentheses and the radiative energy appears in the second parentheses. With this expression, the fraction of the total energy that is due to mechanical energy can be easily found from the solutions determined from equations (7) through (10) and is

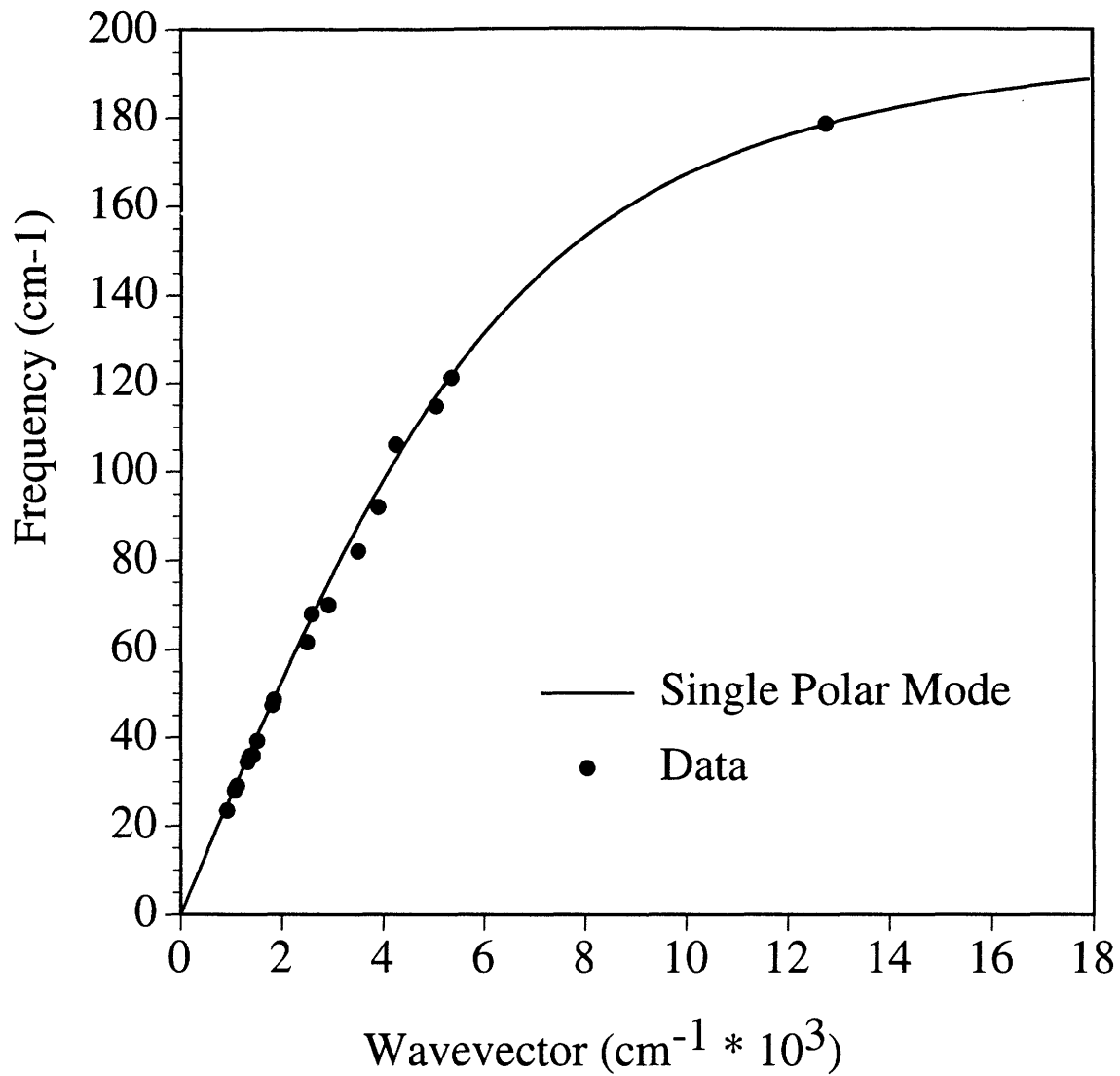


Figure 5.6. The experimentally determined frequency dispersion for the A_1 polariton in lithium tantalate and the calculated dispersion. The dispersion was calculated using the parameters of the previous figure.

$$\frac{U_{\text{mech}}}{U_{\text{total}}} = \frac{\left[(\epsilon_0 - \epsilon_\infty) \left(1 + \frac{\omega^2}{\omega_0^2} \right) \right] \left(1 - \frac{\omega^2}{\omega_0^2} \right)^{-2}}{\epsilon_\infty + \left(\frac{ck}{\omega} \right)^2 + \left[(\epsilon_0 - \epsilon_\infty) \left(1 + \frac{\omega^2}{\omega_0^2} \right) \right] \left(1 - \frac{\omega^2}{\omega_0^2} \right)^{-2}} \quad (20)$$

where the time-dependent quantities in equation (19) have been averaged over a period of a vibration. In Figure 5.5(b) the lattice energy fractions for the upper and lower branches of the polariton mode in lead titanate and lithium tantalate are shown. Figure 5.5 illustrates how the lower frequency polariton changes from largely electromagnetic in character at low wavevectors to almost purely mechanical at large wavevectors while the higher frequency polariton exhibits the opposite behavior.

5.5. Polariton Dynamics in an Anharmonic Potential

As we have argued in previous sections, the potential well in which ions move in PbTiO_3 is strongly anharmonic. As a result, a more general treatment of polariton dynamics than that given in the previous section is needed to understand the results of experiments in this material. In order to treat a polariton in an arbitrary lattice potential, we return to equations (11) through (13), rewriting the equation of motion for the displacement to account for the presence of an anharmonic potential.

$$\frac{\partial^2 Q(x, t)}{\partial t^2} = \frac{-dV(x)}{dx} + \Gamma \frac{\partial Q(x, t)}{\partial t} + b_{12} E(x, t) + F(x, t) \quad (21)$$

$$\frac{\partial^2 E(x,t)}{\partial x^2} = \frac{(1 + 4\pi b_{22})}{c^2} \frac{\partial^2 E(x,t)}{\partial t^2} + \frac{4\pi b_{21}}{c^2} \frac{\partial^2 Q(x,t)}{\partial t} \quad (22)$$

$V(x)$ represents the potential well (which is arbitrary at this stage), Γ is a phenomenological damping term, and $F(x,t)$ is a forcing function included to account for ISRS excitation of the polaritons. Since the ISRS response is related to $Q(x,t)$, a solution for the displacement as a function of time is required to simulate the ISRS response in PbTiO_3 . Because we wish to keep the potential $V(x)$ as general as possible, and since there are only a very small set of anharmonic potentials for which it is possible to obtain an analytic solution, we utilize the numerical method of finite differencing to solve the coupled system of nonlinear differential equations⁶. The equations are solved on a time and space grid with the following evolution equations for the displacement and the electric field.

$$Q_j^{n+1} = (\Delta t)^2 \left[W_j^n + b_{12} E_j^n + F_j^n \right] - (\Delta t) \Gamma \left[Q_j^{n+1} - Q_j^n \right] + 2Q_j^n - Q_j^{n-1} \quad (23)$$

$$E_j^{n+1} = \left(\frac{\Delta t}{\Delta x} \right)^2 \left(\frac{c^2}{1 + 4\pi b_{22}} \right) \left(E_{j+1}^n - 2E_j^n + E_{j-1}^n \right) + 2E_j^n - E_j^{n-1} + \left(\frac{4\pi b_{21}}{1 + 4\pi b_{22}} \right) \left(-Q_j^{n+1} + 2Q_j^n - Q_j^{n-1} \right) \quad (24)$$

n defines the time grid while j defines the space grid. W_j^n represents the force due to the lattice potential ($-dV(x)/dx$). In all calculations, the coupling constants b_{12} , b_{21} , and b_{22} are assumed to be equal to the values

derived in the harmonic case. The natural frequency ω_0 used to compute b_{12} , b_{21} , b_{22} is assumed to be the frequency associated with the harmonic approximation to the anharmonic potential $V(x)$. The numerical methods used for solving these equations were verified through solutions of the harmonic case where analytic solutions exist. In Figure 5.7 we show the numerically and analytically determined frequency dispersion for lithium tantalate. As is evident, agreement is excellent.

Only a few general features of the numerical method will be discussed before proceeding to the specific example of the anharmonic lattice of lead titanate. An obvious point is that unlike in the harmonic case where the polariton dynamics are independent of the initial conditions or intensity of the excitation force, here the dynamics depend sensitively upon the region of the potential energy surface that is sampled. As a result, care must be taken when dealing with the thermal energy distribution and the intensity of the excitation pulses. In order to simply account for finite temperatures, the simulations were performed with the initial conditions of zero displacement and electric field and with the intensity of the excitation force determined such that the energy imparted by the excitation pulse was equal to the thermal energy available to the mode. While having some deficiencies, we believe this to be a consistent way to incorporate the effects of finite temperature. This method assumes that the energy imparted by the excitation force in an actual ISRS experiment is negligible compared to the thermal energy in the lattice. Appendix B outlines experimental approaches and numerical simulations utilizing multiple pulse sequences to induce large amplitude phonon motion.

An interesting feature common to polaritons which becomes obvious using this method to treat finite temperatures in an anharmonic lattice is

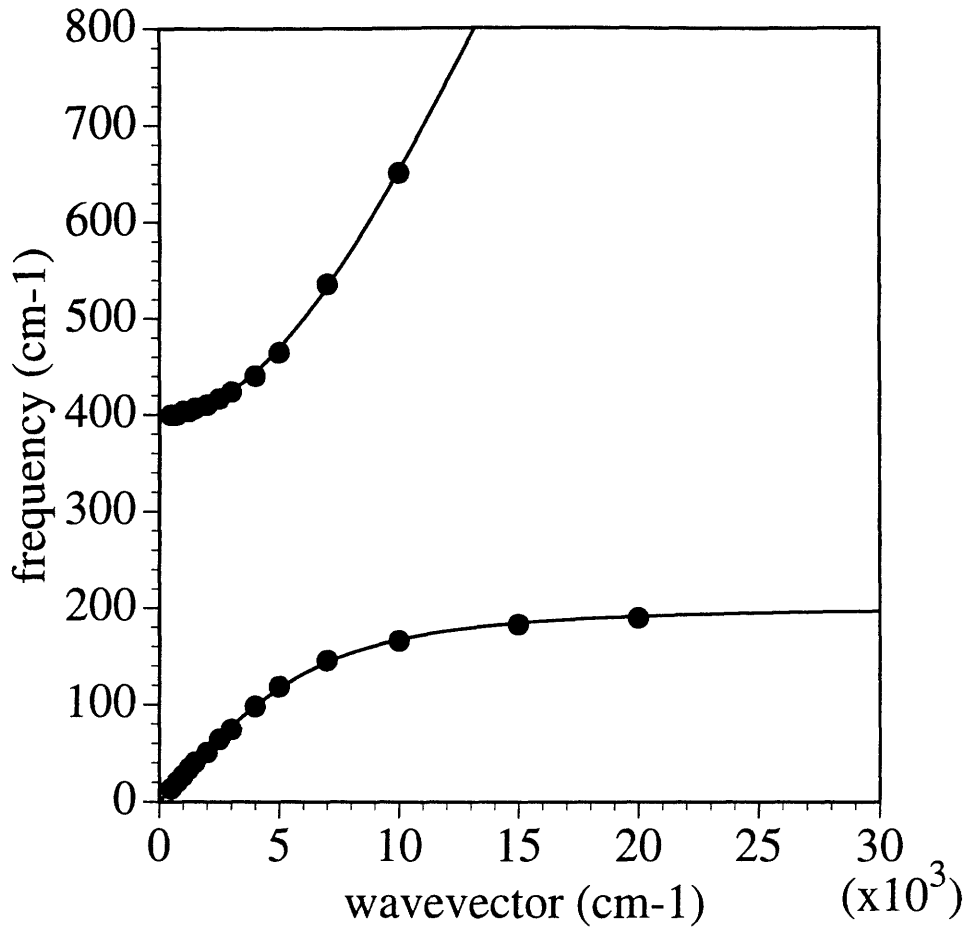


Figure 5.7. Verification of the numerical method in the harmonic limit. The symbols represent the frequencies calculated using the numerical method described to model the polariton dynamics in lithium tantalate. The solid lines represent that analytic solution to the coupled mechanical-electromagnetic equations.

that because the ratio of mechanical energy to total energy increases with increasing wavevector, it is possible to adjust the region of the potential energy surface which is probed by changing the excitation wavevector at a given temperature. In other words, at a fixed temperature, the amplitude of the displacement due to thermal energy decreases with the wavevector. This property of polaritons might be exploited to selectively probe different regions of the potential surface through ISS excitation wavevector adjustment. We also note that a similar effect might be achieved by changing the temperature.

Finally, we note that for all simulations, the pulsewidth of the excitation force was chosen to match the pulsewidth used in the ISRS experiments. Because of this, only the lower frequency polariton is excited. This simplifies the analysis since in the anharmonic case it would be difficult to separate the dynamics of the two polaritons.

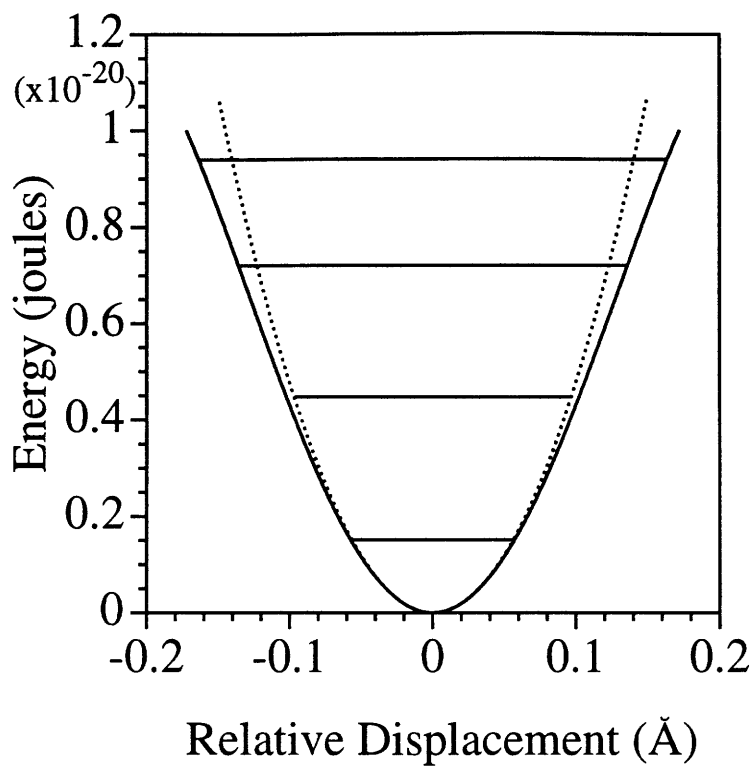
5.6. Numerical Simulations of the Polariton Dynamics in Lead Titanate.

In order to model the ISRS results in lead titanate, the form of the anharmonic potential must be determined. The energy spacings determined from the frequency domain Raman spectra were used to model the potential. The potential is assumed to have only quadratic and quartic terms taking the form

$$V(x) = \alpha x^2 + \beta x^4 \quad (25)$$

The values of α and β were determined by fitting the observed energy spacings shown in Figure 5.8 using the method of McWeeny and Coulson⁷. The details of the method are given in Appendix A. The parameters that yielded the best fit are given in Figure 5.8 along with graphs of the anharmonic potential and the harmonic potential obtained by ignoring the quartic term.

Simulations of ISRS data in lead titanate at room temperature at 2500 cm^{-1} and 5000 cm^{-1} are shown in Figure 5.9 along with attempted fits to single sinusoidal oscillator models. What is shown is the square of the time-dependent displacement induced by the excitation pulses. As seen in the experimental data, while the single oscillator model provides an adequate description of the data at 2500 cm^{-1} , it fails to describe the data at 5000 cm^{-1} . This is consistent with arguments given in previous sections. That is, as the wavevector increases, the fraction of the polariton's total energy that is due to mechanical energy increases. Therefore as the wavevector increases, the initial displacement due to thermal energy increases as seen in Figure 5.5(b). Because a greater fraction of the thermal energy is available for mechanical energy at higher wavevector, the oscillator samples the more anharmonic regions of the potential energy surface at higher wavevectors. The ISRS response at low wavevectors can be fit by a single sinusoidal oscillator model since in that case, the oscillator probes the nearly harmonic region of the potential energy surface. At higher wavevectors, however, this description fails as the oscillator response reflects the anharmonicity of the lattice. It should be noted that although no quantitative inversion of the experimental ISRS data to the form of the lattice potential was attempted, an anharmonic lattice potential at least qualitatively explains the wavevector-dependent response observed.



————— $V(R) = \frac{1}{2} m \omega^2 R^2 + m^2 \alpha R^4$

..... $V(R) = \frac{1}{2} m \omega^2 R^2$

$$m = 1.088 \times 10^{-25} \text{ kg}$$

$$\omega = 2.957 \times 10^{13} \text{ s}^{-1}$$

$$\alpha = -3.955 \times 10^{72} \text{ kg}^{-1} \text{ m}^{-2} \text{ s}^{-2}$$

Figure 5.8. The anharmonic potential used in the numerical simulations of the polariton dynamics in lead titanate.

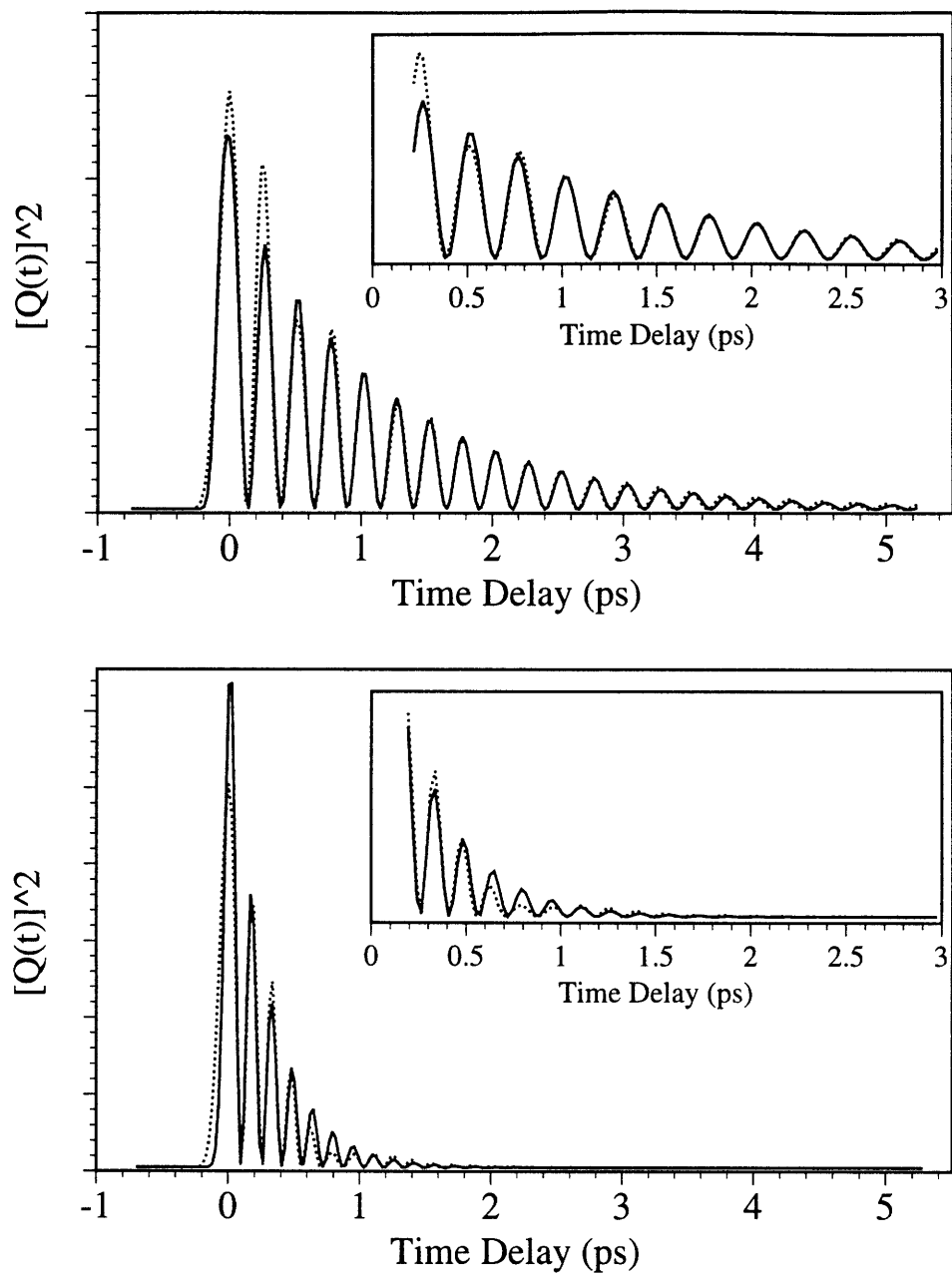


Figure 5.9. Simulations (dashed lines) of the square of the displacements in lead titanate calculated using the numerical method at $k=2500 \text{ cm}^{-1}$ and $k=5000 \text{ cm}^{-1}$. The solid lines represent the best fit to the simulations using a single sinusoidal oscillator model.

5.7. Conclusion

ISRS results on the lowest frequency A1 polariton in lead titanate and numerical simulations demonstrate the effect of anharmonic lattice potentials on polariton dynamics. The effect is negligible at low wavevectors as the polariton samples only the harmonic region of the potential energy surface and grows at higher wavevectors where the polariton displacement extends into the anharmonic region of the lattice potential. The experimental and numerical results suggest that the mixed electromagnetic-mechanical character of polaritons may be used to selectively probe different regions of lattice potential energy surfaces.

References

1. M.E. Lines and A.M. Glass, Principles and Applications of Ferroelectrics and Related Materials, (Alarendom, Oxford, 1977).
2. (a) C.M. Foster, M. Grimsditch, Z. Li, and V.G. Karpov, Phys. Rev. Lett. **71**, 1258 (1993). (b) C.M. Foster, Z. Li, M. Grimsditch, S.-K. Chan, and D.J. Lam, Phys. Rev. B **48**, 10160 (1993).

3. (a) K. Huang, Proc. of Roy. Soc. Ser. A **208**, 352 (1951). (b) M. Born and K. Huang, Dynamical Theory of Crystal Lattices (Clarendon, Oxford, 1962). (c) A.S. Barker and R. Loudon, Rev. Mod. Phys. **44**, 18 (1972)
4. (a) T.P. Dougherty, G.P. Wiederrecht, and K.A. Nelson, Ferroelectrics **120**, 79 (1991). (b) T.P. Dougherty, G.P. Wiederrecht, and K.A. Nelson, Science **258**, 770 (1992) (c) T.P. Dougherty, G.P. Wiederrecht, and K.A. Nelson, submitted to Phys. Rev. B. (d) G.P. Wiederrecht, T.P. Dougherty, L. Dhar, and K.A. Nelson, Ferroelectrics (e) G.P. Wiederrecht, T.P. Dougherty, L. Dhar, and K.A. Nelson, submitted to Phys. Rev. B.
5. (a) Y. -X. Yan and K.A. Nelson, J. Chem. Phys. **87**, 6240 (1987). (b) Y. -X. Yan and K.A. Nelson, J. Chem. Phys. **87**, 6257 (1987).
6. W.H. Press, S.A. Teukolsky, W.T. Vetterling, and B.P. Flannery, Numerical Recipes in C (Cambridge University Press, New York) 1992.
7. R. McWeeny and C.A. Coulson 1947.

Chapter 6. Single-Shot Ultrafast Absorption Spectroscopy

6.1 Introduction

This chapter presents the experimental groundwork for the spectroscopic study of the dynamics of permanent chemical or structural change. The early time dynamics of photoinitiated irreversible chemical or structural transformations in condensed media other than liquids are not easily probed using traditional time-resolved spectroscopic techniques. Typically, the time-dependent absorption of an evolving species is measured through a series of pump-probe sequences. A "pump" laser beam first initiates the reaction and then the system response is measured by a time-delayed probe pulse. The entire time response is mapped out through many pump-probe repetitions with the probe pulse arriving at incrementally longer delays requiring a sample to be exposed to multiple laser shots. This approach cannot be easily used to probe irreversible phenomena in the many media which cannot be conveniently flowed or translated and in which a buildup of reaction product in the irradiated volume interferes with conventional pump-probe experiments. What is required is a technique that allows the time response to be measured in a single laser shot. This yields a multiplex advantage for signal-to-noise ratios in cases where the experiment can be repeated and the signal can be averaged, and most importantly allows for the direct observation of irreversible

processes as they occur. In this chapter, an optical technique for performing single-shot pump-probe spectroscopy with femtosecond time resolution is demonstrated.

6.2 Experimental

Measurement of the time-dependent response of a photoexcited sample in a single laser shot is accomplished through spatial encoding of the temporal information. Although spatial techniques have been used in the past, most have suffered from limited time resolution¹. The approach taken here is similar to that utilized in single-shot autocorrelation experiments². The pump and probe beams are cylindrically focused and overlapped at a wide angle within the sample of interest. The time delay is therefore encoded along the long axis of the cylindrically focused probe beam as its time of interaction with the excited sample varies along this axis. The probe beam is then imaged through a series of lenses onto a CCD camera allowing the temporal information encoded along the cylindrical axis to be recorded.

The experimental geometry is illustrated in Figures 6.1 and 6.2. A 10 cm focal length cylindrical lens is used to focus the pump and probe beams upon the sample. The angle between the pump and probe beams is 15° . The pump and probe beams are spatially overlapped within the sample and then collimated by another 10 cm focal length cylindrical lens placed on the opposite side of the sample. A 20 cm focal length cylindrical lens placed after the collimating lens is used to correct for any diffractive effects and

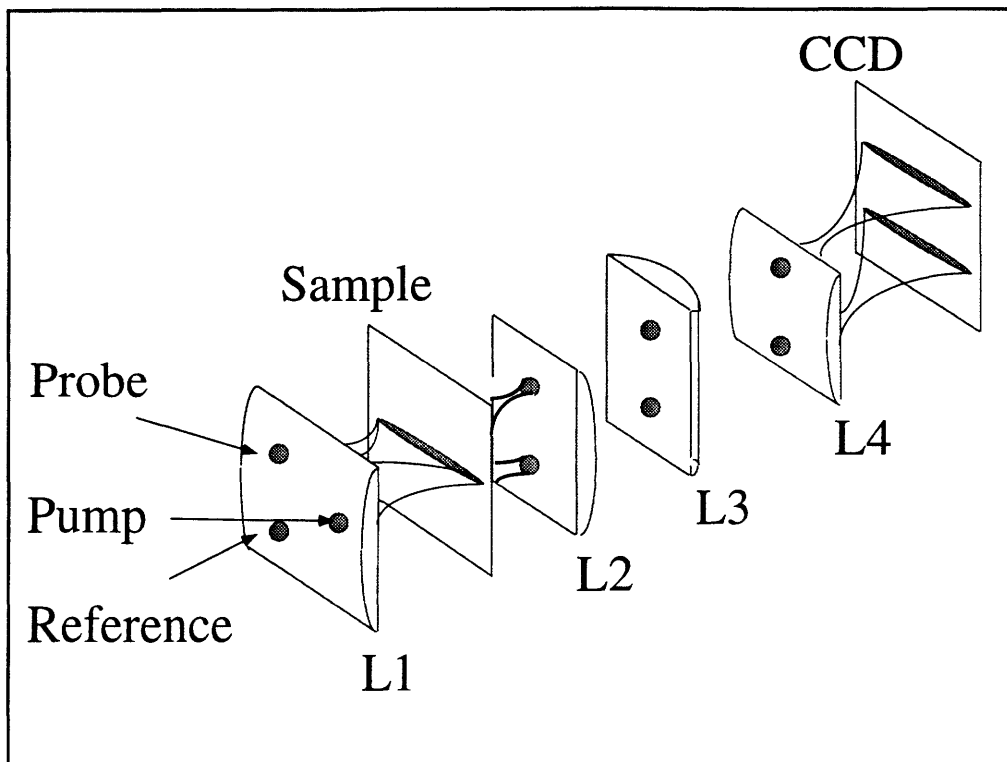


Figure 6.1. The geometry used for the single-shot pump-probe experiment. The pump beam and the probe and reference beams are set to cross at a 15° angle and the three are cylindrically focussed onto the sample. The cylindrically focussed probe and reference beams are then imaged through a series of lenses onto the CCD. Cylindrical lenses L1, L2, L3, and L4 are of focal lengths 10 cm, 10 cm, 20 cm, and 15 cm respectively. L1 and L2 are used to focus and collimate the beams. L3 is used to image the beam and L4 is used focus the images onto the CCD.

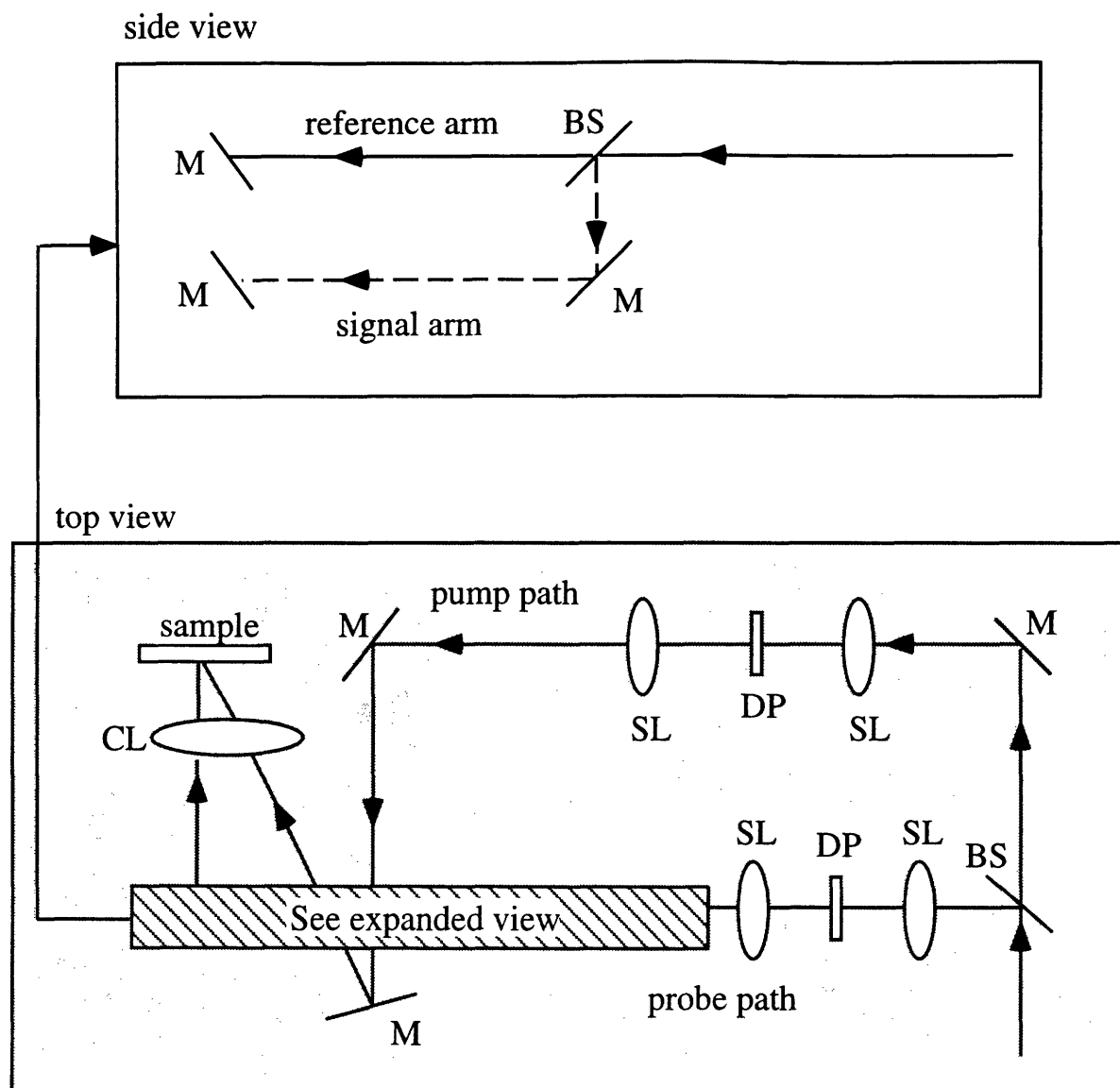


Figure 6.2. The experimental layout for the single-shot pump-probe method. The expanded view illustrates the splitting of the probe beam into a signal arm and a reference arm. The optical components are labelled as: M - mirror, BS - beam splitter, DP - diamond pinhole, SL - spherical lens, CL - cylindrical lens.

image the probe beam profile at the sample upon a 512x512 pixel CCD (Princeton Instruments). A 15 cm focal length cylindrical lens is then used to focus the probe beam onto the CCD. The distances of the lenses from the sample are shown in Figure 6.1. In order to optimize the distance of the imaging lens (L3) from the CCD, a reticule was placed at the sample position and the lens position was adjusted until the probe image on the CCD yielded a clear image of the patterned lines of the reticule. It was found that the time resolution of the experiment was very sensitive to the angular position of the cylindrical lenses. The angular adjustments are shown schematically in Figure 6.3. The angle of each lens about the y-axis was adjusted so that each of the beams was reflected back along its path of incidence. The angle about the x-axis of the imaging lens (L3) was adjusted so that the line pattern seen on the CCD from imaging the reticule was perpendicular to the vertical edges of the square sensitive area of the CCD. The CCD was aligned with a leveler. The angles about the x-axis of the focusing and collimating lenses (L1 and L2) were adjusted so that the cylindrical axes of the beams were respectively parallel and perpendicular to the laser table.

In order to extract the time-dependent response of the sample, the probe image must be normalized for the probe intensity profile and the pump intensity profile. To normalize for the probe intensity profile, a reference beam is split off from the probe arm and overlapped with the pump and probe beams within the sample as shown in Figures 6.1 and 6.2. The heights of the probe and reference beams are set so that they are vertically equidistant from

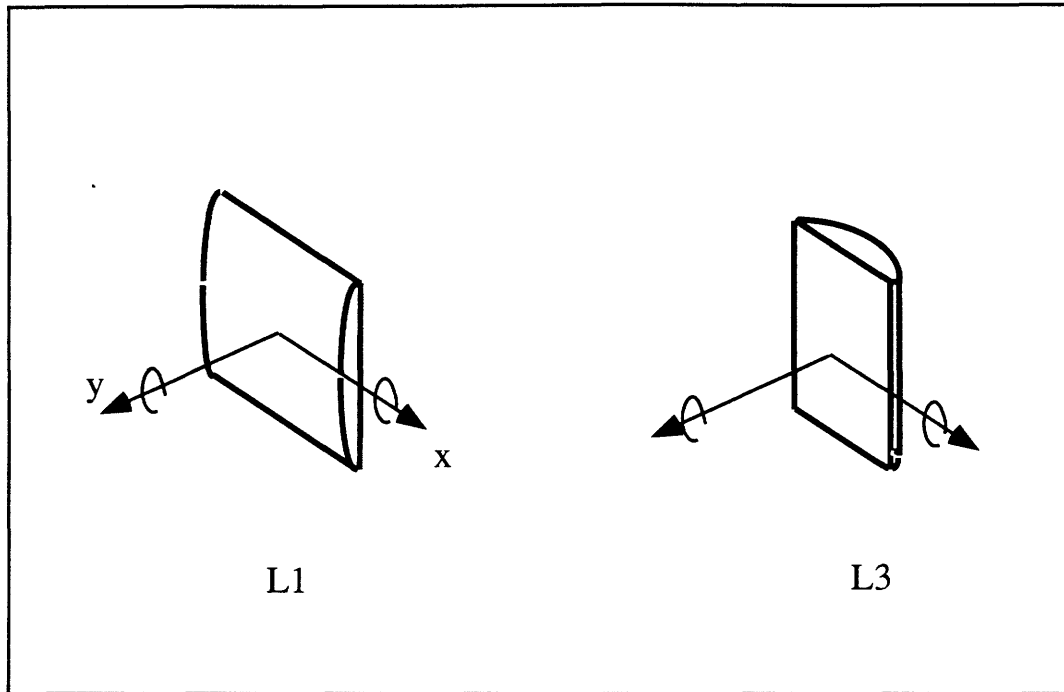


Figure 6.3. The angular adjustments for the cylindrical lenses. Rotational adjustments about the y-axis are made on L1 and L2 (not shown here) so that the back reflection of the probe and reference beams are coincident with the incoming beams. The rotational adjustment about y-axis on these two lenses are made so that the cylindrical axis of each of the beams is parallel to the table for L1 and perpendicular to the table for L2. The x-axis rotational adjustment on L3 is again made by monitoring the back reflection of the beams while the y-axis rotational adjustment is made by monitoring the image of the probe beam passing through a reticule placed at the sample position. The angle is set so that the line pattern of the reticule appears parallel to the vertical edges of the square sensitive area of the CCD.

the pump beam. The reference beam, which is timed to arrive at the sample before the pump pulse, is imaged onto the CCD through the same set of lenses used for the probe beam. The normalization of the probe profile is performed within the CCD data acquisition software³ and is described below. These intensity profiles are then subtracted on a shot-to-shot basis. This normalization procedure is crucial to the experiment because it allows for shot-to-shot variations in the probe intensity profile to be accounted for as the probe profile is compared to a reference profile derived from the same laser shot. A previous normalization strategy which attempted to discriminate against bad laser shots using a position sensitive photodiode to monitor a fraction of the probe beam and then normalized the probe profile with an acceptable subsequent pulse was found to be difficult to implement and extremely unreliable. The present approach of using a reference beam derived from the same laser shot yields reproducible intensity profiles and higher data acquisition times as nearly every laser shot can be utilized.

To normalize for the pump intensity profile, a sample with a long lifetime is used to record the probe image well after the pump has passed through the sample. With the assumption that the time-dependent absorption is constant in this temporal region, the image simply reflects the average pump intensity profile as well as the probe intensity profile which is accounted for independently as described above. Although this approach does not correct for shot-to-shot variations in the pump intensity profile, this normalization procedure was found to be reasonably independent of the number of pump shots averaged.

The normalized absorption change as a function of time to be $S(t)$ is linearly mapped onto the spatially dependent function $S(x)$ where x represents the time-encoding direction. Assuming that there is no two-photon or excited state absorption, the absorption signal is linear in the excitation intensity. The spatially dependent intensity profile measure at the CCD $I(x)$ is given by equation 6.1.

$$I(x) = P(x)[\exp(-\alpha l) + E(x) S(x)] \quad (6.1)$$

where α is the linear absorption coefficient, l is the path length and $E(x)$ and $P(x)$ are the spatial intensity profiles of the excitation and probe beams respectively. Determination of $S(x)$ therefore requires the knowledge of $E(x)$ and $P(x)$.

The reference beam corrects for any shot-to-shot spatial profile fluctuations in the probe beam. With the pump beam blocked, the two-dimensional images of the probe and reference beams are collected through the sample over twenty-five laser shots. The images are integrated along their vertical axes to calculate the probe and reference intensity profiles $P(x)\exp(-\alpha l)$ and $R(x)\exp(-\alpha l)$. The spatially dependent ratio of the intensity profiles $C(x)=P(x)/R(x)$ is then calculated and stored. This ratio is observed to be quite stable on a shot-to-shot basis and the averaging is only done to improve the signal-to-noise ratio.

Once $C(x)$ is stored, the pump beam is unblocked and the product of $C(x)$ and $R(x)\exp(-\alpha l)$ is subtracted from the data and the resulting difference is divided by the same product before the data are stored. The reduced data is therefore proportional to $E(x)S(x)$.

$E(x)$ is obtained by averaging the response of a sample with a long lifetime at long delay times where the response is essentially flat. The reduced data is then divided by $E(x)$ and $S(x)$ is obtained. The mapping function between $S(x)$ and $S(t)$ is determined by moving the delay line a known amount and recording the time encoded per unit distance.

The pump and probe light was derived from the amplified dye laser system described in a previous chapter which provided 75 fs pulses centered at 620nm. The repetition rate of the amplifier was set to 120 Hz and a chopper further reduced the repetition rate to 20 Hz because of the limited data acquisition rate of the CCD camera. Approximately 1 μ J of energy was used for the probe light while 4 μ J was used for the pump light. The samples used in this experiment were 100 μ m thick cells containing the laser dyes cresyl violet, ethyl violet, and Nile blue dissolved in methanol.

6.3 Results

Figures 6.4-6.6 show the time-dependent absorption spectra of the laser dyes Nile blue, cresyl violet, and ethyl violet in methanol measured using the single-shot technique. The total absorption change in these samples was approximately ten percent. In Figure 6.4, the time-dependent data in Nile blue obtained from one shot are compared with data obtained from averaging 25 shots. This demonstrates the reproducibility of the signal on a shot-to-shot basis. Figure 6.5 shows two sets of data (each the average of 25 shots) in the dye cresyl violet for which the length of the probe arm differs by

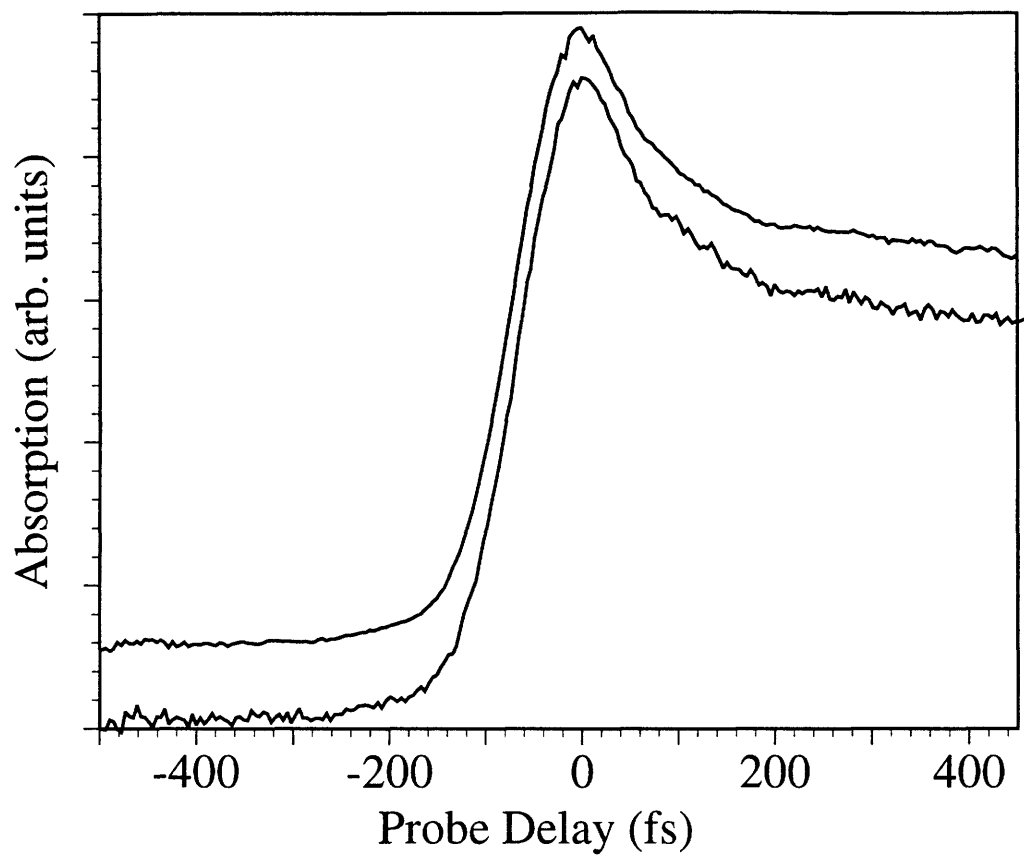


Figure 6.4. Single-shot pump-probe data from the laser dye Nile blue dissolved in methanol. The upper curve is the result of the average of 25 shots while the lower curve is data from a single shot. (The curves are displaced to facilitate comparison.)

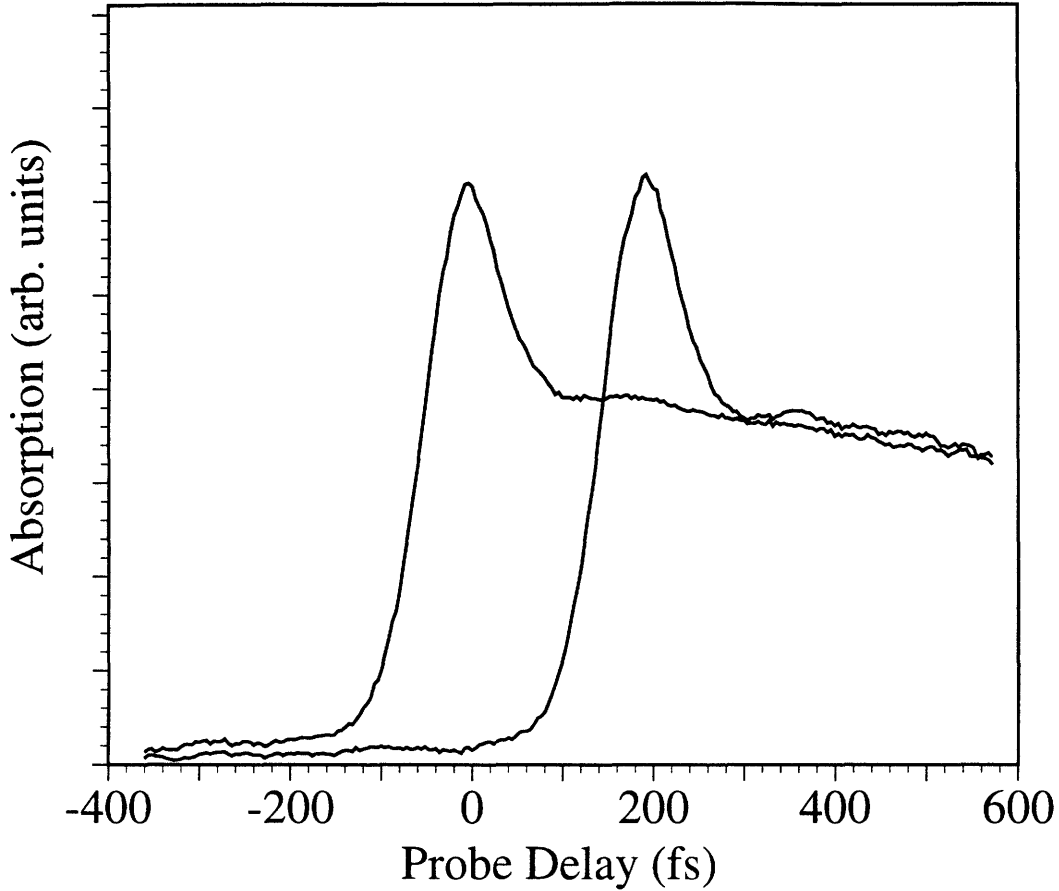


Figure 6.5. Pump-probe data in the laser dye cresyl violet dissolved in methanol. Each curve is the average of 25 laser shots. In the lefthand curve the probe beam has been delayed by 200 fs with respect to the righthand curve.

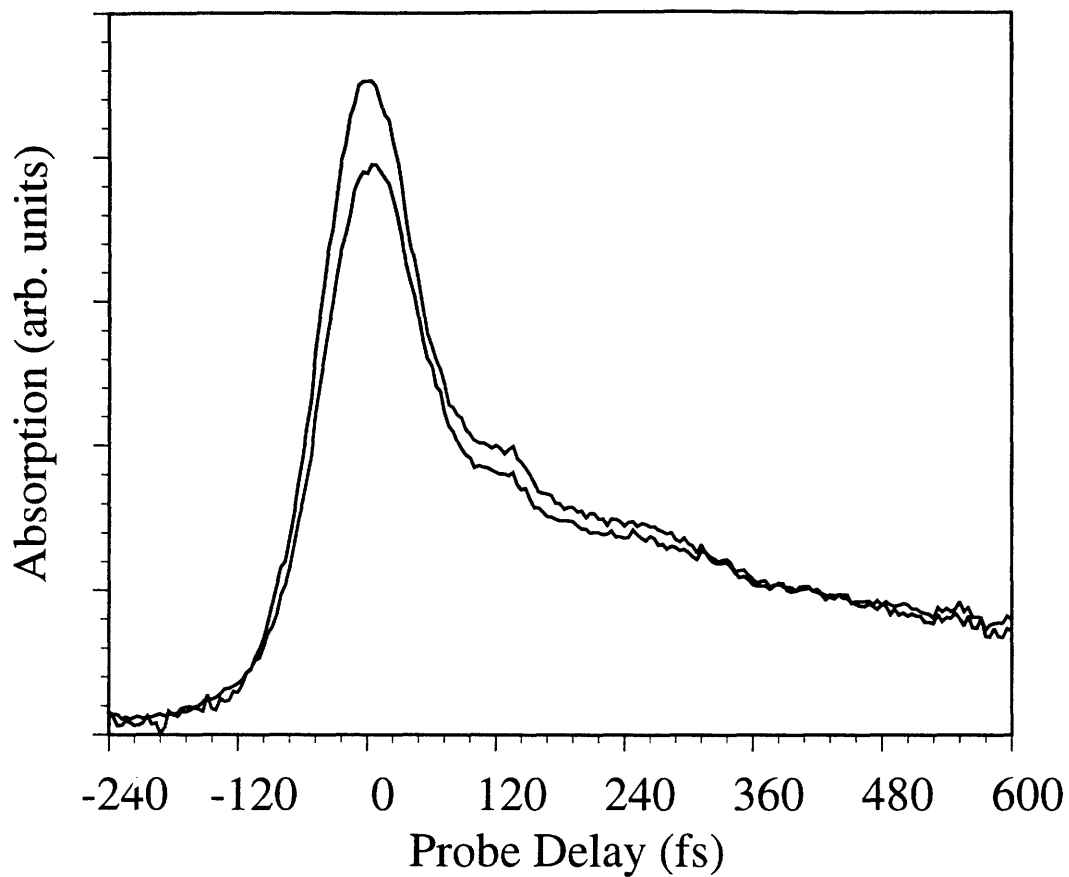


Figure 6.6. Single-shot pump-probe data in ethyl violet in methanol. The lower curve represents the average of 25 shots while the upper curve represents the average of two shots. The frequency of the oscillations is estimated to be 160 fs.

30 μm (or 200 fs). This procedure allows a simple calibration of the time delay.

In Figure 6.6, data from the dye ethyl violet are presented. We wish to emphasize the oscillatory nature of the signal. These oscillations occur with a frequency of approximately 160 fs.

6.4 Discussion

The results demonstrate the high signal-to-noise ratio and the time resolution attainable with the single-shot pump-probe technique presented here. To highlight the near pulse-width limited time resolution achieved, we focus upon the data obtained in the dye ethyl violet shown in Figure 6.6. Figure 6.7 shows the fit to the data generated by convoluting 80 femtosecond pump and probe pulses with the sum of an exponentially decaying cosinusoidal response and purely exponentially decaying term. The amplitudes, decay times, and frequency of the oscillatory term were allowed to vary in order to obtain the best fit. The fit confirms the near pulse-width limited resolution obtainable through this technique.

The time-dependent oscillations observed here have been detected in conventional ultrafast pump-probe studies of ethyl violet in solution⁴ and reflect coherent molecular vibrational motion initiated by the absorption of the ultrashort pulses into an electronic excited state. This demonstrates the ability of this single-shot technique to resolve elementary molecular motions including those involved in a chemical reaction. Many ultrafast studies of irreversible photoinitiated chemical processes in liquids and gases

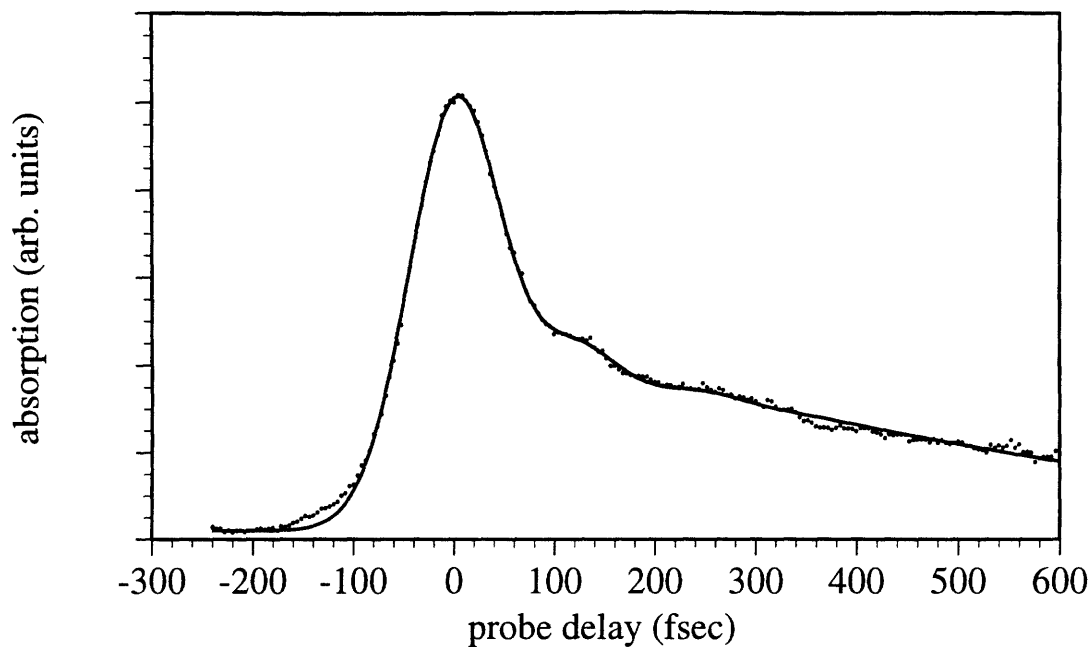


Figure 6.7. Fit to the data obtained in ethyl violet. The data are shown in solid lines while the fit is shown in dashed lines. The fit is generated by convoluting 80 fs pump and probe pulses with the sum of an exponentially damped cosinusoidal response and a purely exponential decaying term. The amplitudes, decay times, and frequency of the oscillatory term were all allowed to vary in order to obtain the best fit.

and reversible processes in solids have revealed the important contributions of the early-time dynamics to chemical reactivity. By using the single-shot laser technique presented here⁵, it is expected that information can be obtained on irreversible chemical processes in solids, polymers, and other media which cannot be easily flowed or translated. Additionally, this technique could provide an experimental probe of structural transformations initiated by high-intensity impulsive excitation. It can be imagined that single-shot experiments on samples with structural phase transitions initiated by phonon motions could follow the phonon dynamics as the structural transformation progresses.

6.5 Limitations of the Single-Shot Technique

The single-shot technique described here holds great potential for spectroscopic characterization of the dynamics of irreversible chemical reactions. However there are a few limitations of the method. First, the total time encoded in this geometry is determined by the spatial size of the linear sample region probed by the cylindrically focused pump and probe beams and the angle between the beams. For practical purposes, this limits the temporal range to several picoseconds. Fortunately, this is not a serious problem in cases in which the interesting dynamics occurs in less than a picosecond. Secondly, the time resolution achieved depends upon the sample thickness. Specifically, the time resolution deteriorates as the sample thickness increases. However, calculations have shown that no serious degradation of resolution occurs up to sample thicknesses

of $100 \mu\text{m}^6$. This dependence upon sample thickness can be avoided by performing the experiment in a reflection geometry rather than a transmission geometry as was done here. Finally the ratio of the temporal range to the time resolution is limited ultimately by the number of pixels in one dimension of the CCD.

6.6 Conclusion

The ability to perform single-shot pump-probe spectroscopy with femtosecond time resolution holds great promise for investigations of the early-time dynamics of irreversible solid-state chemical reactions and laser-induced processes in samples with low damage thresholds. The results presented in the previous sections in which observation of time-dependent molecular vibrations as well as electronic excited state relaxation was reported emphasize the high quality of the data and the sensitivity obtained with this technique. Presently experiments are underway to study the initial dynamics of photoinitiated solid-state reactions in organic crystals and the phonon behavior during lattice melting in several semi-metals.

References

1. (a) M.M. Malley and P.M. Rentzepis, *Chem. Phys. Lett.* **3**, 534 (1969). (b) M.M. Malley and P.M. Rentzepis, *Chem. Phys. Lett.* **7**, 57 (1970). (c) M.R. Topp, P.M. Rentzepis, and R.P. Jones, *Chem. Phys. Lett.* **9**, 1 (1971).

2. (a) A. Brun, P. Georges, G. LeSaux, and F. Salin, *J. Phys. D.* **24**, 1225 (1991). (b) R. Trebino and D.J. Kane, *J. Opt. Soc. Am. A.* **10**, 1101 (1993). (c) D.J. Kane and R. Trebino, *IEEE J. Quantum. Electron.* **29**, 571 (1993). (d) D.J. Kane and R. Trebino, *Opt. Lett.* **18**, 823 (1993).
3. The CCD software was kindly provided by Dr. Thomas P. Dougherty of NIST, Gaithersburg, MD.
4. F.W. Wise, M.J. Rosker, and C.L. Tang, *J. Chem. Phys.* **86**, 2827 (1987).
5. L. Dhar, J.T. Fourkas, and K.A. Nelson, *Optics Lett.* **19**, 643 (1994).
6. J.T. Fourkas, L. Dhar, and K.A. Nelson, submitted to *J. Opt. Soc. Am. B.*

Chapter 7. Future Directions.

The acoustic waveguide studies described in this thesis have focused upon mechanical characterization of thin film systems. The experimental and numerical results presented in Chapter 3 indicate that ISTS can be a powerful tool in characterizing the elastic properties of a film through its depth. The experimental results from the polyimide film bilayer systems demonstrate the depth-profiling capabilities of ISTS and suggest that ISTS may be able to quantitatively characterize films that are expected to exhibit depth-dependent elastic properties such as electron-beam cured films or films in which cross-linking has been induced by ultra-violet light exposure.

In the polariton dynamics study described in Chapter 5, it was seen that ISRS experiments are quite sensitive to the anharmonicities of the lattice potential energy surface. Studying the high temperature behavior of the polariton should yield interesting results as the effect of the anharmonicity increases as a function of temperature. A rigorous test of the sensitivity of ISRS experiments to the form of the anharmonicity should also prove quite useful.

Finally, the technique for performing single-shot ultrafast pump-probe spectroscopy presented in Chapter 6 holds great promise. Further refinement of the technique should allow routine observation of the initial events of irreversible chemical processes.

Appendix A. The Anharmonic Lattice Potential for Lead Titanate.

In this section we briefly describe a simple functional form for the PbTiO_3 anharmonic well and the method used to extract parameters governing this functional form from the lowest few vibrational energy spacings determined from Raman scattering experiments discussed in the main text.

A.1. Anharmonic Well Shapes

Since the number of experimentally measured energy level spacings is limited, a multitude of potential energy shapes exist which can account for the data. For this reason, physical insight must be used to guide the particular choice. We consider the following possible form. Equation A.1, which has recently been proposed for this system, is

$$V(Q) = \alpha Q^2 + \beta Q^4 + \gamma Q^6 \quad (\text{A.1})$$

Here the a , b , and c are unknown parameters governing the shape of the potential. Based on physical intuition, we expect α to be positive and that at least one of β or γ to be negative so that the well is harmonic for small displacements and widens more rapidly than the harmonic well when the displacement increases.

A.2 Extracting the Parameters which appear in (A.1)

One way to determine the energy levels for motion in a potential well with arbitrary shape is to expand the wavefunction describing this motion in terms of a well known basis set. When the expansion of the unknown wavefunction in terms of this basis is inserted into the Schrodinger equation, a system of linear equations is obtained. By writing this system in matrix form, it is easy to show that the positions of the energy levels will occur (i.e. nontrivial solutions for the wavefunctions are obtained) when the determinant of the secular matrix is zero. Therefore, numerical evaluation of these zeroes yields the desired energy levels. By fitting the energy level spacings determined in this way to the measured ones, parameters describing the potential well can be obtained.

It is necessary to describe some details of this procedure as it is applied to the PbTiO_3 system with the well described by (A.1). First, for obvious reasons, we choose the harmonic oscillator basis set for expansion of the actual wavefunction. In order to decrease the convergence time, we choose the frequency of this basis set to be consistent with the energy level spacing of the lowest two modes. Further, for computational reasons, for all expansions, we use only the first twenty of these harmonic oscillator wavefunctions. While this choice limits the accuracy of the determined energies to approximately a few percent of their actual value, non-linear least squares fitting routines which use this energy location method to determine the potential parameters take prohibitively long when more basis functions are used. (We found that less than a one percent change in energy results from using the first fifteen as opposed to the first thirty harmonic oscillator basis set functions.)

We applied the algorithm described above to determine the unknown parameters which appear in equation (A.1). The best fit results for these parameters are given in table A.1, while the best fit calculated and the experimentally measured energy level spacings are given in table A.2. As can be seen from table A.2, only the quartic term in the potential is needed to account for the measured energy level spacings. Addition of the x^6 term does not significantly improve the quality of the fit. Because of this, in the simulations presented in this chapter, only the harmonic and the quartic terms are used in the potential.

Table A.1

Best fit values for PbTiO_3 anharmonicity parameters. In fit #1, the c parameter was fixed to zero, while in fit #2, this parameter was allowed to float. Note the consistency between the best fit parameters in the two cases. (Units are chosen such that \hbar is equal to one and the reduced mass is equal to one half and the energy is in units of 10^{-21} J)

Potential parameter	Best fit value #1	Best fit value #2
α	2.4	2.4
β	-.12	-.11
γ	=0.0	-9.8e-4

Table A.2

Best fit calculated and measured energy level spacings for PbTiO_3 . The energy level spacings were computed using anharmonicity parameters given in table A.1. (Units are chosen such that \hbar is equal to one and the reduced mass is equal to one half and the energy is in units of 10^{-21} J)

Energy level transition	Measured change in energy	Best fit #1 change in energy	Best fit #2 change in energy
1 -> 0	2.954	2.950	2.945
2 -> 1	2.730	2.750	2.753
3 -> 2	2.514	2.490	2.495
4 -> 3	2.196	2.206	2.202

Appendix B. Vibrational Amplitude Amplification Through the Use of Multiple Pulse Excitation.

As discussed in Chapter 5, the energy imparted through ISRS excitation with a single pair of excitation pulses of reasonable energies is negligible compared to the thermal energy available to lattice modes. Therefore, if the coherent vibrational motion induced through ISRS excitation is to be used to drive structural changes or phonon-mediated chemical reactions, a method for achieving large amplitude phonon motion must be developed.

In recent years, pulse-shaping techniques have been used to shape femtosecond pulses into arbitrary waveforms. The use of a timed excitation pulse sequence instead of a single pair of excitation pulses has recently been used to drive phonon modes in the organic crystal α -perylene and the ferroelectric crystal lithium tantalate. By timing a series of excitation pulses to match the vibrational period, repetitive "impulse" driving forces are exerted which gradually build up an increased vibrational amplitude.

In ISRS experiments on lithium tantalate, it was found that photorefractive damage was incurred through two-photon absorption. Therefore, the use of multiple-pulse excitation facilitated low-temperature measurements where single pulse excitation was impossible. By reducing the peak excitation pulse intensity, the two-photon absorption probability was substantially reduced and multiple-pulse ISRS experiments could be carried out without photorefractive damage of the sample. Figure B.1

shows the results of multiple pulse excitation of the lowest frequency A₁ polariton in lithium tantalate at 40K.

Another approach to achieve large amplitude phonon motion is to take advantage of the dispersive nature of polaritons. Because polaritons propagate through the crystal, one could use spatially separated excitation pulses to amplify the vibrational amplitude of a propagating polariton. In Figure B.2 and B.3 are shown the results of simulations of spatially separated multiple pulse excitation of the lowest frequency A₁ polariton in lead titanate. Single excitation pulses rather than pairs of excitation pulses are used. An amplification factor of 4.4 is achieved in Figure B.3 where a set of near spatially continuous excitation beams have been used. In Figure B.2 where the excitation beams are separated by 12 μm, the amplification factor is less than 2.

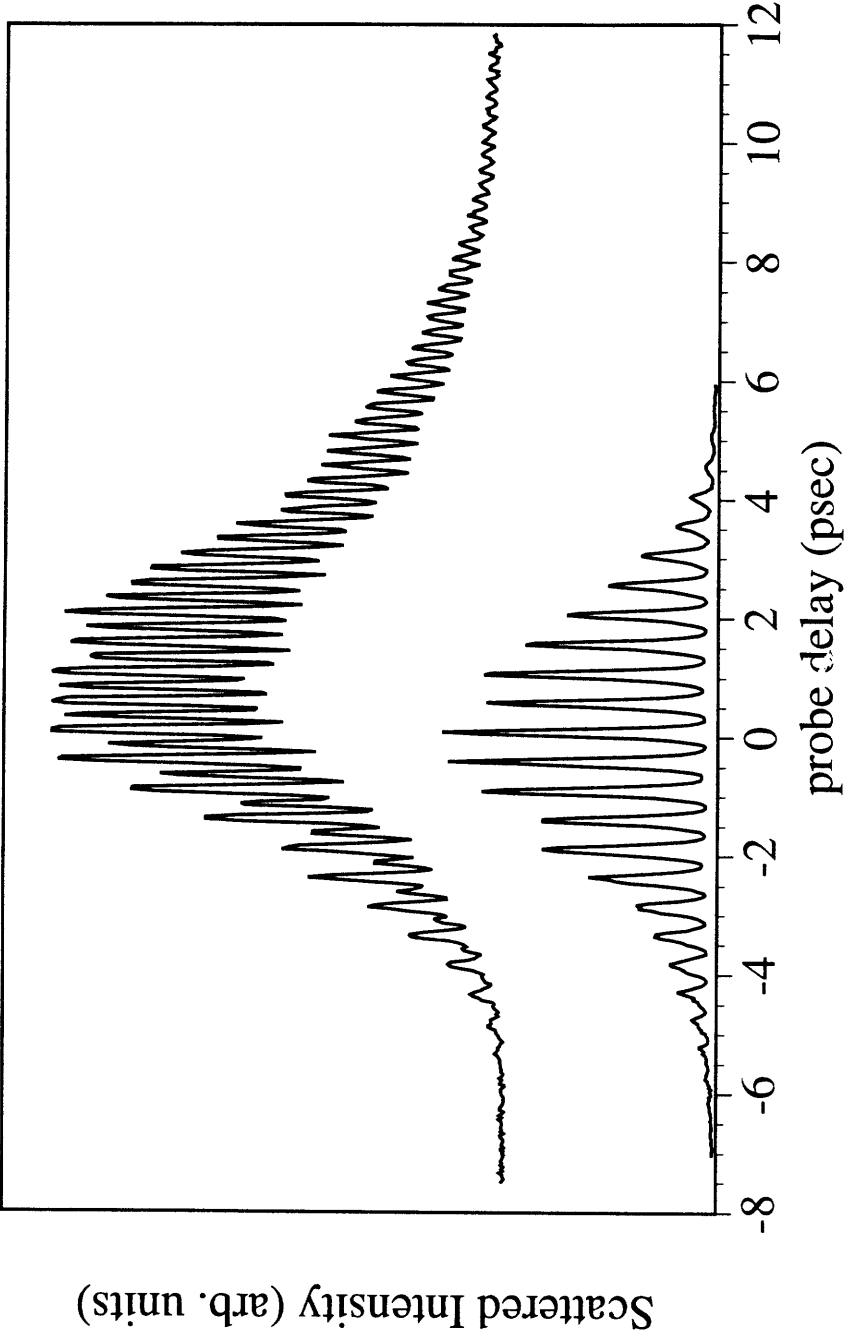


Figure B.1. Multiple excitation pulse ISRS spectroscopy of the lowest frequency A1 polariton in lithium tantalate at 40K (upper trace). The bottom trace is a cross-correlation of the excitation pulse train.

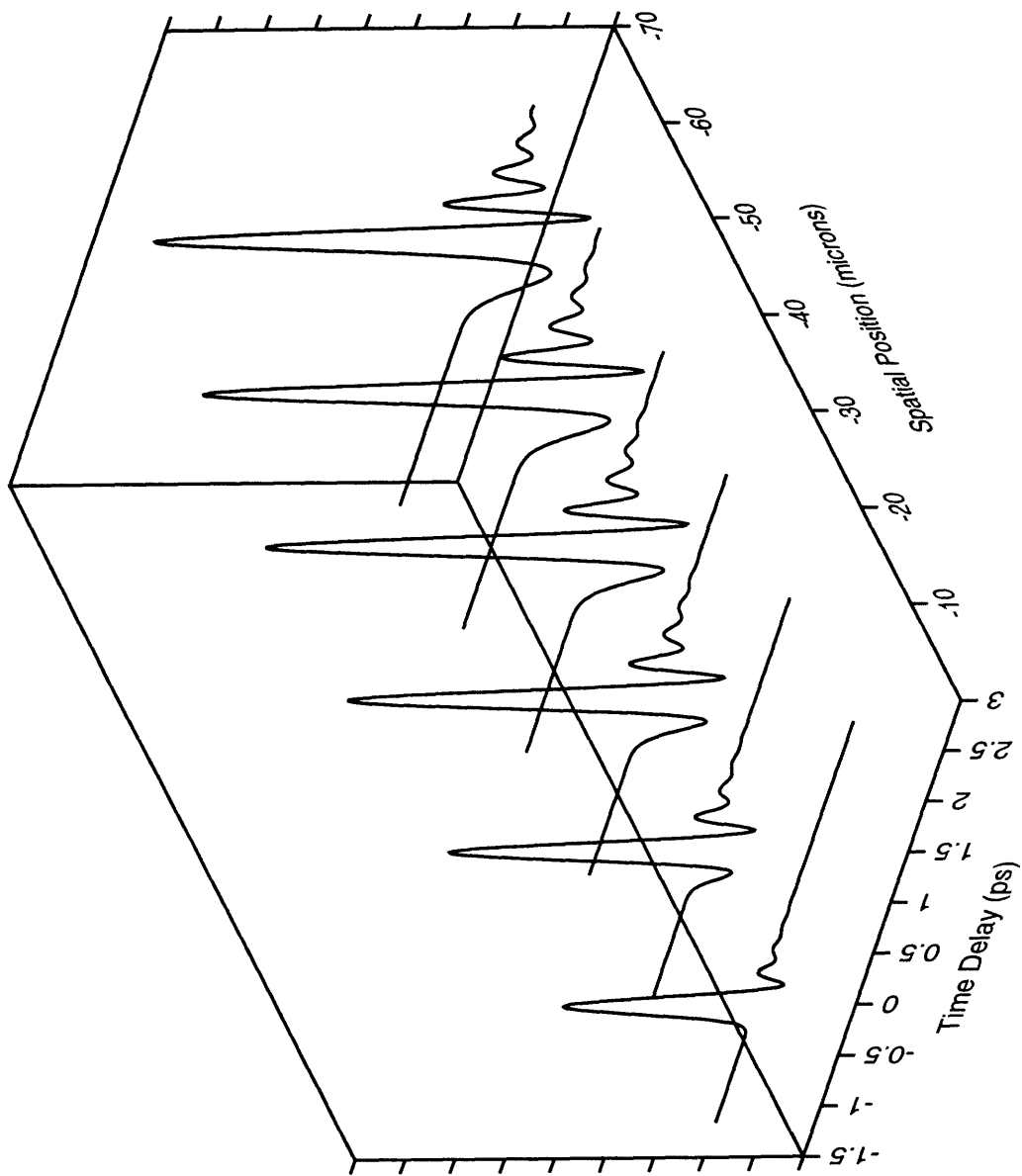


Figure B.2. Vibrational amplitude amplification through the use of spatially separated multiple pulse excitation. Excitation beams with a spot size of $3\ \mu\text{m}$ and with a spatial separation of $12\ \mu\text{m}$ are timed to amplify the propagating polariton in lead titanate coherently excited through single beam ISRS.

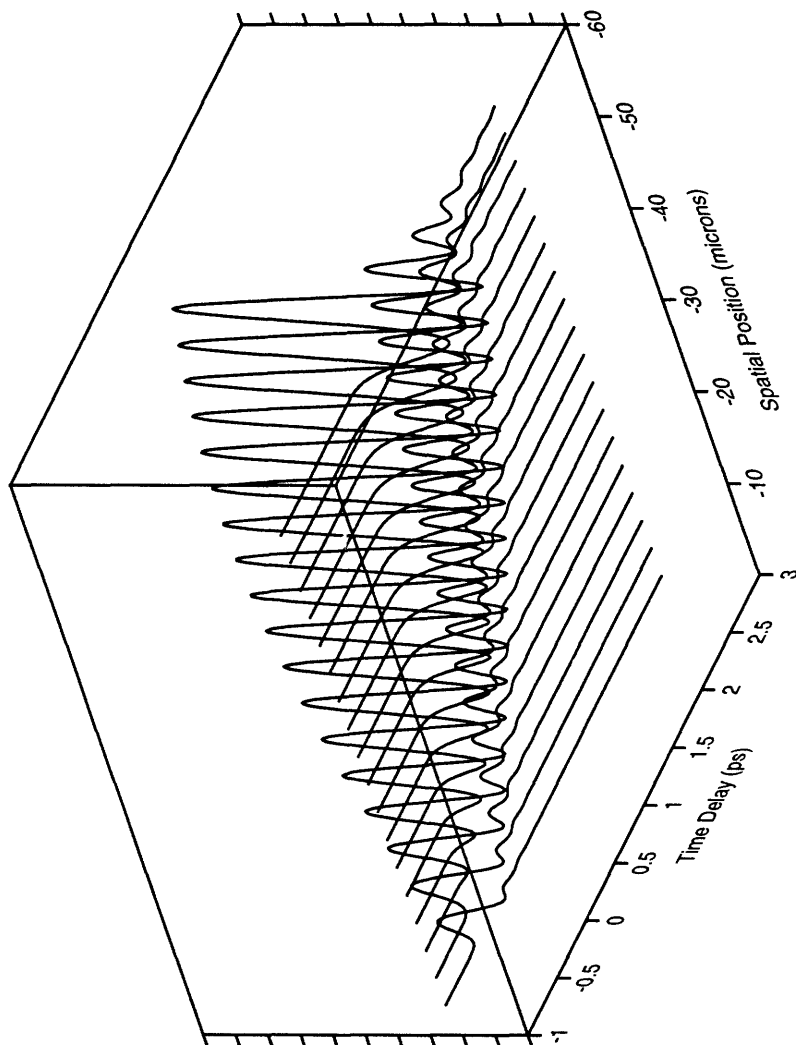


Figure B.3. Vibrational amplitude amplification through the use of spatially separated multiple pulse excitation. The excitation beam spot sizes are $3.5\ \mu\text{m}$ and the beams are separated $3.0\ \mu\text{m}$.